

Università degli Studi di Genova



Scuola politecnica

---

TESI DI LAUREA

**INFLUENCE OF NONLINEAR FLAME  
MODELS ON THERMOACOUSTIC  
INSTABILITIES IN COMBUSTION  
CHAMBERS**

*Candidato:* **Roberto CADEMARTORI**

*Relatore:* Prof. **Alessandro BOTTARO**

*Correlatore:* Ing. **Giovanni CAMPA**

---

*Ottobre 2015*



*Solo coloro che sono così folli da pensare di cambiare il mondo,  
lo cambiano davvero.*

-Albert Einstein



---

## SOMMARIO

---

Nel seguente lavoro di tesi è presentato uno studio di instabilità termoacustica nei combustori di turbogas a ridotte emissioni di NOx. In particolare si vuole studiare l'influenza della non linearità del modello che descrive il comportamento termoacustico della fiamma. Si considera un codice numerico per la costruzione dei cicli limite del sistema. Diversi articoli presenti in letteratura mettono in evidenza i limiti di predizione di un'analisi lineare, e mostrano come la non linearità del modello di fiamma giochi un ruolo fondamentale per la predizione dell'instabilità termoacustica. Nel seguente lavoro tale approccio viene seguito per determinare i cicli limite di diverse configurazioni di combustori, con l'obiettivo di trovare un modello numerico per la predizione dell'instabilità termoacustica in un impianto turbogas. Il codice numerico si basa sulla risoluzione dell'equazione di Helmholtz attraverso un software agli elementi finiti (Comsol Multiphysics). Attraverso un'analisi agli autovalori si valuta la stabilità del sistema. Tale approccio viene studiato in Ansaldo Energia, ed è stato esteso per l'applicazione di modelli di fiamma lineari. In questo lavoro di tesi, svolto in collaborazione con Ansaldo Energia, si prosegue lo studio del modello proposto, valutando la possibilità di eseguire un'analisi di stabilità non lineare in Comsol.



---

## ABSTRACT

---

The thesis presents a thermoacoustic instability study in low NO<sub>x</sub> gas turbine combustors. In particular, influence of nonlinear flame model is studied. Numerical code is considered to create limit cycle of the system. Several papers in literature show prediction limits of linear analysis, and they show the importance of nonlinear flame model in thermoacoustic instability prediction. In this work this approach is used to reproduce limit cycle of several combustors' configurations for the purpose to determinate numerical model for prediction of combustion instability in gas turbine. Numerical code is based on solution of Helmholtz's equation carried by finite element code (Comsol Multiphysics). The stability of the system is evaluated by eigenvalue analysis. This approach is used in Ansaldo Energia for linear flame model. This work is performed with Ansaldo Energia, and it continues the development of proposed model, evaluating the possibility to execute nonlinear analysis in Comsol.



# CONTENTS

<b>1</b>	<b>COMBUSTION IN GAS TURBINE</b>	<b>3</b>
1.1	Gas turbine emissions . . . . .	6
1.2	Development of industrial gas turbine combustion system . . . . .	7
1.3	LPP combustor's instability . . . . .	9
1.4	Suppression methods . . . . .	11
<b>2</b>	<b>THERMOACOUSTIC THEORY</b>	<b>13</b>
2.1	Rayleigh criterion . . . . .	13
2.1.1	Analytical Derivation of the Rayleigh Criterion . . . . .	14
2.1.2	Thermodynamic Interpretation of the Rayleigh Criterion . . . . .	15
2.2	Mathematical model . . . . .	16
2.3	Effect of the mean flow . . . . .	18
<b>3</b>	<b>NUMERICAL MODEL</b>	<b>19</b>
3.1	Flame model . . . . .	19
3.1.1	Linear flame model . . . . .	20
3.2	COMSOL's approach . . . . .	21
3.2.1	Test case 1: cylindrical configuration . . . . .	22
3.2.2	Test case 2: annular configuration . . . . .	24
<b>4</b>	<b>NONLINEAR ANALYSIS</b>	<b>29</b>
4.1	Limit cycle and bifurcation: an overview . . . . .	29
4.1.1	Hopf bifurcation diagrams . . . . .	30
4.1.2	Weakly nonlinear analysis . . . . .	32
4.2	Nonlinear flame model . . . . .	35
4.3	Procedure to track bifurcation diagrams . . . . .	36
<b>5</b>	<b>NUMERICAL TESTS</b>	<b>39</b>
5.1	Rijke tube . . . . .	39
5.1.1	Boundary condition influence . . . . .	40
5.1.2	Time delay influence . . . . .	43
5.1.3	Damping effect . . . . .	45
5.2	Simplified annular combustion chamber . . . . .	49
5.2.1	Polynomial flame model . . . . .	49
5.2.2	Influence of geometry . . . . .	50
5.2.3	Asymmetric conditions . . . . .	53
5.3	Experimental test of Noiray . . . . .	55
5.3.1	Analytical flame model . . . . .	58
5.3.2	Numerical results in Comsol . . . . .	60
5.4	Experimental test of Palies . . . . .	64
5.4.1	Numerical results . . . . .	68

5.4.2	<b>Influence of damping coefficient</b> . . . . .	73
6	<b>ANSALDO MACHINE AEG4.3A</b>	75
6.1	<b>Geometry and boundary conditions</b> . . . . .	75
6.2	<b>Operative conditions</b> . . . . .	77
6.3	<b>Burner transfer matrix</b> . . . . .	78
6.4	<b>Linear analysis</b> . . . . .	80
6.4.1	<b>Results without unsteady heat release</b> . . . . .	80
6.4.2	<b>Results with unsteady heat release</b> . . . . .	80
6.5	<b>Nonlinear flame model</b> . . . . .	85
6.5.1	<b>Test case from the literature</b> . . . . .	85
6.5.2	<b>Experimental flame model</b> . . . . .	87

---

# LIST OF FIGURES

---

Figure 1.1	Gas turbine configuration. . . . .	3
Figure 1.2	Brayton cycle. . . . .	4
Figure 1.3	Simple cycle configuration. . . . .	5
Figure 1.4	Combined cycle configuration. . . . .	5
Figure 1.5	CO and NOx production versus flame temperature [2]. . . . .	7
Figure 1.6	NOx emissions vs equivalence ratio. . . . .	7
Figure 1.7	Comparison of combustor types: conventional diffusion combustor (a), modern premixed combustor (b). . . . .	8
Figure 1.8	LPP combustor's configuration. . . . .	9
Figure 1.9	Burner assembly damaged by combustion instability (left) and new burner assembly (right) (Goy et al. [8]). . . . .	9
Figure 1.10	Experimentally obtained chemical reaction time as a function of the equiv- alence ratio of a hydrocarbon fuel with a molecular weight of about 100 (Zukoski [9]). . . . .	10
Figure 1.11	Schematic drawing of the time evolutions of perturbations responsible for driving combustion instabilities [10]). . . . .	11
Figure 2.1	Thermodynamic interpretation of the Rayleigh criterion [1]. . . . .	15
Figure 3.1	Flame Transfer Function approach. . . . .	20
Figure 3.2	Simplified scheme of flame location in a straight duct with uniform cross section [1]. . . . .	23
Figure 3.3	Variation with $\tau$ of the growth rate for the first mode of the duct in Fig. 3.2 ( $b = 1/10$ ) [1]. . . . .	24
Figure 3.4	Simplified annular combustion chamber; longitudinal view (a), frontal view (b) and internal view (c). . . . .	24
Figure 3.5	Simplified scheme of flame location and boundary conditions, for bench- mark tests on straight duct with variation of section. . . . .	25
Figure 3.6	First four acoustic eigenmodes of the combustor. . . . .	26
Figure 3.7	Variation with $k$ of the normalized frequencies of the annular combustion chamber. $\tau = 0$ s. . . . .	26
Figure 3.8	Influence of time delay on frequency (on the right) and growth rate (on the left) for the first four modes. . . . .	27
Figure 3.9	Influence of time delay on mode (1,1,0). . . . .	28
Figure 4.1	Different types of limit cycle [24]. . . . .	30
Figure 4.2	Steady state oscillation amplitude as a function of R for (a) a supercritical bifurcation and (b-c) a subcritical bifurcation (Campa [1]). . . . .	32
Figure 4.3	Bifurcation diagrams around the Hopf point predicted from the weakly nonlinear analysis [26]. . . . .	35
Figure 5.1	Computational mesh of the Rijke tube (the flame location is highlighted in blue). . . . .	40
Figure 5.2	(a) Flame model in eq.(5.2) with $\mu_2 = 1$ and $\mu_0 = 0.2$ , (b) <i>NFTF</i> in eq.(5.3). . . . .	41

## List of Figures

Figure 5.3	Bifurcation diagram of Rijke tube for the polynomial nonlinear flame model in eq.(5.2) with $\mu_2 = 1$ and $\mu_0 = 0.2$ . . . . .	41
Figure 5.4	Influence of reflection coefficient on limit cycle of eq.(5.2). . . . .	42
Figure 5.5	(a) Flame model in eq.(5.5), (b) <i>NFTF</i> in eq.(5.6) with $\mu_4 = -1$ , $\mu_2 = 1$ and $\mu_0 = 0.2$ . . . . .	43
Figure 5.6	Bifurcation diagram of Rijke tube for the polynomial nonlinear flame model in eq.(5.5) with $\mu_4 = -1$ , $\mu_2 = 1$ and $\mu_0 = 0.2$ . . . . .	44
Figure 5.7	Influence of time delay on bifurcation diagram. . . . .	44
Figure 5.8	Saturation of the normalized heat release rate fluctuations $ Q'/\bar{Q} $ as a function of the amplitude $r$ [39]. (o) Experimental measurements; (---) $ Q'/\bar{Q}  = \mu_0 r$ ; (-) $ Q'/\bar{Q}  = \mu_0 r - \mu_1 r^3$ ; (-·-·-) $ Q'/\bar{Q}  = \gamma \tanh(\delta r)$ . . . . .	45
Figure 5.9	Bifurcation diagram for Rijke tube for nonlinear flame model in eq.(5.8) with $\beta_0 = 1$ and $\beta_1 = 0.5$ . . . . .	46
Figure 5.10	Influence of $\beta_1$ coefficient on stability condition. . . . .	46
Figure 5.11	Influence of sign of $\beta_1$ coefficient on stability condition. . . . .	47
Figure 5.12	Influence of damping coefficient on supercritical (a), and subcritical (b) bifurcation. . . . .	48
Figure 5.13	Computational grid of the simplified annular combustion chamber. . . . .	49
Figure 5.14	Bifurcation diagram of simplified annular combustion chamber for flame model in eq.(5.5) with $\mu_4 = -1$ , $\mu_2 = 1$ and $\mu_0 = 0.5$ . . . . .	50
Figure 5.15	Influence of polynomial coefficients in eq.(5.10):(a) $\beta_0$ coefficient, (b) $\beta_1$ coefficient, (c) $\beta_2$ coefficient. . . . .	51
Figure 5.16	Influence of geometry on bifurcation diagram:(a) variable chamber length, (b) variable plenum length. . . . .	52
Figure 5.17	Asymmetric configurations tested:(a) all burners have the same conditions; (b) one symmetry plane is used to divide six different burners from the others; (c) two symmetry planes are considered; (d) every burner is between two with different conditions; (e) two alternate different burners are applied. . . . .	53
Figure 5.18	Influence of asymmetric conditions of the burners on bifurcation diagram:(a) asymmetric time delay influence, (b) asymmetric flame model influence. . . . .	54
Figure 5.19	Experimental setup of Noiray: the burner is sketched on the left. A close-up view of the flames anchored on the perforated plate is displayed on the right [41]. . . . .	55
Figure 5.20	FDF measured by Noiray: (a) the gain, (b) the phase [41]. . . . .	56
Figure 5.21	Results obtained by Noiray on the first three modes of the system: (a) bifurcation diagram, (b) oscillation frequency expected at the limit cycle [41]. . . . .	56
Figure 5.22	Idealized hysteresis cycle deduced from both experimental results and NDR analysis [41]. . . . .	58
Figure 5.23	Analytical flame transfer function corresponding to eq.(5.11): (a) the gain, (b) the phase [42]. . . . .	59
Figure 5.24	Configuration of numerical model [42]. . . . .	59
Figure 5.25	Analytical flame describing function: (a) the gain, (b) the phase [42]. . . . .	60

Figure 5.26	Bifurcation diagram of the first axial mode of Noiray's test rig with flame model of eq.(5.19), $g_0 = 1.42$ , $\tau_0 = 0.94 \cdot 10^{-3}s$ and $\tau_2 = 0s$ ; (a) $g_1=1$ , (b) $g_1 = 2$ . . . . .	61
Figure 5.27	Bifurcation diagram of the first axial mode of Noiray's test rig with flame model of eq.(5.19), $g_0 = 1.42$ , $g_0 = 0.3$ , $\tau_0 = 0.94 \cdot 10^{-3}s$ and $\tau_2 = 2.5 \cdot 10^{-3}s$ ; (a) Comsol results (b) Green's function results [42]. . . . .	62
Figure 5.28	Bifurcation diagram obtained in Comsol with flame model of eq.(5.19), $g_0 = 1.42$ , $g_0 = 1$ , $\tau_0 = 0.94 \cdot 10^{-3}s$ and $\tau_2 = 2.5 \cdot 10^{-3}s$ . . . . .	63
Figure 5.29	Comparison between experimental bifurcation and numerical results, $g_1 = 1$ . . . . .	64
Figure 5.30	Comparison between experimental bifurcation and numerical results, $g_1 = 1.33$ . . . . .	64
Figure 5.31	Experimental test rig of Palies [45]. . . . .	65
Figure 5.32	Experimental FDF obtained by Palies [45]. . . . .	66
Figure 5.33	Measure of the stability conditions of the combustor. Stable configurations are indicated with gray circles while black stars indicate a high level of rms pressure fluctuation corresponding to a self-sustained oscillation of the system. Gray stars indicate a slightly unstable configuration. [45]. . . . .	67
Figure 5.34	Stability maps obtained by Palies. The colorbar indicates values of $\omega_i - \zeta$ in $s^{-1}$ (negative values correspond to the gray region). The line separating gray and white regions corresponds to points where $\omega_i - \zeta = 0$ meaning that the limit cycle is reached [45]. (a) "Medium" configuration ( $L_1=181.3$ mm), (b) "Long" configuration ( $L_1=245.3$ mm). . . . .	67
Figure 5.35	Comparison between experimental and analytic FDF. . . . .	69
Figure 5.36	Numerical model of test rig: (a) geometry, (b) computational mesh, (c) acoustic mode studied. . . . .	69
Figure 5.37	Comparison between bifurcation diagram obtained by Palies and Comsol results obtained with power function for $\lambda_1$ : (a) "medium" configuration, (b) "long" configuration. . . . .	71
Figure 5.38	Comparison between bifurcation diagram obtained by Palies and Comsol results obtained with polynomial function for $\lambda_1$ : (a) "medium" configuration, (b) "long" configuration. . . . .	72
Figure 5.39	Comparison between bifurcation diagram obtained by Palies and Comsol results obtained with flame model in (5.24): (a) "medium" configuration with $\lambda_{1M}$ in (5.31) and $\lambda_{2M}$ in (5.26) , (b) "long" configuration with $\lambda_{1L}$ in (5.32) and $\lambda_{2L}$ in (5.28). . . . .	73
Figure 5.40	Stability maps of test rig obtained in Comsol. The color zones indicates values of $\omega_i - \zeta$ in $s^{-1}$ . (a) "medium" configuration, (b) "long" configuration. . . . .	74
Figure 5.41	Influence of damping on calibration coefficient $\lambda_1$ . . . . .	74
Figure 6.1	Quarter of the whole combustion chamber in the 3D FEM code: (a) top view, (b) bottom view [1]. . . . .	76
Figure 6.2	Computational grid of one quarter of the system: (a) top view, (b) bottom view [1]. . . . .	76
Figure 6.3	Temperature field in combustion chamber (Fluent data): (a) view of plan parallel to the yz plan, (b) view of plan parallel to the zx plan [1]. . . . .	77
Figure 6.4	Model of the burner transfer matrix with the inlet and outlet surfaces [1]. . . . .	79

## List of Figures

Figure 6.5	Frequencies and growth rates of the modes regarding the actual annular combustion chamber without unsteady heat release. . . . .	80
Figure 6.6	<i>Reaction Rate</i> from RANS simulation. : (a) view of chamber, (b) view along one sector axis. The values are normalized against the maximum Reaction Rate. [1]. . . . .	82
Figure 6.7	Time delay from RANS simulation in the 3D FEM code. The values are normalized against the maximum value [50]. . . . .	83
Figure 6.8	Comparison between eigenvalues of machine obtained with linear flame model and the ones evaluated without unsteady heat release. . . . .	83
Figure 6.9	First azimuthal mode in combustion chamber. . . . .	84
Figure 6.10	Influence of time delay on the first azimuthal mode in combustion chamber: (a) frequency dependence, (b) growth rate dependence. . . . .	85
Figure 6.11	Influence of interaction index on the first azimuthal mode in combustion chamber: (a) frequency dependence, (b) growth rate dependence. . . . .	85
Figure 6.12	Bifurcation diagram for machine configuration with flame model of eq.(5.2), $\mu_2 = 1$ and $\mu_0 = 0.2$ . . . . .	86
Figure 6.13	Influence of time delay of flame model in eq.(5.2) on stability of machine combustor. . . . .	86
Figure 6.14	Influence of damping coefficient on stability of machine combustor. . . . .	87
Figure 6.15	FDF obtained by Palies scaled on frequency of Ansaldo machine mode. . . . .	88
Figure 6.16	Bifurcation diagram of real machine evaluated with experimental flame model of eq.(5.21): (a) calibration coefficients of eqs.(5.31) and (5.26), (b) calibration coefficients of eqs.(5.32) and (5.28). . . . .	89
Figure 6.17	FDF with second peak at normalized frequency equal to 3.27 : (a) gain=0.8, (b) gain=1, (c) gain=1.2, (d) gain=1.4. . . . .	90
Figure 6.18	Influence of the second peak gain of FDF on bifurcation diagram. . . . .	90
Figure 6.19	FDF with second peak gain of 1.2 : (a) second peak at 2.9, (b) second peak at 3, (c) second peak at 3.27. . . . .	91
Figure 6.20	Influence of the second peak position on bifurcation diagram. . . . .	91

---

## LIST OF TABLES

---

Table 3.1	Geometry details of simplified annular combustion chamber . . . . .	25
Table 3.2	Operating conditions . . . . .	25
Table 5.1	Rijke tube dimensions . . . . .	39
Table 5.2	Rijke tube operating conditions . . . . .	40
Table 5.3	Noiray test rig conditions . . . . .	59
Table 5.4	Comparison of experimental and numerical predicted frequency of the mode in Fig.5.36c for the medium (M) and long (L) upstream manifold with the two flame tube size $L_3 = 200,400$ mm at $r = 0.1$ . . . . .	72
Table 6.1	List of the first modes until 250 Hz. Frequencies are normalized against the first eigenfrequency. . . . .	81

---

# NOMENCLATURE

---

## Latin

A	area
b	position
c	speed of sound
$c_p$	specific heat at constant pressure
$c_v$	specific heat at constant volume
e	acoustic energy density
$\mathbf{e}$	unit vector
$E_a$	acoustic energy flux
f	acoustic frequency
g	gain parameter
h	enthalpy
$h_f$	lower heating value
i	imaginary unit
J	Jacobian matrix
$K_i$	wave number
K	conductivity
k	interaction index
$l_a$	order of pure axial mode
L	length
m	mass flow rate
$m_a$	order of pure azimuthal mode
M	Much number
n	parameter
$n_a$	order of pure radial mode
p	pressure
q	heat release
$q_1$	q first derivative in zero
$q_2$	q second derivative in zero
$q_3$	q third derivative in zero
Q	heat release per unit area
$Q^{CM}$	COMSOL monopole source
r	nonlinear flame model amplitude
R	control parameter

RR	rate of reaction
$R_g$	gas constant
$R_L$	reflection coefficient
$R_d$	duct radius
$\Re$	real part
S	entropy
t	time
T	temperature
$T_L$	transmission coefficient
$\mathbf{u}$	velocity vector
v	specific volume
V	volume
x	state vector variable
$x_0$	equilibrium point
Z	sound impedance

## Greek

$\alpha$	area ratio
$\beta$	parameter
$\gamma$	ratio of specific heats
$\delta$	Dirac's delta
$\varepsilon$	small parameter
$\zeta$	damping coefficient
$\eta$	fundamental mode of the velocity fluctuation
$\eta_{th}$	thermodynamic efficiency
$\lambda$	eigenvalue = $-i\omega$
$\lambda_1$	calibration coefficient
$\lambda_2$	calibration coefficient
$\mu$	polynomial function's coefficient
$\xi$	parameter
$\rho$	density
$\sigma_{i,j}$	viscous stress tensor
$\tau$	time delay
$\varphi$	phase
$\phi$	equivalent ratio
$\Phi$	wave energy dissipation
$\chi$	fast time
$\omega$	pulsation

## Superscript

–	mean quantity
/	fluctuating quantity
^	complex quantity
(1)	first Fourier coefficient

## Subscript

C	chamber
d	downstream
eff	effective
F	fold point
H	Hopf point
i	direction
L	linear
NL	nonlinear
oe	open-end
p	plenum
pp	perforated plate
u	upstream

## Abbreviations

AX	axial
AZ	azimuthal
DZ	dilution zone
FEM	finite element method
FTF	Flame Transfer function
FDf	Flame describing function
HAP	hazardous air pollutants
LDI	lean direct injection
LHS	left hand side
LPM	lean-premixed combustion
LPP	lean-premixed prevaporized combustion
ODE	ordinary differential equation
PZ	primary zone
RHS	right hand side
RQL	rich-burn quick-quench lean-burn
SZ	secondary zone
VOC	volatile organic compounds
PM	particulate matter
UHC	unburned hydrocarbons

---

# INTRODUCTION

---

The trend of low polluting, high performance power generators led modern gas turbine's combustor to be annular and supplied with a lean premix of gas and compressed air. In particular, lean premix combustion allows reducing combustion temperature, and then NO<sub>x</sub> emissions are restricted. This configuration, despite its advantages, promotes a thermoacoustic combustion instability also called humming. It is an interaction between heat release and pressure oscillations in combustion chambers, which sometimes leads to damages and machine failures. This phenomenon is known since a very long time. In 1859 Pieter Rijke discovered a way of using heat to sustain a sound in a cylindrical tube open at both ends. In 1878 Lord Rayleigh defined a criterion based on a phenomenological and heuristic description of the instability [1]. Although known since a long time, this phenomenon is not fully understood yet and it is surely not desirable. This instability shows up under certain circumstances, when perturbations in the flow affect the flame dynamics, hence the rate of heat released by the flame. This change in the rate of heat release affects the acoustic waves, creating a feedback loop between the acoustic waves and the heat-release rate fluctuations. This feedback between acoustic and combustion may lead to instability with highly undesirable and often dangerous consequence. Today thermoacoustic instability is much important in many practical operations. In fact in various combustion systems occasionally the oscillations do not pose difficulties, but in many cases the amplitude of the pressure fluctuations are sufficiently high to be unacceptable. There seems to be four general circumstances under which combustion instabilities occur in practical system:

1. sufficiently high densities of combustion energy release;
2. introduction of pulses;
3. unstable mean flow field or geometric configuration favourable to shedding large vortices;
4. operation near the lean blowout limit.

The latest condition has been commonly observed in contemporary gas-turbine combustors designed to operate near blowout limit as part of the strategy to reduce production of oxides of nitrogen, and it is an important case study for Ansaldo Energia. The study of thermoacoustic combustion instability is a very complex issue and, over the years, several different numerical approaches have been developed to model as well as possible this phenomenon. These approaches can be grouped in three different categories:

1. low order model;
2. CFD (computational fluid dynamics) models;

### 3. Helmholtz solvers.

These numerical methods require a suitable description of the feedback of the flame to the incoming perturbations, the geometry of the burner and the boundary conditions. In particular, the relation from flow oscillations and heat release oscillations is not known and an empirical solution may be inserted. A Flame Transfer Function (FTF) links the heat release oscillations and the flow oscillations. Usually a linear FTF is used, and time delay between flow oscillations and heat release is considered. Although linear techniques are able to predict whether the non-oscillating steady state of a thermoacoustic system is asymptotically stable (without oscillations) or unstable (increasing oscillations), a thermoacoustic system can reach a permanent oscillating state (the so called "limit cycle"), even when it is linearly stable, if a sufficiently large impulse occurs. A nonlinear analysis is able to predict the existence of this oscillating state and the nature of the bifurcation process.

The aim of this work is to investigate the behaviour of gas turbine combustion chambers in presence of nonlinear flame models. The bifurcation diagram helps in the understanding of the influence of limit cycles as a function of the parameters of the system. It shows the amplitude alteration of the system from stability to instability conditions and it shows which value of the control parameter makes the system unstable. The bifurcation diagrams, obtained by using a continuation technique in the frequency domain, give the amplitude of the oscillations as a function of a chosen flame parameter. The Helmholtz equation is used to model the combustion chamber and nonlinear terms are introduced in the flame model, starting from the classical  $n$ - $\tau$  formulation. A three-dimensional finite element method (FEM) is used for the discretization of the computational domain and a solver of quadratic eigenvalue problems is combined with Newton technique in order to identify the points of the bifurcation diagram.

In the [first chapter](#) of thesis an overview of gas turbine's combustion is presented. In particular, it is reported a brief description of gas turbine emissions and the main practical configurations of combustion systems as of now adopted. Also, a description of the lean premixed combustion system can be found, with an overview about the phenomenon of the thermoacoustic combustion instability. In the [second chapter](#) thermoacoustic theory is approached and mathematical model is illustrated. The numerical FEM approach used in this work is reported in the [third chapter](#). The nonlinear analysis is the subject of the [fourth chapter](#). In particular, the bifurcation concept is illustrated and how a non-linear phenomenon is present in combustion thermoacoustic analysis. Then, the analytical form of nonlinear flame models is described and the procedure to track bifurcation diagrams in FEM code is illustrated. In the second part of thesis several numerical test are reported. The [fifth chapter](#) shows the results obtained in Rijke tube and in simplified annular combustor geometry. As can be found in the literature, several nonlinear flame models are applied in order to obtain bifurcation diagrams. Then, the nonlinear analysis is applied to two experimental setup, and numeric results are compared with experimental data. Finally, in [sixth chapter](#), practical machine geometry is tested and the accuracy of the model is evaluated.

# 1

## COMBUSTION IN GAS TURBINE

A gas turbine engine is a device that is designed to convert the thermal energy of a fuel into some form of useful power, such as mechanical (or shaft) power or a high speed thrust of a jet. It is formed by a gas compressor, a burner (or combustion chamber) and an expansion turbine (Fig.1.1). The main advantage of

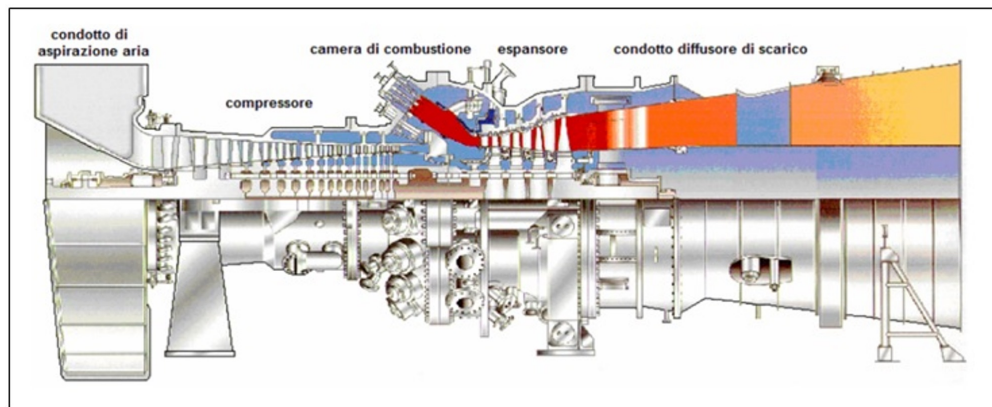


Figure 1.1: Gas turbine configuration.

this technology is the high power to weight ratio that leads to use gas turbine as aeronautic propeller and for electric power generation. The engine is based on Brayton cycle (Fig.1.2) which considers four thermodynamic processes:

- isentropic process (1-2), ambient air is drawn into the compressor, where it is pressurized;
- isobaric process (2-3), the compressed air runs through a combustion chamber where combustion transforms chemical energy of gas in heat power;
- isentropic process (3-4), the heated pressurized air gives up its energy expanding through a turbine;
- isobaric process (4-1), heat rejection in the atmosphere.

However, in a practical gas turbine, mechanical energy is irreversibly transformed into heat when gases are compressed, due to internal friction and turbulence. Also, passage through the combustion chamber is accompanied by slight loss in pressure and during expansion, between the stator and rotor blades of turbine, irreversible energy transformation once again occur. Then, ideal Brayton cycle is a theoretical model but in practical machine entropy variation and efficiency of the components must be considered ( $1'-2'-3'-4'$ ). As the temperature increases isobaric line diverges, and this causes an enthalpy variation higher than in the turbine to the compressor.

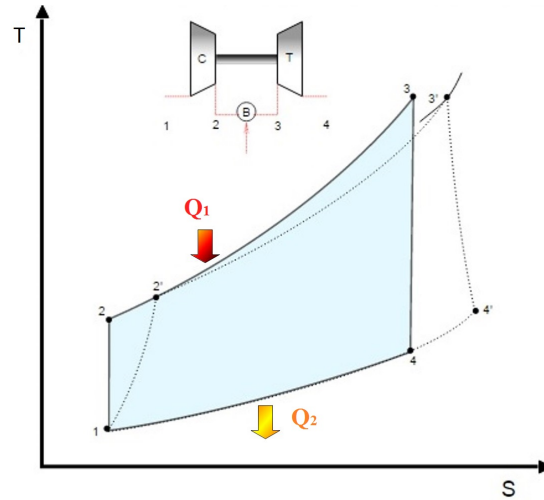


Figure 1.2: Brayton cycle.

This implies that some of the work extracted by the turbine is used to drive the compressor but the residual mechanical power can be exploited. An important parameter of power system is the thermal efficiency. It is defined as:

$$\eta_{th} = 1 - \frac{|Q_2|}{|Q_1|} \quad (1.1)$$

Considering air as perfect gas, specific heat ratio constant in chemical composition and temperature,  $\frac{T_2}{T_1} = \frac{p_2}{p_1}^{\left(\frac{k-1}{k}\right)}$  and then  $T_1 T_3 = T_2 T_4$ , thermal efficiency of ideal Brayton cycle becomes:

$$\eta_{th} = 1 - \frac{T_4}{T_3} \quad (1.2)$$

Eq.1.2 shows that thermal efficiency grows as  $T_3$  increases. A higher efficiency leads to lower fuel consumption and then lower production costs. Also pollutant emission is reduced. For this, turbine inlet temperature is the highest possible, according to structural mechanical limit. As of now, turbine materials and cooling technique allows to turbine inlet temperature about 1100-1400 °C. In electric power generation, simple cycle configuration use the surplus of mechanical power to moves an alternator keyed on the same shaft of the turbine (Fig.1.3). For this configuration, assuming maximum admissible temperature, thermal efficiency is about to 0.35-0.4. To increase performance combined cycle configuration can be used. Waste heat from the turbine is recovered by a heat recovery steam generator to power a conventional steam turbine (Fig.1.4). Combined cycle has efficiency about 0.6 and it is the configuration usually used for power generation. Since simple cycle power plants are less efficient than combined cycle plants, they can be turned on and off within minutes. This makes the simple cycle very flexible and they can be used to supply power during peak or unscheduled demand. The combustion is very important process to reach the required performance. It must ensure the turbine inlet temperature for requested efficiency, and at the same time low pressure losses, combustion stability and low pollutant emissions. The combustion process in gas turbine can be classified as diffusion flame combustion, or lean-

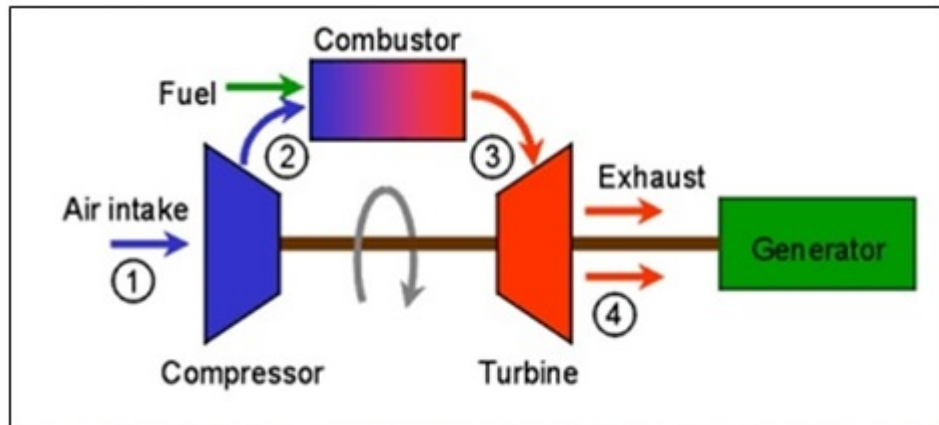


Figure 1.3: Simple cycle configuration.

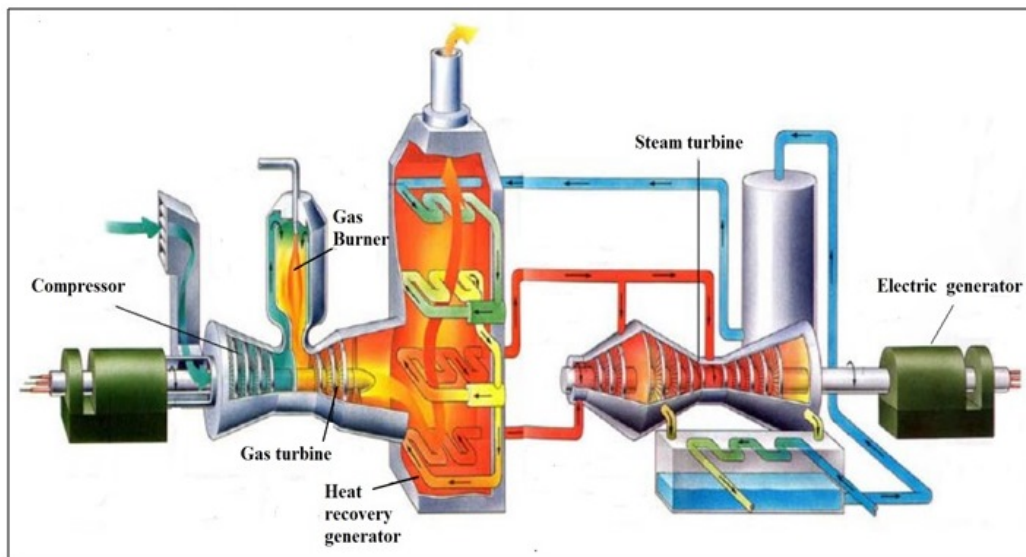


Figure 1.4: Combined cycle configuration.

premix staged combustion. In the diffusion flame combustion, the fuel-air mixing and combustion take place simultaneously in the primary combustion zone. This generates regions of near stoichiometric fuel-air mixtures where the temperatures are very high. For lean-premix combustors, fuel and air are thoroughly mixed in an initial stage resulting in a uniform, lean, unburned fuel-air mixture which is delivered to a secondary stage where the combustion reaction takes place. Diffusion combustion is more stable than lean-premix combustion but it causes high flame temperature. Discharge limits for  $\text{NO}_x$  and  $\text{CO}$  are becoming increasingly stringent. One of the most logical control solutions is to reduce emissions at the source. This can be a double-edged sword, as higher combustion temperatures improve turbine efficiency and reduce  $\text{CO}$ , but increase  $\text{NO}_x$ . The opposite effect occurs at lower combustion temperatures. Today, the strict regulation for pollutant emissions imposes low flame temperature, then lean-premix combustion is used to reduce  $\text{NO}_x$  emissions and instability's studies are much important for proper operation of combustion chamber.

## 1.1 GAS TURBINE EMISSIONS

The primary pollutants from gas turbine engines are nitrogen oxides (NO<sub>x</sub>), carbon monoxide (CO), and to a lesser extent, volatile organic compounds (VOC). Particulate matter (PM) is also a primary pollutant for gas turbines using liquid fuels. Nitrogen oxide formation is strongly dependent on the high temperatures developed in the combustor. Carbon monoxide, VOC, hazardous air pollutants (HAP), and PM are primarily the result of incomplete combustion. Trace to low amounts of HAP and sulfur dioxide (SO<sub>2</sub>) are emitted from gas turbines. Ash and metallic additives in the fuel may also contribute to PM in the exhaust. Emissions of oxides of sulphur (SO<sub>x</sub>) will only appear in a significant quantity of sulphur in the fuel but it can be considered less important. Other types of pollutants are greenhouse gases. Carbon dioxide (CO<sub>2</sub>) and nitrous oxide (N<sub>2</sub>O) emissions are all produced during natural gas and distillate oil combustion in gas turbines. Nearly all of the fuel carbon is converted to CO<sub>2</sub> during the combustion process. This conversion is relatively independent of firing configuration. Methane (CH<sub>4</sub>) is also present in the exhaust gas and is thought to be unburned fuel in the case of natural gas or a product of combustion in the case of distillate fuel oil. Although the formation of CO acts to reduce CO<sub>2</sub> emissions, the amount of CO produced is insignificant compared to the amount of CO<sub>2</sub> produced. The majority of the fuel carbon not converted to CO<sub>2</sub> is due to incomplete combustion. Gas turbines without any pollutant's abatement technology usually have emissions in the range between 180 and 400 ppm, depending on type and load. On the other hand, CO emissions are very low, often below 10 ppm, then the goal of new combustion chamber project is to reduce NO<sub>x</sub> emissions. Relative NO<sub>x</sub> emissions for diffusion combustors increase with an increasing load, due to a rise in combustion temperature. In fact the most important factor affecting formation of NO<sub>x</sub> is flame temperature; this is theoretically a maximum at stoichiometric conditions and will fall off at both rich and lean mixtures. Unfortunately, while operating well away from stoichiometric could reduce NO<sub>x</sub> this results in increased formation of both CO and UHC. NO<sub>x</sub> formation rate varies exponentially with flame temperature, so the key to limit NO<sub>x</sub> emissions is reduction of flame temperature. This may be solved by introduce diluents into the combustion zone. CO is initially formed in large quantities in a flame and converts to CO<sub>2</sub>. As blowout is approached, CO emissions climb rapidly because the flame temperature is not high enough to convert it to CO<sub>2</sub>. At low loads, CO concentration is high due to airflow through adjacent unlit domes, which is caused by unburned air quenching the combustor. Low NO<sub>x</sub> and CO emissions occur in a narrow band of flame temperature, which is seen from Fig. 1.5. Optimum adiabatic flame temperature range is usually between 1400 and 1600°C [2].

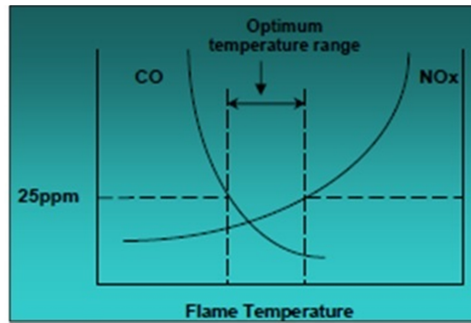


Figure 1.5: CO and NOx production versus flame temperature [2].

## 1.2 DEVELOPMENT OF INDUSTRIAL GAS TURBINE COMBUSTION SYSTEM

The increasingly strict regulation for pollutant emissions has recently led engine manufacturers to develop combustors that meet various regulatory requirements (Bahr [3]; Correa [4]). New concepts for combustion technology have been introduced to the gas turbine industry, including lean-premixed (LPM) combustion (or lean-premixed prevaporized (LPP) combustion when liquid fuels are employed), rich-burn quick-quench lean-burn (RQL) combustion, and catalytic combustion (Lefebvre [5]; Correa [6]). Among these methods, RQL techniques are hampered by soot formation and incomplete mixing between fuel-rich combustion products and air. Catalytic combustion suffers from challenges associated with cost, durability and safety. Lean-premixed (prevaporized) combustion appears to be the most promising technology for practical systems at the present time (note that for aero-engine gas turbines using liquid fuels, lean direct injection (LDI) combustion is often adopted for pollution control because of its superior stability behaviour). In LPP combustion, the fuel and air are premixed upstream of the combustor to avoid the formation of stoichiometric regions. The combustion zone is operated with excess air and then, as Fig.1.6 shows, the flame temperature is reduced. Consequently, thermal NOx is virtually eliminated (Zeldovich [7]).

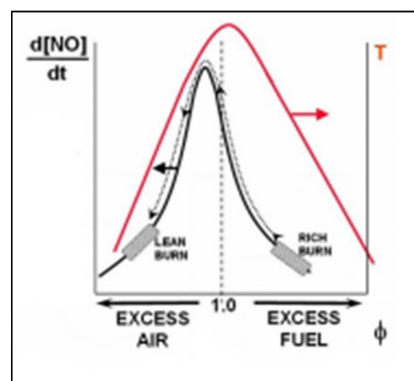
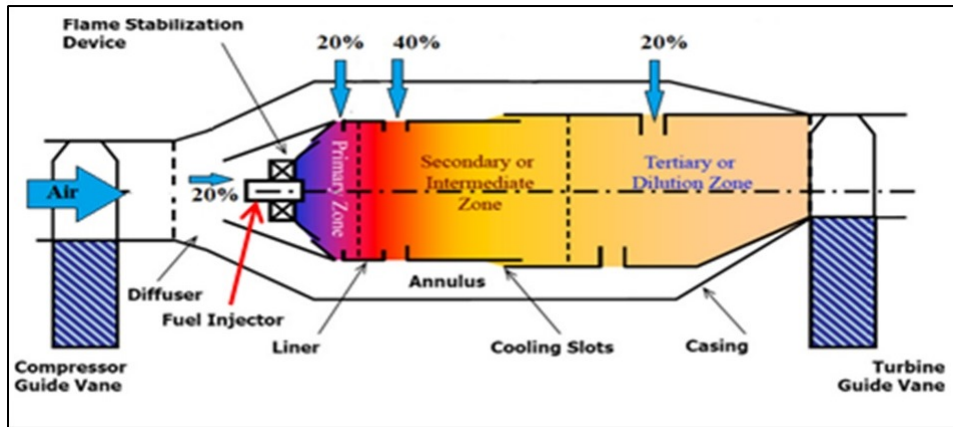
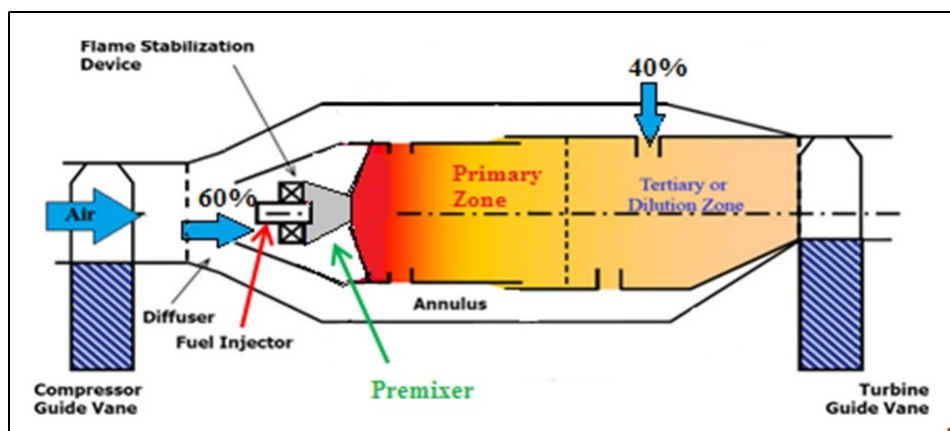


Figure 1.6: NOx emissions vs equivalence ratio.



(a)



(b)

Figure 1.7: Comparison of combustor types: conventional diffusion combustor (a), modern premixed combustor (b).

Differences between conventional diffusion and modern premixed combustors are illustrated in Fig.1.7. In both type, airflow is slowed down by diffuser for decreasing pressure loss and it is split up by the liner. One part of the airflow goes through the annulus, the region between the liner and the casing, for cooling and dilution purposes, another part of the airflow enters the mixing chamber, where fuel is injected. The liner is divided into three sections, primary zone (PZ), secondary zone (SZ) and dilution zone (DZ). The main function of PZ is to provide enough time for the fuel to mix and to create combustion conditions. The goal of the SZ is to provide enough time to achieve full combustion. This significantly reduces bad reaction products like carbon monoxide and unburned hydrocarbons. Finally the goal of the DZ is to reduce the temperature of the outlet stream, such that it is acceptable for the turbine. The premixed design mixes the fuel and air prior to injection into the PZ, whereas mixing of the fuel and air for diffusion flames does not occur until inside the PZ. A smaller fraction of the air is diverted to the annulus in premixed designs as leaner fuel/air mixtures are required. This reduces the amount of air available for cooling purposes and necessitates the use of advanced techniques. Conventional film cooling slot designs limit the amount of air available

for leaner combustion. They must also be avoided as the admission of cooler air into the PZ can potentially reduce flame stability and increase CO emissions. In conventional combustors additional air is admitted through holes in the liner into the secondary zone (SZ) to allow the complete oxidation of CO into CO<sub>2</sub>. Premixed combustors do not require a SZ as their lower peak flame temperature minimizes the dissociation of CO<sub>2</sub> into CO. The hot combustion products are then diluted with the remaining annulus air in the dilution zone (DZ). Less time for mixing in the DZ is required for premixed combustors as the peak flame temperatures are significantly lower than those in conventional ones.

### 1.3 LPP COMBUSTOR'S INSTABILITY

LPP burners are generally adopted in modern gas turbines for their superior performance of pollutants reduction, but they have serious drawback such as flame blow-out, autoignition, and flashback, which do not appear in conventional diffusion flame type. Premixing duct is an important parameter of LPP and its design is most important (Fig.1.8).

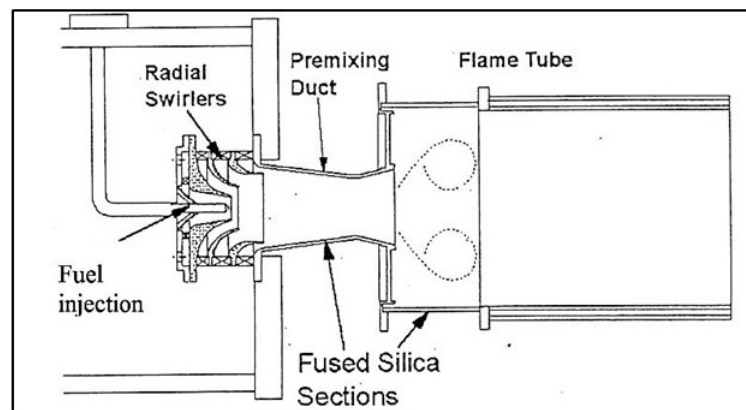
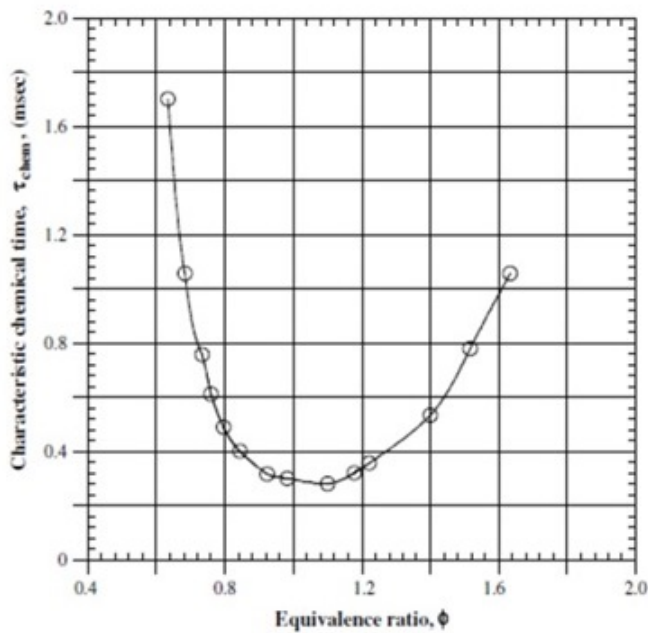


Figure 1.8: LPP combustor's configuration.

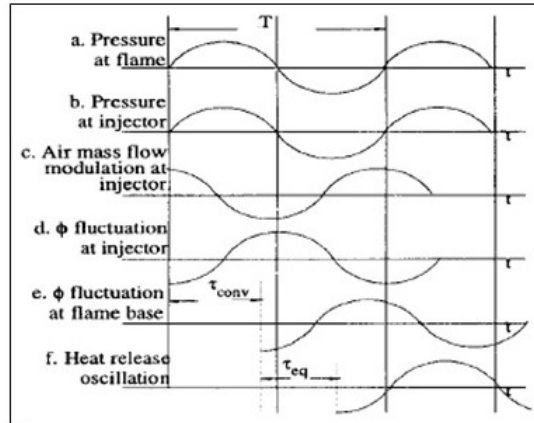


Figure 1.9: Burner assembly damaged by combustion instability (left) and new burner assembly (right) (Goy et al. [8]).

At inlet, radial swirlers and converged duct reduce turbulence and accelerate flow to avoid flashback and auto-ignition, second part of the duct diverges to slow down flow to improve flame stability. Over these issues, one of serious problem is that premixed combustion at lean conditions has been sensitive to combustion instability. When premixed combustion becomes unstable, unsteady fluctuation in pressure and heat fluxes are observed to increase significantly. As a result, the fatigue of materials from mechanical vibration induced by the high amplitude of pressure fluctuation and large unsteady heat fluxes would considerably shorten the lifetime of combustor. Fig.1.9 shows a burner assembly damaged by combustion oscillations, and, for comparison, a new burner assembly. One explanation for that lean premixed combustion is susceptible to instabilities can be attributed to non-uniform mixing of the inlet flows before flowing into a combustor which leads to local equivalence ratio fluctuations. A small change in the equivalence ratio near a lean flammability limit is able to initiate large variations in many characteristics of flame such as a flame speed, a flame temperature, and a chemical time. The experimental data obtained by Zukoski [9], shown in Fig.1.10 indicates that the gradient of chemical reaction time with respect to equivalence ratio ( $\frac{\partial \tau_{\text{chem}}}{\partial \phi}$ ), increases significantly as the flame gets leaner. Since the chemical reaction time is inversely proportional to the reaction rate, a small variation in the equivalence ratio can create large fluctuations in the reaction rate at lean conditions, as compared to the stoichiometric condition. As a result, the pressure oscillations will grow stronger with definite amplitude when the fluctuations of the reaction rate are coupled with the acoustic of the combustor system, making a closed loop of nonlinear energy exchanges mechanism [10].



**Figure 1.10:** Experimentally obtained chemical reaction time as a function of the equivalence ratio of a hydrocarbon fuel with a molecular weight of about 100 (Zukoski [9]).



**Figure 1.11:** Schematic drawing of the time evolutions of perturbations responsible for driving combustion instabilities [10]).

This mechanism is illustrated in Fig.1.11. Three time delay between acoustic waves and heat's oscillations are considered. Acoustic waves, originating from the combustion chamber, travel upstream and modulate the fuel and air mass flows in the injectors with a time delay  $\tau_1$ . The time that fuel occupies to travel from injector to combustion chamber generate time delay  $\tau_{conv}$ . These time delays, together with  $\tau_{chem}$  due to variation of  $\phi$ , generate an out of phase loop between heat release and acoustic waves and it can form an oscillatory combustion. The possibility of forming such large amplitude  $\phi$  oscillations from modest flow perturbations suggests that even though diffusive and turbulent mixing processes will tend to homogenize the mixture as it flows from the fuel injector towards the combustor, the equivalence ratio perturbations may still persist at the flame. The assessment of the effects of premixing on combustion instability is quite important for the design of LPP combustors since the degree of premixing also effects the emission characteristic of combustors, flame structures and the local distributions of an equivalence ratio at a fuel nozzle. In light of these facts, extensive efforts have been made worldwide in the industrial, government, and academic communities to understand the unique stability characteristics of low emission lean-premixed gas turbine engines.

## 1.4 SUPPRESSION METHODS

In order to eliminate combustion oscillations the coupling between acoustic waves and unsteady heat release must be interrupted. Two types of approaches are proposed: active and passive control techniques. Passive control involves changes of fuel or hardware design (for example, in the composition or types of reactants, fuel injection devices and chamber geometry, or the installation of acoustic dampers), either to reduce the rate at which energy is transferred to unsteady motions, or to increase losses of energy, such as by the use of suitable resonators to introduce a dissipative process [1]. In contrast to passive control, active type control is can be used, but it involves expenditure of energy from a source external to the system. Generally, the purpose is to minimize the difference or "error" between the instan-

taneous desired and actual behaviour of the system. Active control may involve sensing the instabilities and then using a feedback control loop to modify one or more input parameters, which consequently interrupts the coupling between unsteady heat release and acoustic waves. Both passive and active control techniques have been successfully applied in instability control in many combustion systems. A wide description of these techniques has been made by Huang and Yang [11] and by Culick [12].

---

# 2 THERMOACOUSTIC THEORY

---

A sound wave in a gas is usually regarded as consisting of coupled pressure and motion oscillations, but temperature oscillations are always present, too. When the sound travels in small channels, oscillating heat also flows to and from the channel walls. The combination of all such oscillations produces a rich variety of "thermoacoustic" effects. Research in thermoacoustics began with simple curiosity about the oscillating heat transfer between gas sound waves and solid boundaries. These interactions are too small to be obvious in the sound in air with which we communicate every day. However, in intense sound waves in pressurized gases, thermoacoustics can be harnessed to produce powerful engines, pulsating combustion, heat pumps, refrigerators, and mixture separators. Hence, much current thermoacoustics research is motivated by the desire to create new technology for the energy industry that is as simple and reliable as sound waves themselves. The first observation of combustion oscillation is the "singing flame" described by Higgins in 1777 [13]. After that several researchers started to analyze the phenomenon and they described that high levels of sound could be produced by a flame. In 1878 Lord Rayleigh was the first to hypothesized the onset of instability and to define a criterion based on a phenomenological and heuristic description of the instability. He quoted: *"If heat be given to the air at the moment of greatest condensation, or be taken from it at the moment of greatest rarefaction, the vibration is encouraged. On the other hand, if heat be given at the moment of greatest rarefaction, or abstracted at the moment of greatest condensation, the vibration is discouraged"* [14][15]. This paragraph gives the so-called Rayleigh criterion for the occurrence of combustion instability. The spontaneous acoustic oscillations that Rayleigh explained in this way included simple case that the Sondhauss oscillation and the Rijke tube [16], which are essentially open tubes with either nothing inside (Sondhauss) or a simple gauze inside (Rijke), heated at one location by a flame and held elsewhere at ambient temperature.

## 2.1 RAYLEIGH CRITERION

Many researchers restated the ideas of Lord Rayleigh, highlighting the importance of the phase between the unsteady heat release and the pressure oscillations in the onset of instability. Qualitatively the criterion states that if the oscillations of pressure and heat release are in phase energy is supplied to the oscillatory flow field, otherwise energy is subtracted from the system. The Rayleigh criterion is best defined as the following inequality:

$$\int_0^{\tau} \int_0^V p'(x, t) q'(x, t) dv dt > \int_0^{\tau} \int_0^V \Phi(x, t) dv dt \quad (2.1)$$

where  $p'$  and  $q'$  are the pressure and heat release fluctuations respectively,  $\tau$ ,  $V$  and  $\Phi$  are the period of oscillation, the control volume (the volume of the combustor) and the wave energy dissipation respectively. When the inequality in eq.(2.1) is satisfied, thermoacoustic instability occurs. The LHS of the inequality represents the total mechanical energy added to the oscillations by the heat addition process per cycle. The RHS of the inequality represents the total energy dissipated by the oscillation per cycle. The acoustic dissipations inside the combustor are usually very small, so that the LHS has more importance. Assuming that  $p'$  and  $q'$  have a periodic time dependence, the sign of the time integral in the LHS depends on the ratio  $\frac{\tau_0}{\tau}$ , where  $\tau_0$  is the phase difference between  $p'$  and  $q'$ . When  $\frac{\tau_0}{\tau} = 0, 1, 2, \dots$  the integral has a positive maximum, whereas when  $\frac{\tau_0}{\tau} = 1/2, 3/2, \dots$  the integral has a negative minimum. This agrees with Lord Rayleigh's hypotheses: when  $p'$  and  $q'$  are in phase, instability occurs; when  $p'$  and  $q'$  are out of phase, stabilization occurs. Since the integral in eq.(2.1) is both temporal and spatial, stabilization and destabilization can occur in different locations inside the combustor.

### 2.1.1 Analytical Derivation of the Rayleigh Criterion

The acoustic energy density  $e'$  in a one-dimensional acoustic field can be derived from the unforced conservation equations as:

$$e' = \frac{\bar{\rho}u'^2}{2} + \frac{p'^2}{2\rho c^2}, \quad (2.2)$$

where  $\frac{\bar{\rho}u'^2}{2}$  is the kinetic acoustic energy and  $\frac{p'^2}{2\rho c^2}$  is the potential acoustic energy. Any system that would sustain waves should have these energy components and the periodic conversion from one form to the other sustains the oscillations. The momentum and energy conservation for a zero mean velocity and without any spatial dependence can be written as:

$$\bar{\rho} \frac{\partial u'}{\partial t} + \frac{\partial p'}{\partial x} = 0 \quad (2.3)$$

$$\frac{\partial p'}{\partial t} + \gamma \bar{p} \frac{\partial u'}{\partial x} = (\gamma - 1)q'. \quad (2.4)$$

Multiplying eq.(2.3) by  $u'$  and eq.(2.4) by  $\frac{p'}{\gamma \bar{p}}$ , summing these two terms and using eq.(2.2)), the following equation is obtained:

$$\frac{\partial e'}{\partial t} + u' \frac{\partial p'}{\partial x} + p' \frac{\partial u'}{\partial x} = \frac{\gamma - 1}{\rho c^2} p' q'. \quad (2.5)$$

Integrating eq.(2.5) temporally over the period of oscillation  $\tau$  and spatially over the length  $L$  of the combustor, it is obtained:

$$\Delta_\tau \int_0^L e' dx = \frac{\gamma - 1}{\rho c^2} \int_0^\tau \int_0^L p'(x, t) q'(x, y) dx dt - \Delta_L \int_0^\tau E'_a dt - \int_0^\tau \int_0^V \Phi(x, t) dx dt, \quad (2.6)$$

where  $\Delta_\tau$  and  $\Delta_L$  are the changes over the time and the length respectively. The LHS of eq.(2.6) is the change in the acoustic energy per cross-sectional area of the combustor. The first term in the RHS is the Rayleigh integral, the second term is the acoustic energy flux across the control surface of the field with  $E'a = p'u'$ , the third term is the dissipation in the acoustic field. The energy balance in (2.6) shows that when the Rayleigh criterion is satisfied,  $p'$  and  $q'$  are in phase and the gain in the first term in the RHS is large enough to overcome the other two terms. In this situation the acoustic energy in the combustor will be dominant.

### 2.1.2 Thermodynamic Interpretation of the Rayleigh Criterion

The Rayleigh criterion can be better explained by means of a thermodynamic cycle [17]. Sound waves are isentropic, so in the  $p$ - $v$  diagram (Fig.2.1) the volume moves back and forth on an isentrope. When the heat is added or extracted periodically to the gas, an increase of the specific volume  $v$  of the gas occurs. If this heat addition is in phase with pressure oscillations, the state of the gas volume moves clockwise around a thermodynamic cycle (curve 1-2'-3'-4' in Fig.2.1). This process can be seen as a "thermoacoustic heat engine", transferring mechanical energy into sound waves, and a self-excited instability can occur. In the case in which heat release fluctuations are not perfectly in phase with pressure fluctuations, the area 1-2'-3'-4' will be smaller and the efficiency reduced. When the heat release

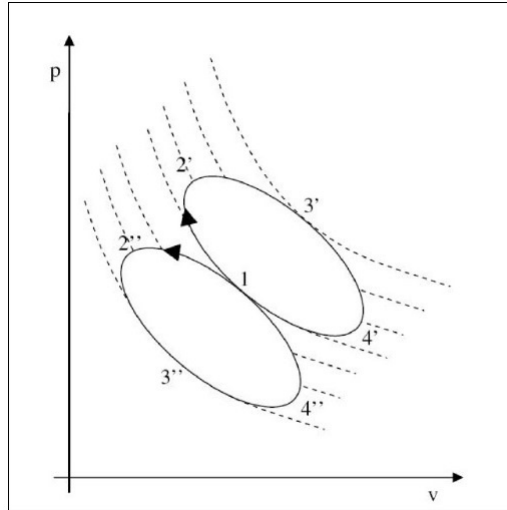


Figure 2.1: Thermodynamic interpretation of the Rayleigh criterion [1].

fluctuations are out-of-phase with pressure fluctuations, the system moves counterclockwise through the cycle 1-2''-3''-4'' and mechanical energy is extracted from the acoustic wave. The mechanical work performed by the thermodynamic cycle resulting from acoustic oscillations with heat release can be expressed as follows:

$$\oint p \, dv = \oint (\bar{p} + p') \, d(\bar{v} + v') = \oint \bar{p} \, dv' + \oint p' \, dv' = 0 + \oint p' \, dv'. \quad (2.7)$$

In eq.(2.8) the specific volume  $v'$  is split into an isotropic part, for which  $v' = -\frac{(vdp')}{\gamma p}$ , and a part  $v'^{(q)}$  due to heat addition (or removal):

$$\oint p' dv' = -\frac{v}{\gamma p} \oint p' dp' + \oint p' dv'^{(q)} = 0 + \oint p' \frac{dv'^{(q)}}{dt} dt \sim \oint p' q' dt. \quad (2.8)$$

The rate of change of  $v'$  in time is proportional to heat release perturbations. So the work done by the "thermoacoustic engine" is positive (energy added to acoustics) if the integral of  $p'q'$  is positive over one period of oscillation, as suggested by Rayleigh. If the losses of acoustic energy exceed the rate of energy input to the acoustic field by the fluctuating flame, a self-excited instability cannot develop, even if  $p'$  and  $q'$  are in phase. This is why the Rayleigh criterion is a necessary, but not a sufficient criterion for instability to occur [17].

## 2.2 MATHEMATICAL MODEL

The acoustic analysis is based on the resolution of the wave equation. It is derived from the linearized equations of the perturbations. In the case of a compressible viscous fluid in the absence of external forces, the Navier-Stokes equations are obtained from the conservation of mass and momentum:

$$\frac{D\rho}{Dt} + \rho \nabla \cdot \mathbf{u} = 0, \quad (2.9)$$

$$\rho \frac{D\mathbf{u}}{Dt} = -\nabla p + \frac{\partial \sigma_{ij}}{\partial x_j} \mathbf{e}_i, \quad (2.10)$$

where  $p$  is the pressure,  $\rho$  the density,  $\mathbf{u}$  is the velocity vector,  $\sigma_{ij}$  is the viscous stress tensor and  $\mathbf{e}_i$  is the unit vector in the direction  $i$ .  $D = Dt$  is the material derivative and it is defined as  $\frac{\partial}{\partial t} + \mathbf{u} \cdot \nabla$ . If the fluid is considered as a perfect gas, the gas law is introduced:

$$\frac{p}{\rho} = R_g T, \quad (2.11)$$

where  $T$  is the temperature and  $R_g = c_p - c_v$  is the gas constant with  $c_p$  and  $c_v$  the specific heats at constant pressure and constant volume respectively. The internal energy  $e$  is equal to  $c_v T$ , whereas the enthalpy  $h$  is equal to  $e + p\rho$ . Conservation of energy is defined as:

$$\rho \frac{D}{Dt} \left( e + \frac{1}{2} \mathbf{u}^2 \right) = -\nabla \cdot (p\mathbf{u}) + q + \nabla \cdot (K\nabla T) + \frac{\partial}{\partial x_j} (\sigma_{ij} u_i), \quad (2.12)$$

where  $K$  is the conductivity and  $q$  is the rate of heat added to the fluid per unit volume. Introducing the conservation of momentum, eq.(2.10), eq.(2.12) can be rearranged as:

$$\rho \frac{Dh}{Dt} = \frac{Dp}{Dt} + q + \nabla \cdot (K\nabla T) + \sigma_{ij} \frac{\partial u_i}{\partial x_j}. \quad (2.13)$$

Entropy  $S$  is defined by the thermodynamic relation  $dh = TdS + (\frac{1}{\rho})dp$ , so that eq.(2.13) yields:

$$\rho T \frac{DS}{Dt} = q + \nabla \cdot (K \nabla T) + \sigma_{i,j} \frac{\partial u_i}{\partial x_j}, \quad (2.14)$$

where it is clear that entropy is increased by heat input, heat transfer and viscous effects. The flow is assumed to be unviscid, so  $\sigma_{i,j} = 0$ . Additionally, the fluid is assumed to be an ideal gas, which, added to the hypothesis of perfect gas, means that the specific heats are constant. From the definition of entropy,  $S = c_v \log \frac{p}{\rho^\gamma}$ , where  $\gamma = \frac{c_p}{c_v}$  is the ratio of specific heats. The flow is considered to be composed of a steady uniform mean flow (identified by an overbar) and a small perturbation (identified by a prime):

$$p(\mathbf{x}, t) = \bar{p} + p'(\mathbf{x}, t) \quad (2.15)$$

and the same for the other variables. Applying these hypotheses to eqs.(2.9),(2.10) and (2.14), the linearized equations for the perturbations are obtained:

$$\frac{D\bar{\rho}'}{Dt} + \bar{\rho} \nabla \cdot \mathbf{u}' = 0, \quad (2.16)$$

$$\frac{D\bar{\mathbf{u}}'}{Dt} + \frac{1}{\bar{\rho}} \nabla p' = 0, \quad (2.17)$$

$$\bar{\rho} T \frac{DS'}{Dt} = q'. \quad (2.18)$$

Combining eqs.(2.16), (2.17) and (2.18) and considering that  $S' = c_v \frac{p'}{\bar{p}} - c_p \frac{\rho'}{\bar{\rho}} = 0$ , the inhomogeneous wave equation is obtained:

$$\frac{1}{\bar{c}^2} \frac{D^2 p'}{Dt^2} - \nabla^2 p' = \frac{\gamma - 1}{\bar{c}^2} \frac{Dq'}{Dt}, \quad (2.19)$$

where  $c$  is the speed of sound.

Since in gas turbine combustion chamber the flow velocity is generally far below the sound velocity, the flow velocity  $\bar{\mathbf{u}}$  can be generally considered negligible. Under such hypothesis, the inhomogeneous wave equation in eq.(2.19) becomes:

$$\frac{1}{\bar{c}^2} \frac{\partial^2 p'}{\partial t^2} - \nabla^2 p' = \frac{\gamma - 1}{\bar{c}^2} \frac{\partial q'}{\partial t}. \quad (2.20)$$

The acoustic analysis of a gas turbine combustion chamber is based on the resolution of equation (2.20), with the appropriate boundary conditions. The estimated frequencies of oscillations obtained from the above classical acoustics analysis commonly lie within 10 – 15% or less of the frequencies observed in experiments for combustion instabilities (Culick [18]). It is precisely the departure; however, from classical acoustics that defines the class of problems we call combustion instabilities. According to Culick, there are three main reasons why the classical view of acoustics is a good first approximation to wave propagation in the combustion chamber. First, the Mach number of the mean flow is usually so low that convective and

refractive effects are small. Second, if the exhaust nozzle is choked, the incident waves are efficiently reflected, and the exit plane can be regarded as a rigid surface, acoustically. Third, in the limit of small-amplitude disturbances, the unsteady motion in the compressible flow can be decomposed into three independent modes of propagation: acoustic, vortical and entropy waves. Even in the highly turbulent non-uniform flow usually present in a combustion chamber, acoustic waves behave according to their own simple classical laws. The role of the classical linear acoustic analysis should not, however, be exaggerated. It cannot decide which modes of acoustic oscillations will be excited, nor is it able to predict the amplitude of the excited modes.

### 2.3 EFFECT OF THE MEAN FLOW

Since the Mach number of the inlet flow is usually small, it can be possible to neglect the mean flow velocity. In so doing the error is not so large, but the mean flow has two important consequences. It influences the propagation velocity of the acoustic waves, with the one-dimensional wave travelling downward with velocity  $\bar{c} + \bar{u}$  and upward at  $\bar{c} - \bar{u}$ . Then the mean flow determines the existence of the entropy and vorticity waves. Eq.(2.20) is written when  $\bar{u} = 0$ , whereas in the case of  $\bar{u} \neq 0$  the partial derivatives for pressure  $p'$  and heat release  $q'$  are substituted by material derivatives, which consider the effect of the mean flow velocity:  $\frac{D}{Dt} = \frac{\partial}{\partial t} + \mathbf{u} \cdot \nabla$ . The expression for the inhomogeneous wave equation in this case is:

$$\frac{1}{\bar{c}^2} \frac{D^2 p'}{Dt^2} - \bar{\rho} \nabla \cdot \left( \frac{1}{\bar{\rho}} \nabla p' \right) = \frac{\gamma - 1}{\bar{c}^2} \frac{Dq'}{Dt}. \quad (2.21)$$

Many numerical tests on 3D FEM code are demonstrated that low Mach number have a small influence on results [1] confirming what was found by Dowling and Stow [19] for a configuration without unsteady heat release. Test in a simple tube shows that the growth rate decreases following a quasi-linear trend with Mach number, highlighting the damping effect of the mean flow inside the duct since the stability of the mode is increased with the Mach number. The error in neglecting the mean flow velocity inside a cylindrical duct is very low for the frequencies: up to 7% for  $M = 0.2$ , while for the growth rate the error determines a more conservative analysis [1].

---

# 3

## NUMERICAL MODEL

---

Combustion instability's prediction is a very complex issue and, over the years, several different approaches have been developed to model as well as possible this phenomenon. These approaches can be grouped into three different categories: low order models, CFD (computational fluid dynamics) models and Helmholtz solvers. Low order models define the combustor system as a series of subsystems, using mathematical transfer function matrices to connect these lumped acoustic elements one to each other. In this scheme flame is concentrated in one of the lumped elements and located at the beginning of the combustion chamber. Acoustically the phenomenon is correctly investigated if simplified schemes, such as a simple pipe section, are examined. When complex elements are involved, these models become inexact and make use of assumptions and empirical data. CFD codes include URANS and LES which theoretically detect all the main effects. Particularly LES codes are proposed in order to investigate the phenomenon of combustion instability and matching pressure oscillations with turbulent combustion phenomena, even though they require large numerical resources. In order to overcome some of the limitations of the previous techniques, an approach making use of Helmholtz solver is introduced. Three-dimensional geometries can be examined and complex eigenfrequencies of the system can be detected. This approach solves numerically the differential equation problem converted in a complex eigenvalue problem in the frequency domain. The eigenvalue problem is non-linear and is solved by means of a linearization under the hypothesis of small oscillations. From the complex eigenvalues of the system it is possible to ascertain if the corresponding mode is unstable or if the oscillations will decrease in time, i.e. the mode is stable. By means of this approach it is possible to examine a spatially distributed flame inside the whole combustion chamber and not only a simplified flame sheet after the burners.

### 3.1 FLAME MODEL

Despite the analytical integral form, Rayleigh criterion is still difficult to apply because no explicit information about frequency spectrum or flame shape is available. Hence, fulfillment of eq.(2.1) should be verified for every possible frequency spectrum and any flame shape admitted by the equations of motion. This control is practically impossible so that, as of now, Rayleigh criterion is correct but useless. This is the reason why different authors provided different methods to take into account thermoacoustic interactions. Indeed, there are several mechanisms leading to instability, and, correspondingly, many competing theories are available. In Ansaldo Energia, in agreement with several academic studies, to model heat release fluctuations, Flame Transfer Function (FTF) approach is used. FTF is defined

as the ratio of heat release rate oscillation to inlet velocity's or pressure's fluctuations, where all of them are normalized by their corresponding time-averaged values (Fig.3.1). In this way relation between pressure/velocity and heat release is

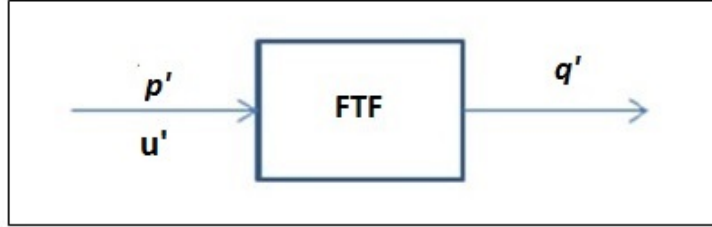


Figure 3.1: Flame Transfer Function approach.

determined. FTF can be obtained experimentally or numerically. In second case combined use of finite-volume and finite-element codes is requested. In particular, results obtained with one code are used as input into the other to find the Flame Transfer Function. This numerical method could be very good but the enormous computational effort of a precise finite-volume analysis limits the number of interactions between the two codes. However given the good results obtained by using COMSOL Multiphysics, this software was adopted by Ansaldo to investigate the combustion instability.

### 3.1.1 Linear flame model

Many types of combustion response models can be found in literature. One of the commonly used is the time delay model ( $n-\tau$  formulation), which has been extensively employed to study combustion instabilities in liquid-propellant rocket engines (Crocco and Cheng [20]). The model globally describes the dynamic relationship between fuel injection and heat release, and can be briefly summarized as follows (Culick [21]). Suppose that at time  $t$ , the pressure in the chamber suddenly decreases, causing an increase in the flow of fuel through the injector. The increased mass is convected downstream to the flame front and burns at some later time  $t + \tau$ , where  $\tau$  is the time delay. The time scales that contribute to the time delay are the convection time needed to travel the distance from the fuel injection location to the flame front, the mixing time for fresh air and fuel to mix with hot product gases, and the chemical time corresponding to the ignition delay. The time delay can have a single value in the entire flame zone or a time delay distribution can be considered. This latter case permits to create a more realistic model of a gas turbine burner flame. The fluctuating heat release may depend on both the pressure and the velocity, additionally allowing for a time delay. Since in gas turbines the influence of the pressure fluctuations can be neglected [17], it is chosen a flame model with heat release fluctuations coupled to the velocity fluctuations  $u'$  with a time delay. In the linear case and in the time domain it means [1]

$$\frac{q'}{\bar{q}} = -k \frac{u'(t - \tau)}{\bar{u}} \quad (3.1)$$

where  $k$  is the interaction index, which represents a dimensionless parameter of proportionality between the heat release fluctuations and the velocity fluctuations. The fluctuating variables can be expressed by complex functions of time and position with a sinusoidal form:  $q' = \hat{q}e^{(i\omega t)}$  and  $u' = \hat{u}e^{(i\omega t)}$ , so that the linear flame model in the frequency domain can be written as

$$\frac{\hat{q}}{\bar{q}} = -k \frac{\hat{u}}{\bar{u}} e^{-i\omega\tau}. \quad (3.2)$$

The linear flame transfer function used in linear-mode calculations is so defined by

$$\text{FTF}_L(\omega) = \frac{\hat{q}/\bar{q}}{\hat{u}/\bar{u}} = -ke^{(-i\omega\tau)}. \quad (3.3)$$

### 3.2 COMSOL'S APPROACH

Instability analysis is carried out by using commercial software, Comsol Multiphysics, based on the finite element method (FEM). Three-dimensional geometries can be examined and complex eigenfrequencies of the system can be detected. This approach numerically solves the differential equation problem converted in a complex eigenvalue problem in the frequency domain and the stability analysis can be conducted. The fluid is regarded as an ideal gas and flow velocity is considered negligible. The effects of viscosity, mean flow, thermal diffusivity and heat transfer with walls are neglected, the mean pressure is assumed uniform in the domain. Under such hypotheses, in presence of heat fluctuations, the inhomogeneous wave equation (2.20) is obtained. Neglecting the effects of the temperature variation, no entropy waves are considered and the pressure fluctuations are related to the velocity fluctuations by

$$\frac{\partial \mathbf{u}'}{\partial t} + \frac{1}{\rho} \nabla p' = 0. \quad (3.4)$$

The COMSOL module considered is "pressure acoustics". For the search of the eigenvalues and the eigenmodes of the system, the analysis is performed in the frequency domain and the fluctuating variables are expressed by complex functions of time and position with a sinusoidal form:  $p' = \hat{p}e^{(i\omega\tau)}$ , where  $\omega = \omega_r + i\omega_i$  is the complex frequency. Its real part  $\omega_r$  gives the frequency of oscillations, while the imaginary part  $-\omega_i$  provides the growth rate at which the amplitude of the oscillations increases per cycle. The solving equation for the "pressure acoustics" module is slightly different from the inhomogeneous wave equation provided in eq.(2.20)

$$\frac{\lambda^2 \hat{p}}{\bar{c}^2 \bar{\rho}} - \frac{\nabla^2 \hat{p}}{\bar{\rho}} = Q^{\text{CM}} \quad (3.5)$$

where  $\lambda = -i\omega$  is the eigenvalue.  $Q^{\text{CM}}$  is the monopole source defined in the "pressure acoustics" module, which is related to  $\hat{q}$ . Dividing eq.(2.20) by density, remembering that the fluctuating variables can be expressed as

$$\mathbf{p}' = \Re(\hat{\mathbf{p}}(\mathbf{x})e^{i\omega t}), \quad (3.6)$$

$$\mathbf{u}' = \Re(\hat{\mathbf{u}}(\mathbf{x})e^{i\omega t}), \quad (3.7)$$

$$\mathbf{q}' = \Re(\hat{\mathbf{q}}(\mathbf{x})e^{i\omega t}), \quad (3.8)$$

and setting  $\lambda = -i\omega$ , the inhomogeneous wave equation becomes:

$$\frac{\lambda^2}{\rho c^2} \hat{\mathbf{p}} - \frac{\nabla^2 \hat{\mathbf{p}}}{\bar{\rho}} = -\frac{\gamma - 1}{\rho c^2} \lambda \hat{\mathbf{q}}. \quad (3.9)$$

Comparing eq.(3.5) and eq.(3.9), the correspondence between  $Q^{\text{CM}}$  and  $\hat{\mathbf{q}}$  is obtained [1]:

$$Q^{\text{CM}} = -\frac{\gamma - 1}{\rho c^2} \lambda \hat{\mathbf{q}}. \quad (3.10)$$

Eq.(3.9) shows a quadratic eigenvalue problem that can be solved by means of an iterative linearization procedure. COMSOL uses the ARPACK FORTRAN as numerical routines for large-scale eigenvalue problems. An iterative procedure based on a quadratic approximation around an eigenvalue linearization point  $\lambda_0$  is adopted. Such a procedure is speeded up by using, as approximate starting eigenvalue, the value obtained through the analysis of the system without heat release fluctuations. The solver reformulates the quadratic eigenvalue problem as a linear eigenvalue problem of the conventional form  $\mathbf{A}\mathbf{x} = \lambda\mathbf{B}\mathbf{x}$  and iteratively updates the linearization point until convergence is reached. A direct solver is used for all the cases. This direct solver works on general matrix systems using multifrontal method and direct LU factorization of the sparse matrix  $\mathbf{A}$ .

### 3.2.1 Test case 1: cylindrical configuration

In order to obtain the expression of the monopole source to insert in COMSOL in the case of a linear flame model, the paper by Dowling and Stow [19] is taken as bench-mark. A series of examples is solved by means of a one-dimensional acoustic network code. In the acoustic network approach the unsteady heat release is assumed to be concentrated at a single axial plane  $x = b$ , called flame sheet and it is also:

$$\mathbf{q}'(x, t) = Q'(t)\delta(x - b), \quad (3.11)$$

where  $Q'(t)$  is the rate of heat release per unit area, assumed to be related to the oncoming air velocity there with a time delay, and the term  $\delta(x - b)$  is the Dirac delta, denoting the reciprocal of the thickness of the flame sheet. Fig.3.2 shows the geometrical configuration. In the 3D FEM approach it is not possible to consider the heat release as a flame sheet, so that a thin region for the heat input is considered, as shown in Fig.3.2. As a consequence, the term  $\delta(x - b)$  is defined as:

$$\delta(x - b) \simeq \begin{cases} 0 & x \leq b - \frac{s}{2} \\ \frac{1}{s} & b - \frac{s}{2} < x \leq b + \frac{s}{2} \\ 0 & x > b + \frac{s}{2} \end{cases} \quad (3.12)$$

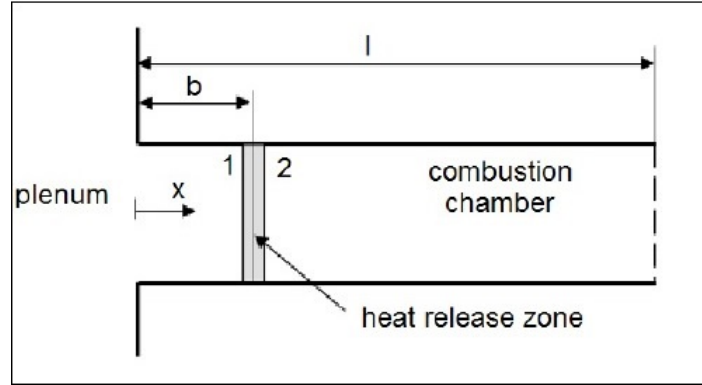


Figure 3.2: Simplified scheme of flame location in a straight duct with uniform cross section [1].

where  $s$  is the thickness of the heat release zone and  $b$  is its axial location [1]. If we assume for  $Q'/\bar{Q}$  the following expression:

$$\frac{Q'}{\bar{Q}} = -k \frac{u'}{\bar{u}} (t - \tau) \quad (3.13)$$

which is of the same form of eq.(3.1), considering that:

$$\bar{Q} = \bar{\rho} \bar{u} c_p \Delta T \quad (3.14)$$

substituting  $Q'$  in eq.(3.11), considering expression of eqs.(3.6) (3.7) (3.8) and finally using eq.(3.10), the following equation is obtained:

$$Q^{CM} = k \lambda \hat{u} \delta(x - b) e^{\lambda \tau} \quad (3.15)$$

where  $\lambda$  is the eigenvalue and all the other constant values that does not appear are included in  $k$ . Eq.(3.15) is the monopole source in COMSOL when a linear flame model related to the velocity is used. The velocity is evaluated on the section immediately before the flame.

To confirm this approach, Comsol's results are compared with analytical solution proposed by Dowling and Stow to find complex eigenvalues:

$$\tan(K_1 b) \tan[K_2 (x - b)] = \left( \frac{\bar{\rho}_2 \bar{c}_2}{\bar{\rho}_1 \bar{c}_1} \right) [1 - \beta e^{(-i\omega\tau)}] \quad (3.16)$$

where the subscript 1 refers to the domain upstream the flame at temperature  $T_1$  and subscript 2 refers to the domain downstream the flame at temperature  $T_2 > T_1$ .  $K_i = \frac{\omega}{c}$  is the wave number. In this test case  $T_1 = T_2$ . A comparison from 3D FEM code's results and analytical solution of eq.(3.16) are illustrated in Fig.3.3 [1]. Good agreement between analytical and numerical results confirms the accuracy of Comsol's approach and the possibility to use this model for combustion instability prediction.

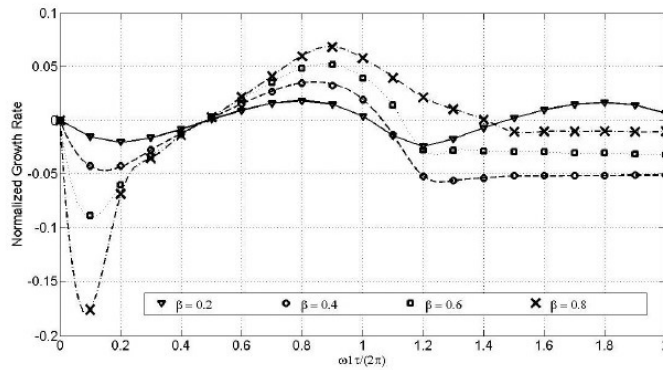


Figure 3.3: Variation with  $\tau$  of the growth rate for the first mode of the duct in Fig. 3.2 ( $b = 1/10$ )[1].

### 3.2.2 Test case 2: annular configuration

At the beginning, results obtained by Campa [1] in simplified annular combustion chamber proposed in [51] are reproduced. For this example a linear flame model is used to evaluate the influence of heat release and of time delay on the system. Fig.3.4 shows the configuration of simplified annular combustion chamber while geometry details are reported in Tab.3.1. The combustor is characterized by a diffusion chamber ring (plenum) and an annular combustion chamber linked by 12 cylindrical burners. The flame is modelled with a heat source in a finite volume at the end of the burners (Fig.3.5) using linear flame model in eq.(3.2).

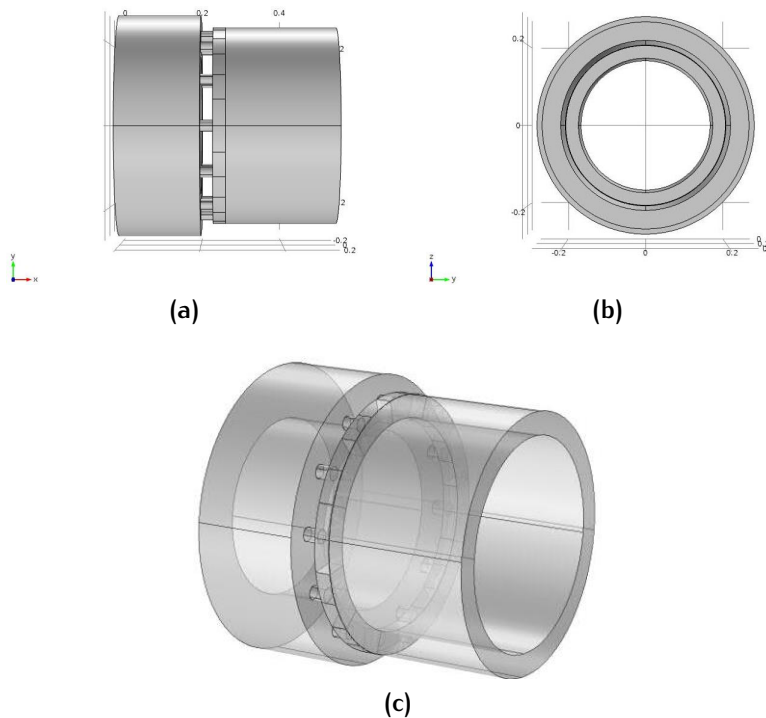


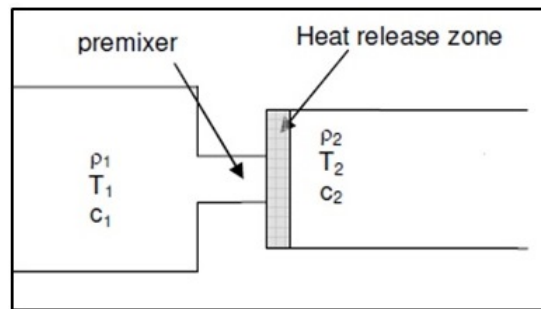
Figure 3.4: Simplified annular combustion chamber; longitudinal view (a), frontal view (b) and internal view (c).

**Table 3.1:** Geometry details of simplified annular combustion chamber

Description	Value
Mean diameter	0.437 m
Length of the plenum	0.200 m
Outer diameter of the plenum	0.540 m
Internal diameter of the plenum	0.334 m
Length of the burners	0.030 m
Diameter of the burners	0.026 m
Length of the combustion chamber	0.300 m
Outer diameter of the combustion chamber	0.480 m
Internal diameter combustion chamber	0.394 m

**Table 3.2:** Operating conditions

Description	Value	Unit
$\rho_1$ Plenum density	0.450	kg/m <sup>3</sup>
$\rho_2$ Combustion chamber density	0.148	kg/m <sup>3</sup>
$u_1$ Plenum flow velocity	6.116	m/s
$u_2$ Combustion chamber flow velocity	33.360	m/s
$c_1$ Plenum sound velocity	556	m/s
$c_2$ Combustion chamber sound velocity	945.2	m/s
$T_1$ Plenum temperature	770	K
$T_2$ Combustion chamber temperature	2000	K
$\phi$ Equivalent ratio	0.69	
$P$ Thermal power	1020	W

**Figure 3.5:** Simplified scheme of flame location and boundary conditions, for benchmark tests on straight duct with variation of section.

At operating condition reported in Tab.3.2, first four modes are studied (Fig.3.6). The first mode is a pure axial mode, the second one is a circumferential mode that involves only the plenum where the largest pressure oscillations can be seen. The third mode is a coupled axial-circumferential mode where the largest oscillations occur in the combustion chamber. The fourth mode is a circumferential mode of the second order that involves only the plenum. The eigenfrequencies are normalized with the frequency  $f_0 = c_0/l_0$  where  $l_0$  is the mean diameter of the chamber.

## NUMERICAL MODEL

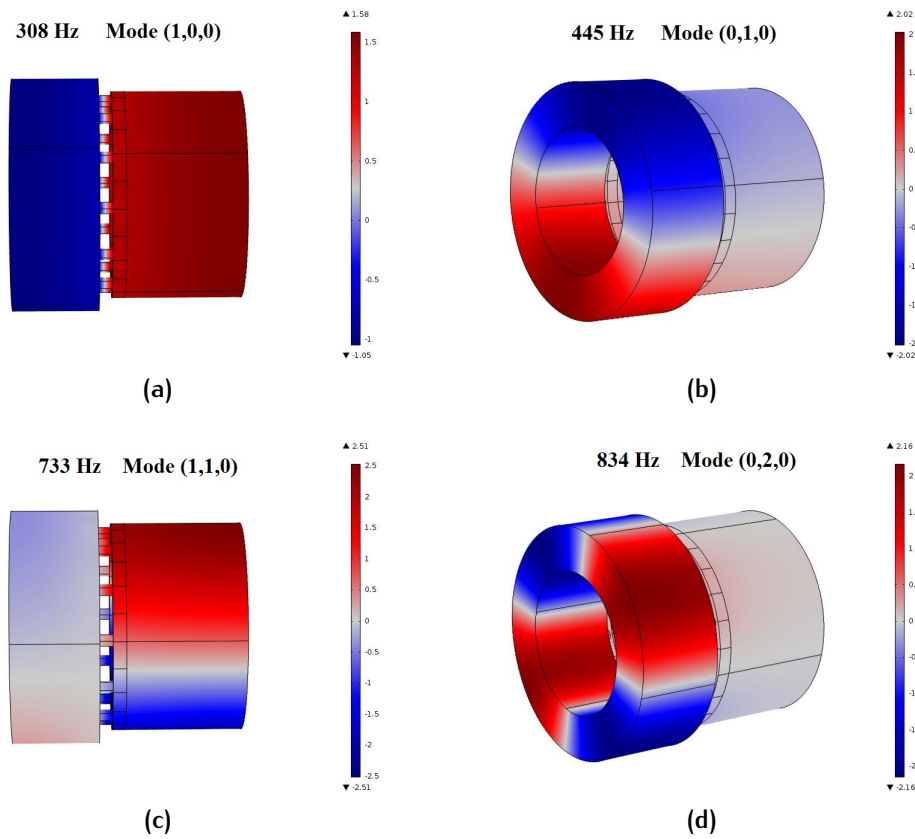


Figure 3.6: First four acoustic eigenmodes of the combustor.

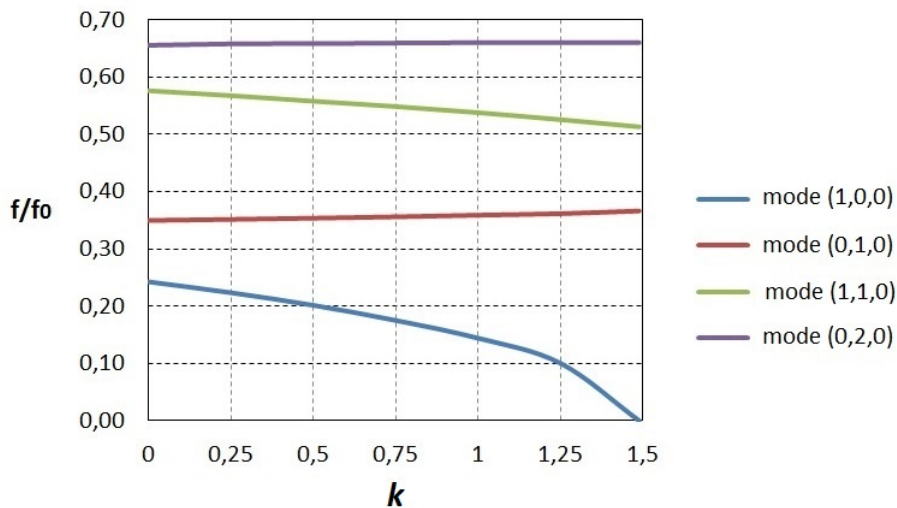
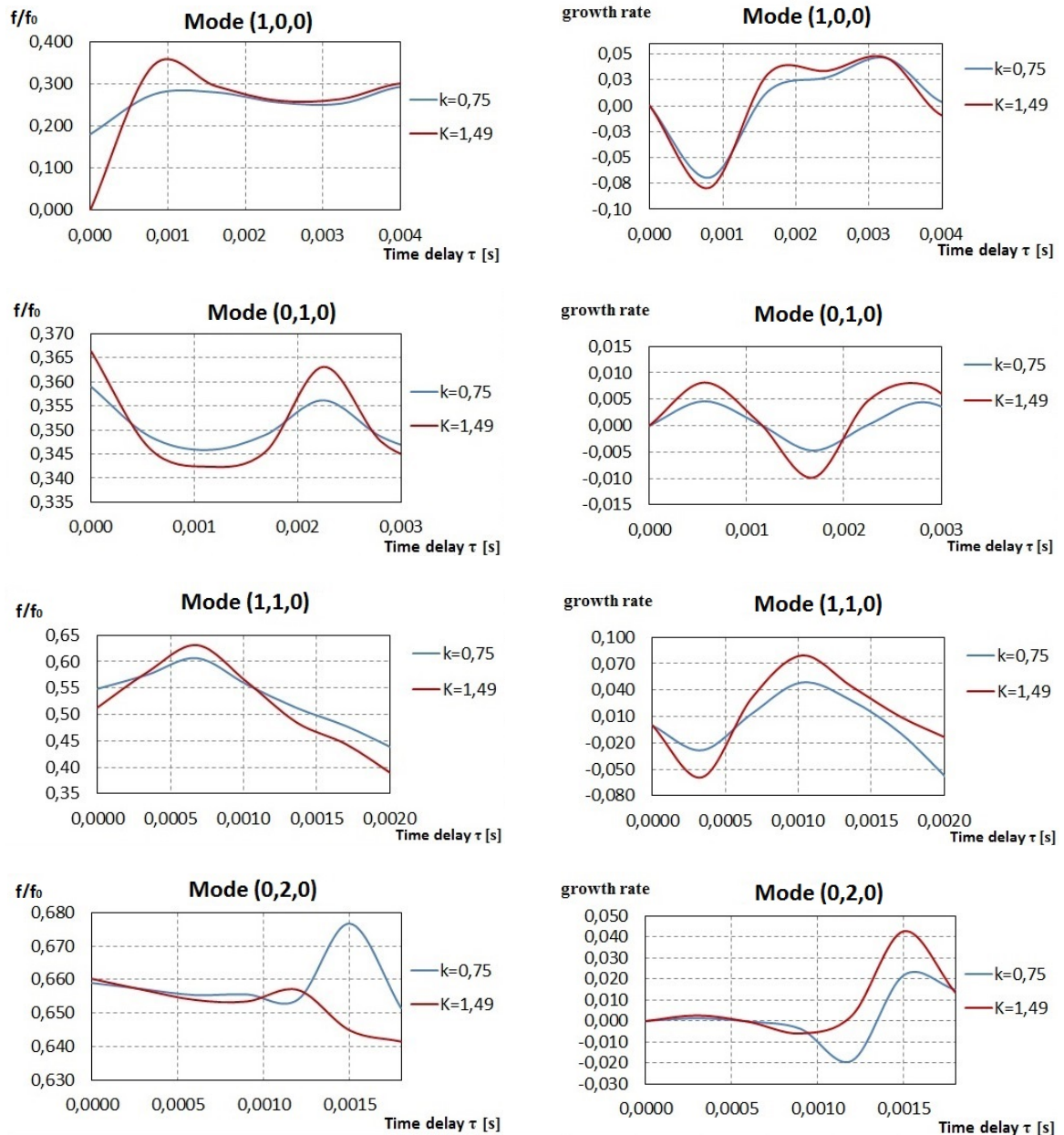


Figure 3.7: Variation with  $k$  of the normalized frequencies of the annular combustion chamber.  $\tau = 0$  s.

The modes are denoted with the nomenclature  $(l_a, m_a, n_a)$ , where  $l_a$ ,  $m_a$  and  $n_a$  are, respectively, the orders of the pure axial, circumferential and radial modes that appear in the eigenmode obtained from simulation. At first, time delay is set equal to zero and the influence of heat release is studied (Fig.3.7). The frequency of axial

mode is strongly influenced by the variation of  $k$  and for higher values of heat release, axial mode disappears. The increase of  $k$  has, on the other hand, a lower influence on both the frequencies of the circumferential modes in the plenum, while a significant variation of the frequency is observed for the circumferential mode in the combustion chamber. At second time, time delay's influence is studied (Fig.3.8).



**Figure 3.8:** Influence of time delay on frequency (on the right) and growth rate (on the left) for the first four modes.

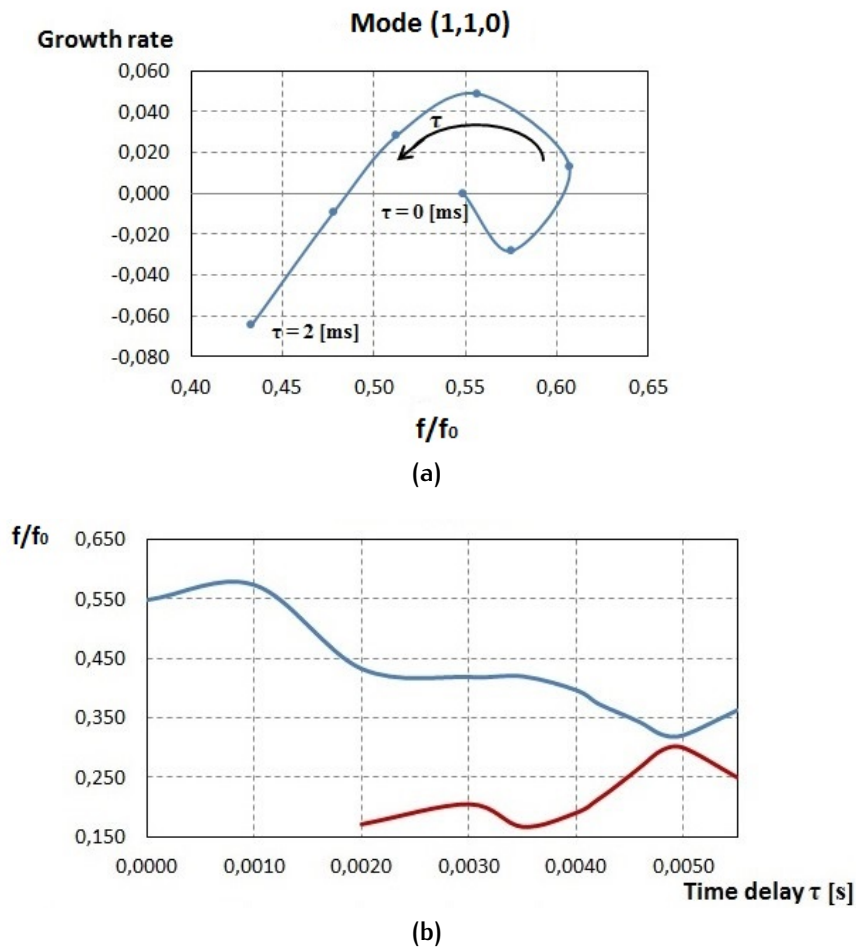


Figure 3.9: Influence of time delay on mode (1,1,0).

To increase time delay, oscillations of frequency and growth rate occur. In particular, variation between positive and negative value of growth rate shows that the time delay has an important influence on the stability of the system. This phenomenon is emphasized for higher value of  $k$ . In Fig.3.9(a) time delay influence on the mode (1,1,0) is reported: normalized frequency is the abscissa and growth rate is the ordinate.  $\tau$  is varied from 0 ms to 2 ms, with  $k = 0.75$ . As one can expect the curve described in the diagram looks like a spiral, since there is a periodicity for complex eigenfrequencies: in the frequency domain time delay is located inside an exponential. This diagram shows the importance of a correct choice of the time delay, when it is assumed to be constant in the flame model. A short change in the time delay can determine a passage from a stable to an unstable condition, and vice versa. Finally, Fig.3.9(b) shows that for higher value of time delay the same mode present two different frequencies. This phenomenon, with growth rate oscillations, is due to non-linear effect and they confirm that a nonlinear approach is needed to study combustion instability.

---

# 4 NONLINEAR ANALYSIS

---

In real life, in engineering, in nature and in society many phenomena have a nonlinear behaviour and these appear commonly to be chaotic, unpredictable or counterintuitive. Although such chaotic behaviour may resemble random behaviour, it is absolutely not random. This is due to nonlinear phenomena, which are complicated to study because most of nonlinear systems are impossible to solve analytically. For this, nonlinear systems are commonly approximated by linear equations (linearization), but this works well up to some accuracy and some range for the input values, but some interesting phenomena such as chaos and singularities are hidden by linearization. The essential difference between linear and nonlinear system is that the first can be broken down in two parts. Each part can be solved separately and finally recombined to get the answer. This is a powerful tool to study and to predict many phenomena but many things in nature don't act in this way [24]. Also nonlinear analysis allows evaluating limit cycle and bifurcation diagram of the system. Combustion instability is a typical nonlinear phenomenon. Linear techniques can predict whether a thermoacoustic system is stable or unstable but with sufficiently large perturbation thermoacoustic system can reach self-sustained oscillations and, even when it is linearly stable, a nonlinear analysis is required for predicting the self-sustained oscillations and limit cycle amplitudes. In order to get this kind of information nonlinearities is introduced inside heat release rate.

## 4.1 LIMIT CYCLE AND BIFURCATION: AN OVERVIEW

Dynamical systems theory has been often employed to study nonlinear flow and flame dynamics in combustion systems (Jahnke and Culick [22], Ananthkrishnan et al. [23]). Information can be found in the text books like the one written by Strogatz [24]. Trajectory represents the evolution in time of the system and depending on whether the system is stable or unstable a different type of trajectory is expected. Consider a one-parameter autonomous (time-invariant) nonlinear dynamical system as follows

$$\dot{\mathbf{x}} = f(\mathbf{x}, R) \quad (4.1)$$

where  $\mathbf{x}$  is the state vector variable and  $R$  is a scalar parameter. The equilibrium point  $\mathbf{x}_0$  of the autonomous system of eq.(4.1) for a given  $R$  is the real root of the equation

$$\dot{\mathbf{x}} = f(\mathbf{x}_0, R) = 0. \quad (4.2)$$

The equilibrium solution  $\mathbf{x}_0$  has the property that whenever the state of the system starts at  $\mathbf{x}_0$ , it will remain there for all future time. If the system is perturbed, in case of stable behaviour it always returns to its initial condition, while in case of

instability system's solution diverges. The stability of an equilibrium point is determined by the eigenvalues of the Jacobian matrix  $\mathbf{J} = \partial f / \partial \mathbf{x}$  evaluated at that point. For equilibrium solution to be stable all eigenvalues must have negative real parts. Dynamical systems of eq.(4.1) may have not only equilibrium solutions but also periodic solutions called limit cycles. Limit cycles are presented by isolated periodic orbits in the phase portrait of the elements of the state vector  $\mathbf{x}$ . They are inherently nonlinear phenomena, so they cannot occur in linear systems. The amplitude of a linear oscillation is set entirely by its initial conditions, and any slight disturbance to the amplitude will persist forever. In contrast, limit cycle oscillations are determined by the structure of the system itself and, if the system is slightly perturbed, it always returns to the limit cycle. The qualitative behaviour of an autonomous dynamical system is thus determined by the pattern of its equilibrium points and periodic orbits, as well as by their stability properties, which further depend on the parameter  $R$ . Depending on kind of system and on control parameter considered, three types of limit cycle can be expected (Fig.4.1). In stable type, perturbed

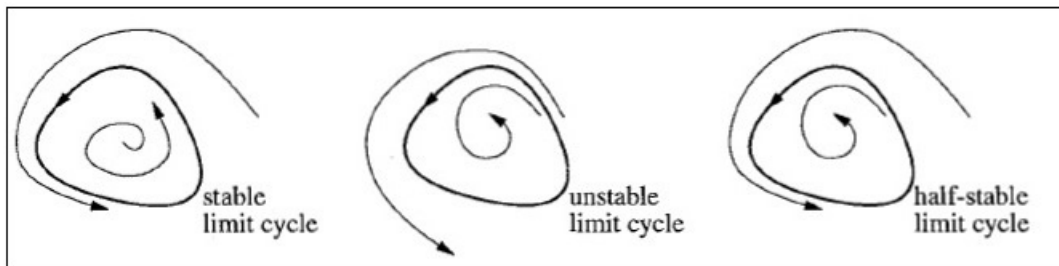


Figure 4.1: Different types of limit cycle [24].

system returns to limit cycle's oscillation while, in unstable type, system departs from limit cycle and it can converge to equilibrium point or it can diverge. If there is a neighboring trajectory which spirals into the limit cycle as time approaches infinity, and another one which spirals into it as time approaches negative infinity, a semi-stable limit cycle occurs. Bifurcations represent a qualitative change in behaviour of the system, and the parameter value at which they occur are called bifurcation point. They are defined as the change in the equilibrium points, or periodic orbits, or in the stability properties as the parameter  $R$  is varied. Several types of bifurcations, including saddle-node, transcritical, pitchfork, and Hopf bifurcations, are commonly observed in dynamical systems [24]. In particular, when a pair of complex-conjugate eigenvalues passes through the imaginary axis with varying values of parameter  $R$ , Hopf bifurcation takes place.

#### 4.1.1 Hopf bifurcation diagrams

In Fig.4.2 three diagrams with the same control parameter  $R$  are shown. The variable on the vertical axis is the steady state amplitude of the system, which is often the peak-to-peak amplitude of the oscillations. At low values of  $R$  there is a solution with zero amplitude, which is known as the stable solution at zero (solid line in the figure). When  $R$  reaches  $R_H$ , this solution becomes unstable. This point is known as a Hopf bifurcation point. For  $R$  greater than  $R_H$ , the solution at zero

amplitude is unstable (dashed line) and the system starts to oscillate and eventually reaches the steady state amplitude (solid line at non-zero amplitudes), which is the limit cycle or the stable periodic solution. The nonlinear behaviour around the Hopf bifurcation point determines two different types of bifurcation. The first type is the supercritical bifurcation (Fig.4.2(a)) and it is characterized by a gradual increase of the amplitude as  $R > R_H$ . For  $R < R_H$  all perturbations imposed on the system tend to decay to zero, whereas for  $R > R_H$  all the perturbations tend to reach a new stable periodic solution, that is a limit cycle equilibrium. As the control parameter  $R$  is increased, the system follows the red arrow path. As it is decreased, the system follows the blue arrow path. The second type is the subcritical bifurcation (Fig.4.2(b)) and it is characterized by a sudden increase of the steady state amplitude as  $R$  increases through  $R_H$ , reaching the limit cycle equilibrium at higher amplitudes (red arrows path). Decreasing the control parameter  $R$ , the perturbations imposed on the system reach a stable periodic solution until  $R = R_F$  with  $R_F < R_H$ , where  $R_F$  is referred to the fold point. As  $R$  decreases, through  $R_F$  all perturbations decay to zero, as shown by the blue arrow path in Fig.4.2(b). The dashed line in Fig.4.2(b), located between  $R_F$  e  $R_H$ , is known as the unstable periodic solution [24]. Fig.4.2(c) shows a particular type of subcritical bifurcation, since it is composed of an initial supercritical bifurcation with two fold points which determine the subcritical behaviour of the bifurcation diagram.

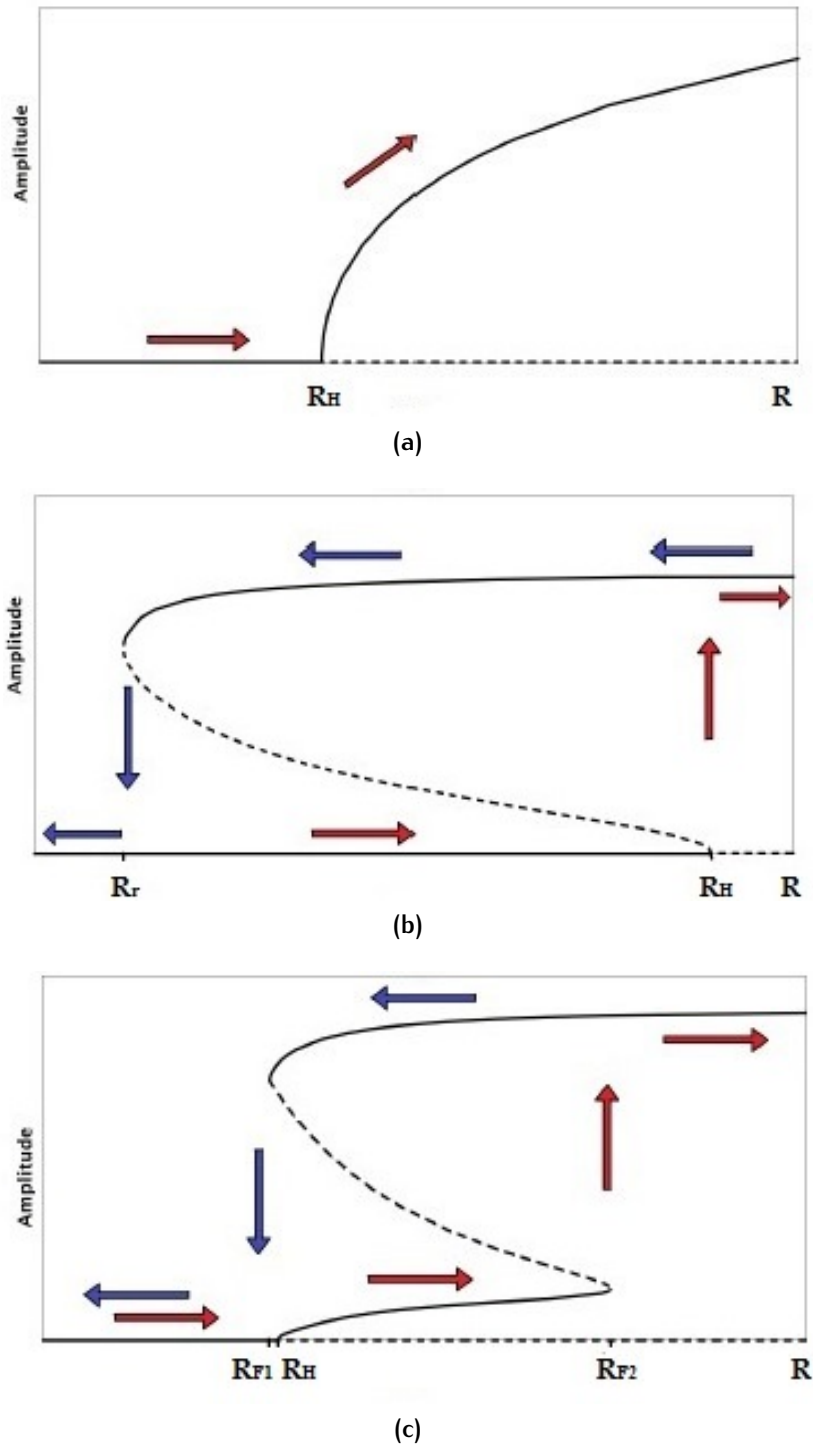


Figure 4.2: Steady state oscillation amplitude as a function of  $R$  for (a) a supercritical bifurcation and (b-c) a subcritical bifurcation (Campa [1]).

#### 4.1.2 Weakly nonlinear analysis

The appropriate analysis for determining the nature of a Hopf bifurcation point is a weakly nonlinear analysis. This has been performed before on thermoacoustic systems [25], making similar assumptions to the time averaging approach in many

of Culick's papers. It was derived also by Juniper [26], whose approach differs from others due to the use of the Maclaurin expansion. This section is entirely taken from the work by Juniper, in order to demonstrate that is possible to predict the kind of bifurcation from the analytical form of the flame model. The weakly nonlinear analysis has been performed on a generic governing equation for fluctuations around the steady state in a single mode thermoacoustic system

$$\ddot{x} + \zeta\dot{x} + x + q(x(t - \tau)) = 0. \quad (4.3)$$

The variable  $x$  can be identified with the amplitude of the fundamental mode of the velocity fluctuation,  $\eta$ , in a simple Rijke tube model [27][28] or with  $\eta$  in [29]. In line with [27][28] the damping coefficient,  $\zeta$ , appears explicitly and the heat release is velocity-coupled with a time delay  $\tau$ . One of two assumptions must be made:

- that the time delay is small compared with the oscillation period  $\chi$ , or
- that  $x$  is periodic in  $t$ .

The first of these is chosen here because it is less restrictive, so  $q(x(t - \tau)) \approx q(x - \dot{x})$ . In a moment a weakly nonlinear analysis will be performed around the Hopf bifurcation point, at which oscillations in  $q$  are small. In this case it is valid to take the Maclaurin expansion of

$$q(x(t - \tau)) \approx q_1(x - \tau\dot{x}) + q_2(x - \tau\dot{x})^2 + q_3(x - \tau\dot{x})^3 + \dots \quad (4.4)$$

where  $q_1 \equiv q'(0)$ ,  $q_2 \equiv q''(0)/2!$  and  $q_3 \equiv q'''(0)/3!$ . For the weakly nonlinear analysis, this expansion is more general than assuming that  $q$  is a specified function of  $\eta$ , as in ([25],[30]-[36]).  $q$  will be expanded only to third order because this is the lowest order that determines the behaviour around the Hopf bifurcation point. Eq.(4.4) is substituted into eq.(4.3), which is re-arranged to give

$$\ddot{x} + (1 + q_1)x + (\zeta - \tau q_1)\dot{x} + q_2(x - \tau\dot{x})^2 + q_3(x - \tau\dot{x})^3 = 0. \quad (4.5)$$

The first two terms are those of a harmonic oscillator with frequency  $(1 + q_1)^{1/2}$ . The third term represents the first order competition between heat release and damping. Around the Hopf bifurcation point they nearly cancel so this term is small. The final two terms are nonlinear and are small around the Hopf bifurcation because the amplitude of  $x$  is small. Eq.(4.5) can therefore be put into the form

$$\ddot{x} + (1 + q_1)x + \varepsilon h(x, \dot{x}) = 0 \quad (4.6)$$

where  $\varepsilon$  is a small parameter. It is then susceptible to a two-timing analysis [24]. A fast time,  $\chi$ , and a slow time,  $T$ , are defined such that  $\chi = t$  and  $T = \varepsilon t$ . These variables,  $T$  and  $\chi$ , are treated as if they are independent. The variable  $x$  is then expressed as a function of  $\chi$ ,  $T$ , and  $\varepsilon$ . The variables  $\dot{x}$  and  $\ddot{x}$  are evaluated using the chain rule

$$x(\chi, T, \varepsilon) = x_0(\chi, T) + \varepsilon x_1(\chi, T) + \mathcal{O}(\varepsilon^2) \quad (4.7)$$

$$\dot{x} = \frac{\partial x_0}{\partial \chi} + \varepsilon \left( \frac{\partial x_1}{\partial \chi} + \frac{\partial x_0}{\partial T} \right) + \mathcal{O}(\varepsilon^2) \quad (4.8)$$

$$\ddot{x} = \frac{\partial^2 x_0}{\partial \chi^2} + \varepsilon \left( \frac{\partial^2 x_1}{\partial \chi^2} + 2 \frac{\partial^2 x_0}{\partial \lambda \partial T} \right) + \mathcal{O}(\varepsilon^2). \quad (4.9)$$

Equations (4.7),(4.8) and (4.9) are substituted into (4.5) and equated at different orders of  $\varepsilon$ . At  $\mathcal{O}(\varepsilon^0)$  and  $\mathcal{O}(\varepsilon^1)$  respectively

$$\frac{\partial^2 x_0}{\partial \chi^2} + (1 + q_1)x_0 = 0 \quad (4.10)$$

$$\begin{aligned} \frac{\partial^2 x_1}{\partial \chi^2} + 2 \frac{\partial^2 x_0}{\partial T \partial \chi} + (1 + q_1)x_1 + (\zeta - \tau q_1) \frac{\partial x_0}{\partial \chi} + q_2 \left( x_0 - \tau \frac{\partial x_0}{\partial \chi} \right)^2 + \\ + q_3 \left( x_0 - \tau \frac{\partial x_0}{\partial \chi} \right)^3 = 0. \end{aligned} \quad (4.11)$$

If variations of  $x_0$  in the slow timescale  $T$  are frozen, eq.(4.10) collapses to an ODE with solution

$$X_0 = r \cos(\omega \chi + \varphi) \quad (4.12)$$

where  $\omega_2 = (1 + q_1)$ ,  $r$  and  $\varphi$  are functions of the slow time  $T$ . Eq.(4.12) is substituted into eq.(4.11), which is re-arranged to give an inhomogeneous ODE for  $x_1$

$$\begin{aligned} \frac{\partial^2 x_1}{\partial \chi^2} + \omega^2 x_1 = \left[ 2\omega r \frac{d\varphi}{dT} - q_3 \frac{3(1 + \omega^2 \tau^2)}{4} r^3 \right] \cos(\omega \chi + \varphi) + \\ + \left[ 2\omega \frac{dr}{dT} + (\zeta - \tau q_1)\omega r - q_3 \frac{3\tau\omega(1 + \tau^2\omega^2)}{4} r^3 \right] \sin(\omega \chi + \varphi) + \Theta \end{aligned} \quad (4.13)$$

where  $\Theta$  includes terms in  $\cos n(\omega \chi + \varphi)$  and  $\sin n(\omega \chi + \varphi)$  where  $n \neq 1$ . To avoid secular terms (terms that grow without bound as  $t \rightarrow \infty$ ), the expressions in square brackets in eq.(4.13) must be zero. This leads to an expression for the evolution of the amplitude  $r$ , and phase  $\varphi$ , on the slow timescale  $T$ , for  $r \neq 0$

$$\frac{dr}{dT} = \frac{(\tau q_1 - \zeta)}{2} r + \frac{3\tau(1 + \tau^2\omega^2)}{8} q_3 r^3 \quad (4.14)$$

$$\frac{d\varphi}{dT} = \frac{3(1 + \tau^2\omega^2)}{8\omega} q_3 r^2. \quad (4.15)$$

The first term on the RHS of eq.(4.14) represents linear driving if  $\tau q_1 > \zeta$  and the second term represents cubic saturation if  $q_3$  is negative or cubic enhancement if  $q_3$  is positive. There is a periodic solution if  $dr/dT = 0$ , which occurs when

$$r = \pm \sqrt{\frac{4(\zeta - \tau q_1)}{3q_3 \tau(1 + \tau^2\omega^2)}}. \quad (4.16)$$

Assuming that  $q_1$  is positive, this gives two types of solution, depending on whether  $q_3$  is positive or negative, as shown in figure (4.3). The same result can be derived with a time-averaging approach. This shows that cubic terms are required in order to predict whether a bifurcation is supercritical or subcritical.

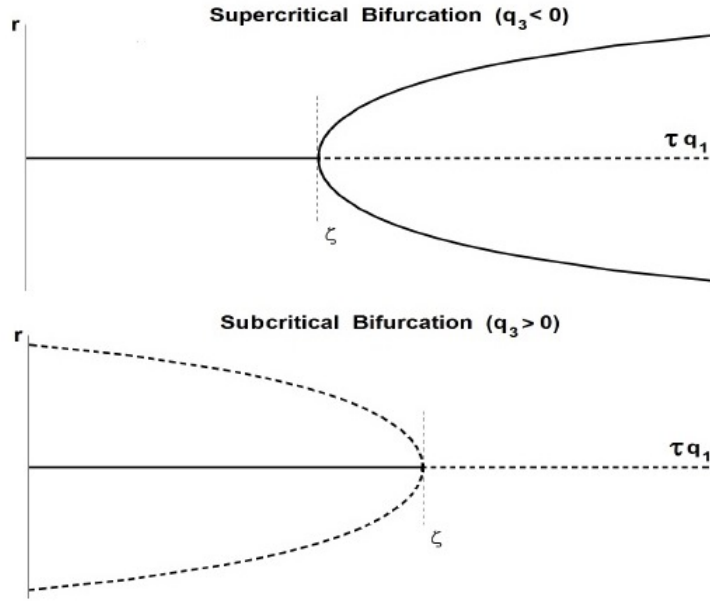


**Figure 4.3:** Bifurcation diagrams around the Hopf point predicted from the weakly nonlinear analysis [26].

## 4.2 NONLINEAR FLAME MODEL

To study the nonlinear behaviour of the combustion instability in Comsol, nonlinear flame model is introduced. In this way bifurcation diagram of the system is reproduced. To obtain nonlinear dependence between  $q'$  and  $u'$ , the procedure proposed by Stow and Dowling [37] is followed. Let consider the linear flame model in eq.(3.1). Nonlinear relation between heat and flow oscillations is obtained introducing nonlinear function  $\Gamma$ , which can be expressed as flow amplitude multiplied by a further nonlinear function  $\Psi$

$$\frac{q'(t)}{\bar{q}} = -k \Gamma \left( \frac{u'(t-\tau)}{\bar{u}} \right) = -k \frac{u'(t-\tau)}{\bar{u}} \Psi \left( \frac{u'(t-\tau)}{\bar{u}} \right). \quad (4.17)$$

The flame model is converted into the frequency domain assuming the flame response to a harmonic input

$$u'(t) = \Re(\hat{u} e^{i\omega t}) = \hat{u} \cos(\omega t). \quad (4.18)$$

For small disturbance, the heat release is also harmonic and is written as

$$q'(t) = \Re(\hat{q} e^{i\omega t}) = \hat{q} \cos(\omega t). \quad (4.19)$$

For finite disturbance,  $q'(t)$  may not be harmonic but is still periodic (with the same period as  $u'(t)$ ) and hence it can be described by a Fourier series

$$q'(t) = \Re \left( \sum_{m=0}^{\infty} \hat{q}^m e^{im\omega t} \right), \quad (4.20)$$

where  $m$  is the order of the harmonics. Let now consider the first harmonic  $\hat{q}^{(1)}$ . The first Fourier coefficient is written as

$$\hat{q}^{(1)} = \frac{\omega}{\pi} \int_0^{\frac{2\pi}{\omega}} q' e^{i\omega t} dt. \quad (4.21)$$

The flame transfer function used in linear model calculation is defined by eq.(3.3). Introducing eqs.(4.18),(4.19) and the nonlinear flame model in eq.(4.17), and considering the property of the Fourier transform that  $F(q'(t)) = F(u'(t-\tau)) = F(u'(t))e^{-i\omega\tau}$  it is show that

$$\begin{aligned} \hat{q}^{(1)} &= \frac{\omega}{\pi} \int_0^{\frac{2\pi}{\omega}} -k \bar{q} e^{-i\omega\tau} r \cos(\omega t) \Psi\left(\frac{u'(t)}{\bar{u}}\right) \left(\cos(\omega t) + i \sin(\omega t)\right) dt \\ &= -k \bar{q} r e^{-i\omega\tau} \frac{\omega}{\pi} \int_0^{\frac{2\pi}{\omega}} \Psi\left(\frac{u'(t)}{\bar{u}}\right) \cos^2(\omega t) dt \end{aligned} \quad (4.22)$$

where the imaginary term disappears because the integral from 0 to  $2\pi$  of the product of cosine and sine is null. Solving the integral in eq.(4.22) and considering eq.(3.3), nonlinear flame transfer function is obtained

$$FTF_{NL}(\omega, r) = FTF_L(\omega) NFTF \quad (4.23)$$

where

$$NFTF = \frac{\omega}{\pi} \int_0^{\frac{2\pi}{\omega}} \Psi\left(\frac{u'(t)}{\bar{u}}\right) \cos^2(\omega t) dt \quad (4.24)$$

is a function of frequency and amplitude  $r = |\hat{u}/\bar{u}|$ .

### 4.3 PROCEDURE TO TRACK BIFURCATION DIAGRAMS

There are two procedures to obtain the bifurcation diagrams using the FEM approach. The first is similar to the theoretical one described by Jahnke and Culick [22], while the second one is a consequence of numerical code property. The general technique is based on fixing all parameters of the system but one and tracing the steady states of the system as a function of this parameter. In this work, at first, several tests are performed using the interaction index  $k$  as control parameter, while in second time, two experimental data are reproduced varying combustion chamber length. In both cases the not fixed parameter is the oscillation amplitude  $r$ . It implies that, each time a value of the amplitude  $r$  is assumed to detect the solutions of the eigenvalue problem, a linear flame model is solved. In fact the amplitude  $r$  is defined as  $|\hat{u}/\bar{u}|$ , hence the *NFTF* function degenerates to a constant value and the transfer matrix becomes linear. As a consequence, although the flame model is nonlinear, the eigenvalue problem is solved for a linear flame model detecting each point of the bifurcation diagram. At the beginning the Hopf bifurcation point is evaluated. The amplitude  $r$  is set equal to zero and the control parameter used is varied until the passage from a stable to an unstable condition is observed, which

means when the imaginary part of the complex eigenfrequencies becomes negative. The Newton's method is adopted to detect the point corresponding to zero growth rate, using the last value of  $k$  with positive imaginary part and the first value of  $k$  with negative imaginary part. Once the Hopf point is identified, two different approaches can be followed to reproduce bifurcation diagrams. Theoretical method of Culick [22] claims that value of control parameter is changed in the range of interest, and for each value of this, zero growth rate condition is found varying the amplitude  $r$ . This method is valid for any control parameters assumed, but in case the control parameter is the interaction index  $k$ , another easier approach can be used. In fact, nonlinear flame transfer function is defined as product of linear FTF, interaction index  $k$  and  $NFTF$  which is function of the amplitude. Then, setting the value of amplitude  $r = r_0$ , one value of  $NFTF$  is obtained and linear FTF is multiplied by constant  $C = k * NFTF(r_0)$ . Initially, setting  $r_0 = 0$ , a fixed value of  $NFTF$  is considered and proportional relation between  $C$  and  $k$  is founded. For this condition, varying index  $k$  (and then value of  $C$ ) until unstable condition, Hopf point is evaluated. When both  $k$  and  $r$  vary, the zero growth rate condition is obtained for only one value of  $C$ . This value of  $C$  is the same used for detecting the Hopf point. Then, for each value of  $r$ , the zero growth rate condition is expected for  $k = \frac{C}{NFTF(r)}$ . This approach is faster than theoretical one because when Hopf point is evaluated the entire bifurcation diagram can be reproduced. However this method can be used only when the control parameter is  $k$ , while in other cases Culick's approach is required. Anyhow, connecting the points identified through the process illustrated, the bifurcation diagram is obtained.



---

# 5 NUMERICAL TESTS

---

First, to study nonlinear behaviour of combustion systems, heat release models from the literature are compared with the corresponding data obtained by Comsol. Several nonlinear flame models are tested obtaining bifurcation diagrams on simple geometry as a Rijke tube or simplified annular combustion chamber. For these geometries, using interaction index  $k$  as a control parameter, several bifurcation diagrams are obtained to evaluate the influence of *NFTF*'s coefficients and boundary conditions. Then, to confirm Comsol approach, two experimental data are reproduced. In these cases bifurcation diagrams are obtained using combustion chamber length as a control parameter. The first experimental test considered is reproduced by Noiray [41]. It considers simple tube geometry with premixed combustion and variable chamber length. Using analytical heat release model proposed by Heckl [42][43], bifurcation diagrams are reproduced. The second experimental test considered is carried out by Palies [44][45] in horizontal tube with swirl premixed combustion and variable length of the zones before and after the flame. Finally, using the flame model applied on the configuration proposed by Palies, investigation of thermoacoustic instability is carried out on geometry of Ansaldo Energia machine AE94.3A.

## 5.1 RIJKE TUBE

At first, simple configuration of Rijke tube is analyzed. The two sectors separated by the flame zone represent the plenum (before the flame) and the combustion chamber (after the flame). Details of the geometry are given in table 5.1 while the operating conditions are reported in table 5.2.

Table 5.1: Rijke tube dimensions

Description	Value
Plenum length	0.75 m
Flame zone length	0.0225 m
Combustion chamber length	2.2275 m
Sectional area	0.07854 m

There is no mean flow. At the beginning open-end inlet and outlet boundary conditions ( $p' = 0$ ) are considered and time delay is set constant  $\tau = 0.02$  s. This assumption permits to isolate only the heat release effect without considering the time delay influence. Fig.5.1 shows the computational mesh, which consists of 6070

Table 5.2: Rijke tube operating conditions

Description	Value
Pressure	100000 Pa
Plenum temperature	300 K
Flame zone and combustion chamber temperature	700 K
Specific heat ratio	1.33

elements, and the location of the heat release which is highlighted. For this configuration several nonlinear heat release models are set to track bifurcation diagrams and to evaluate the influence of the parameters of the system on stability conditions.

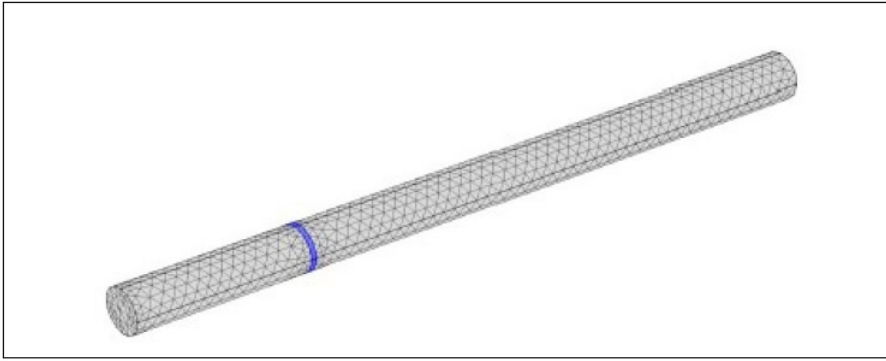


Figure 5.1: Computational mesh of the Rijke tube (the flame location is highlighted in blue).

### 5.1.1 Boundary condition influence

The first flame model tested is a quadratic polynomial, written with reference to the van der Pol oscillator

$$\ddot{x} + (\mu_2 x^2 - \mu_0)\dot{x} + x = 0. \quad (5.1)$$

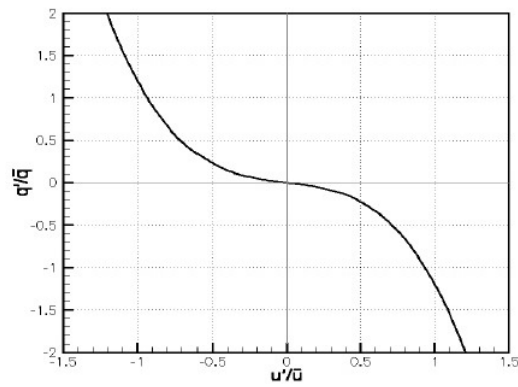
The nonlinear flame model becomes eq.(5.2) and its behaviour is reported in Fig.5.2(a).

$$\frac{q'}{\bar{q}} = -k \left[ \mu_2 \left( \frac{u'(t-\tau)}{\bar{u}} \right)^2 + \mu_0 \right] \frac{u'(t-\tau)}{\bar{u}} \quad (5.2)$$

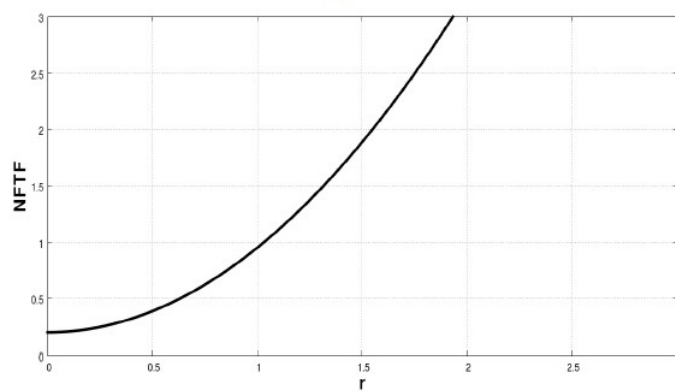
The Nonlinear Flame Transfer Function is obtained following the passages described in the previous section 4.2,

$$NFTF = \frac{3}{4} \mu_2 r^2 + \mu_0. \quad (5.3)$$

Several couples of values for  $\mu_2$  and  $\mu_0$  was analyzed by Cinquepalmi [38]. In this work values is set as  $\mu_2 = 1$  and  $\mu_0 = 0.2$  (Fig.5.2(b)).



(a)



(b)

Figure 5.2: (a) Flame model in eq.(5.2) with  $\mu_2 = 1$  and  $\mu_0 = 0.2$ , (b) *NTF* in eq.(5.3).

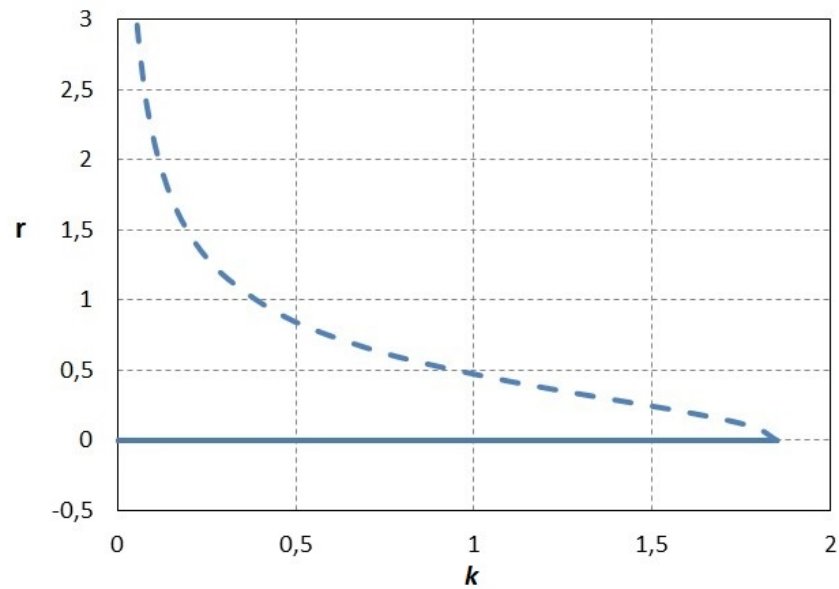


Figure 5.3: Bifurcation diagram of Rijke tube for the polynomial nonlinear flame model in eq.(5.2) with  $\mu_2 = 1$  and  $\mu_0 = 0.2$ .

Using interaction index  $k$  as a control parameter, and flow oscillation's amplitude  $r$  as a not fixed parameter, bifurcation diagram is obtained (Fig.5.3). The first and third derivatives in zero of eq.(5.3) are both negative, which means that, from nonlinear weakly analysis, subcritical bifurcation is expected. Results show that beyond the Hopf point the oscillations grow without limit because both  $\mu_2$  and  $\mu_0$  are positive. Before the Hopf point, periodic solution is unstable for the same reason (see Fig.(4.3)). As amplitude  $r$  increases, unstable conditions occur at lower values of  $k$ . Dashed line represents the zero growth rate condition, under this line the amplitude is damped and system is stable while, over the line, the amplitude grows without limit.

For this *NFTF* influence of the end boundary condition is evaluated. In particular many values of reflection coefficient  $R_L$  is set to vary sound impedance  $Z$  (eq.(5.4)) at the exit of Rijke tube.

$$Z = \frac{p}{u} = \rho c \frac{(1 + R_L)}{(1 - R_L)} \quad (5.4)$$

For  $R_L = -1$  wave is totally reflected and open end case returns, while to increase reflection coefficient dissipative and transmission effects are modelled.

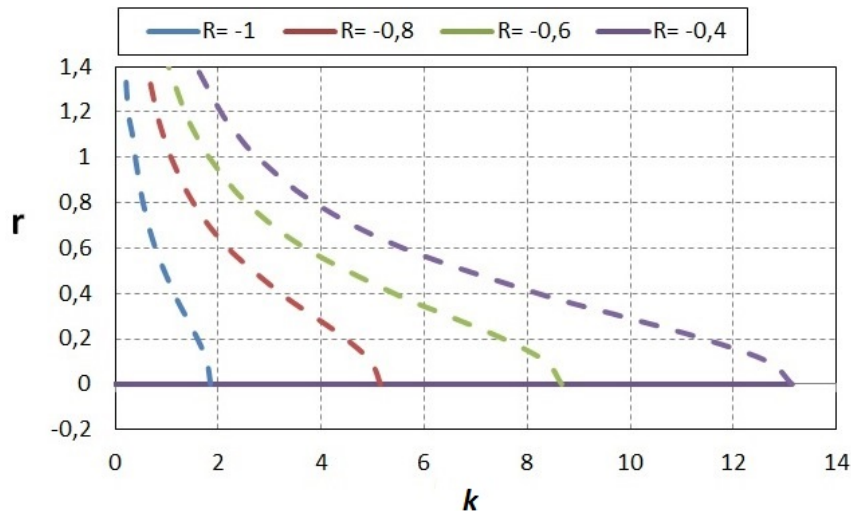


Figure 5.4: Influence of reflection coefficient on limit cycle of eq.(5.2).

Results reported in Fig.5.4 show that moving from open end to closed boundary condition, Hopf point moves at higher values of  $k$ , and then, stable zone increases. Also, at the same heat release, as reflection coefficient drops, the oscillation amplitude increases. Finally, as  $k$  goes to zero asymptotic limit cycles is expected and unstable condition is equal for any values of  $R_L$ . As reflection coefficient varies, oscillation's frequency of the system changes. In particular, from  $R_L = -1$  to  $R_L = -0.4$  frequency varies in a range from 74.6 Hz to 85.7 Hz with a monotone increasing behaviour.

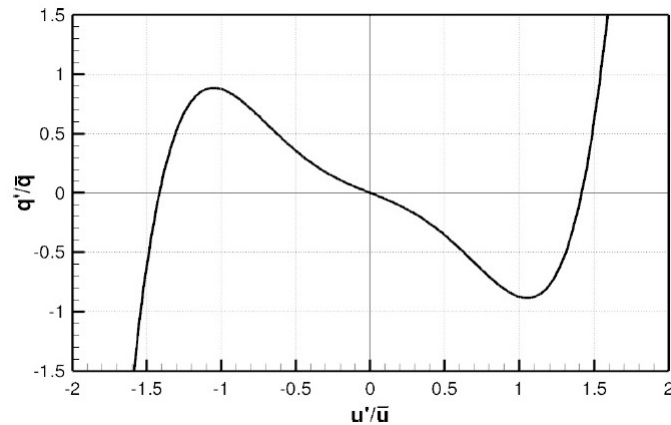
## 5.1.2 Time delay influence

The second flame model considered is a fourth order polynomial, written with reference to the van der Pol oscillator augmented with a fourth order term. So the nonlinear flame model becomes

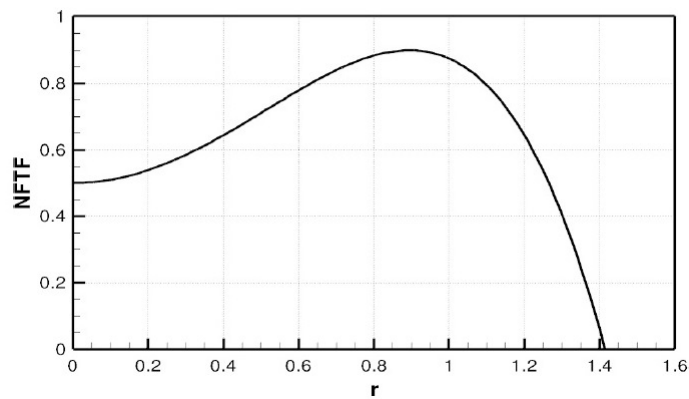
$$\frac{q'}{q} = -k \left[ \mu_4 \left( \frac{u'(t-\tau)}{\bar{u}} \right)^4 + \mu_2 \left( \frac{u'(t-\tau)}{\bar{u}} \right)^2 + \mu_0 \right] \frac{u'(t-\tau)}{\bar{u}}. \quad (5.5)$$

Following the same steps previously described, the *NFTF* is obtained:

$$NFTF = \frac{5}{8} \mu_4 r^4 + \frac{3}{4} \mu_2 r^2 + \mu_0. \quad (5.6)$$



(a)



(b)

**Figure 5.5:** (a) Flame model in eq.(5.5), (b) *NFTF* in eq.(5.6) with  $\mu_4 = -1$ ,  $\mu_2 = 1$  and  $\mu_0 = 0.2$ .

The case with  $\mu_4 = -1$ ,  $\mu_2 = 1$  and  $\mu_0 = 0.2$  is studied. The *NFTF* is positive only for small values of the amplitude and then it is negative. Even in this case the *NFTF* function is considered only when it is positive and for positive values of the amplitude  $r$  to ensure the physical meaning of the flame model Fig.5.5 (b). Applying this flame model, bifurcation diagram is obtained (Fig.5.6). The results show a subcritical Hopf bifurcation to an unstable periodic solution at small amplitudes,

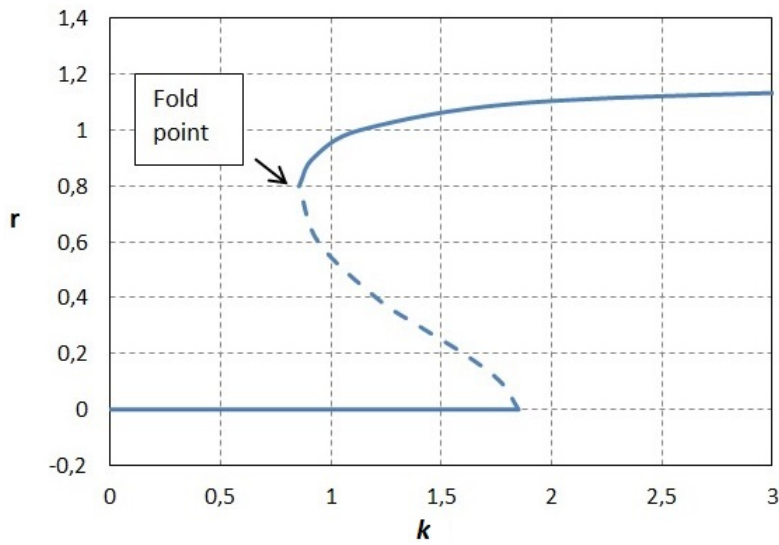


Figure 5.6: Bifurcation diagram of Rijke tube for the polynomial nonlinear flame model in eq.(5.5) with  $\mu_4 = -1$   $\mu_2 = 1$  and  $\mu_0 = 0.2$ .

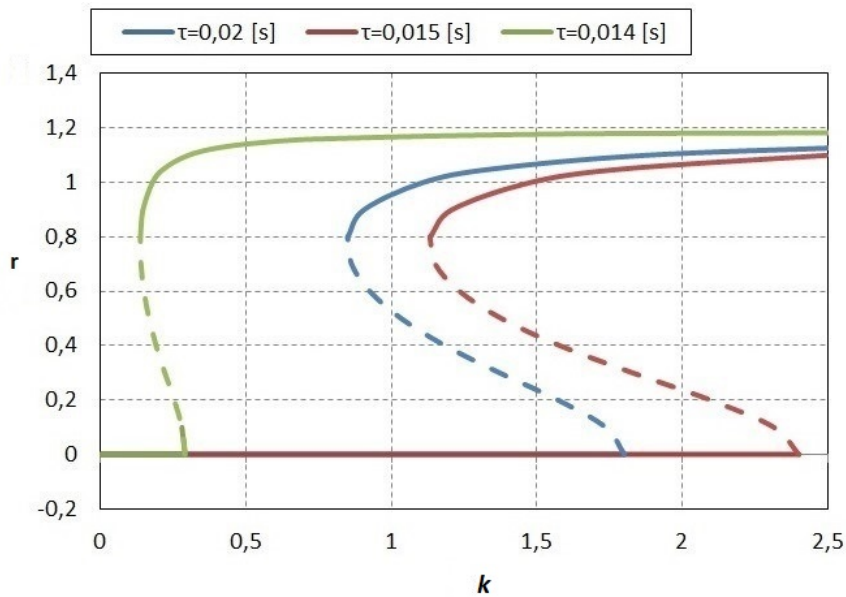


Figure 5.7: Influence of time delay on bifurcation diagram.

followed by a fold bifurcation to stable periodic solution at large amplitudes. The value of  $r$  which changes limit cycle's behaviour is called fold point. For this heat release model influence of time delay is studied (Fig.5.7). As time delay varies, qualitative behaviour of bifurcation doesn't change but stability conditions vary. In particular, for  $\tau=5$  ms the system is always stable; for  $\tau=10$  ms the system is always unstable;  $\tau=14$  ms the frequency diminishes from 72 to 71.4 Hz until the Hopf point and then remains constant along the bifurcation curve; for  $\tau=15$  ms the frequency falls from 72 to 66.7 Hz until the Hopf point, staying fixed ever after along the bifurcation curve; for  $\tau=20$  ms the frequency rises from 72 to 75 Hz until the Hopf point and next does not change. Furthermore, with  $\tau=15$  ms the system has the

largest stability field (Hopf point at  $k=2.37$ , fold point at  $k=1.12$  and limit cycle amplitude  $r=1.1$ ), while with  $\tau=14$  ms the system has the smallest stability field (Hopf point at  $k=0.27$ , fold point at  $k=0.13$  and limit cycle amplitude  $r=1.18$ ); with  $\tau=20$  ms the situation is intermediate (Hopf point at  $k=1.83$ , fold point at  $k=0.87$  and limit cycle amplitude  $r=1.12$ ). Fold points occur always at the same amplitude. Previous results show that time delay hasn't monotone influence. In fact, as time delay changes, phase displacement between heat release and velocity's fluctuation varies, and it can be improve or aggravate stability conditions.

### 5.1.3 Damping effect

The third flame model tested differs than previous because it links heat's oscillation to pressure's oscillations  $r=|p'/\bar{p}|$ , according to experimental results obtained by Noiray (Fig.5.8)[39]. Experimental results are approximated with different re-

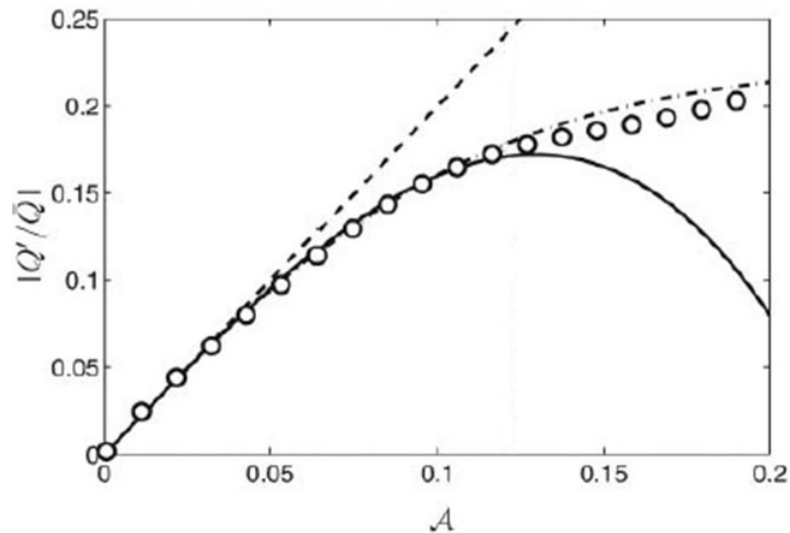


**Figure 5.8:** Saturation of the normalized heat release rate fluctuations  $|Q'/\bar{Q}|$  as a function of the amplitude  $r$  [39]. (o) Experimental measurements; (---) $|Q'/\bar{Q}| = \mu_0 r$ ; (—) $|Q'/\bar{Q}| = \mu_0 r - \mu_1 r^3$ ; (-·-) $|Q'/\bar{Q}| = \gamma \tanh(\delta r)$ .

lations. As shown in Fig.5.8, linear approximation is good for lower values of amplitude, but as pressure's oscillation increases nonlinear effects occur. An excellent agreement is found for hyperbolic tangent function while cubic polynomial relation approximates experimental data in a large range of interest. Considering the cubic polynomial suggested by Noiray, bifurcation diagram of the system is obtained. Then, the flame model is set as:

$$\frac{q'}{\bar{q}} = \mu_0 \frac{p'(t-\tau)}{\bar{p}} - \mu_1 \frac{p'(t-\tau)^3}{\bar{p}} \quad (5.7)$$

which corresponds to

$$NFTF = \beta_0 - \beta_1 r^2. \quad (5.8)$$

Keeping  $\tau = 20$  [ms] and setting  $\beta_1 = 0.5$ ,  $\beta_0 = 1$  supercritical bifurcation is obtained (Fig.5.9). For lower value of  $k$  stable solution is expected, while beyond Hopf

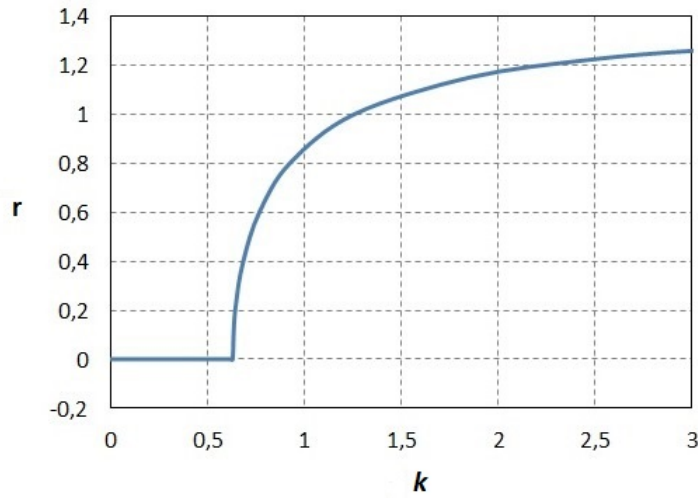


Figure 5.9: Bifurcation diagram for Rijke tube for nonlinear flame model in eq.(5.8) with  $\beta_0 = 1$  and  $\beta_1 = 0.5$ .

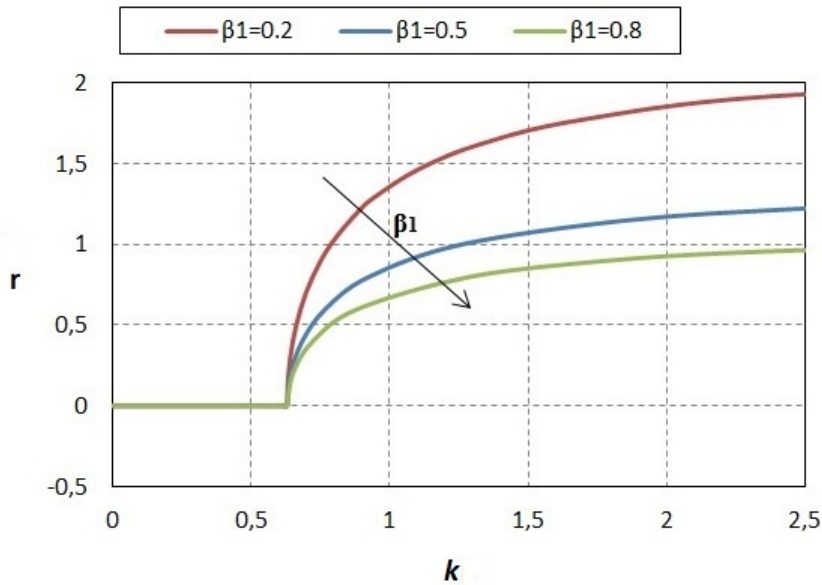


Figure 5.10: Influence of  $\beta_1$  coefficient on stability condition.

point ( $k= 0.63$ ) system moves towards higher oscillation amplitude. To evaluate  $\beta_1$  influence, parametric study is executed. Results obtained are reported in Fig.5.10 and they show that as  $\beta_1$  varies, the Hopf point doesn't change. This occurs because the Hopf point is evaluated at amplitude  $r= 0$  and then, only parameter  $\beta_0$  has influence on stability conditions. However, from  $r \neq 0$ , as  $\beta_1$  increases, lower amplitude reached by system is expected.

If negative value of  $\beta_1$  is set, according to weakly nonlinear analysis, subcritical bifurcation occurs (Fig.5.11).

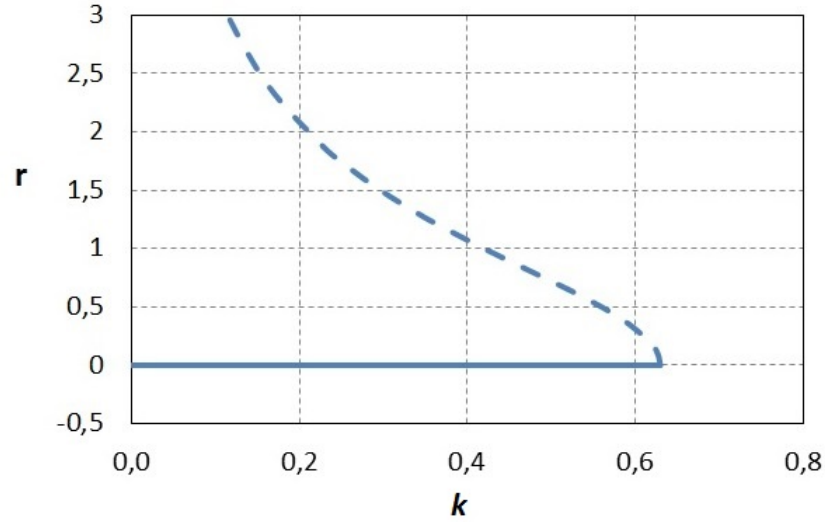


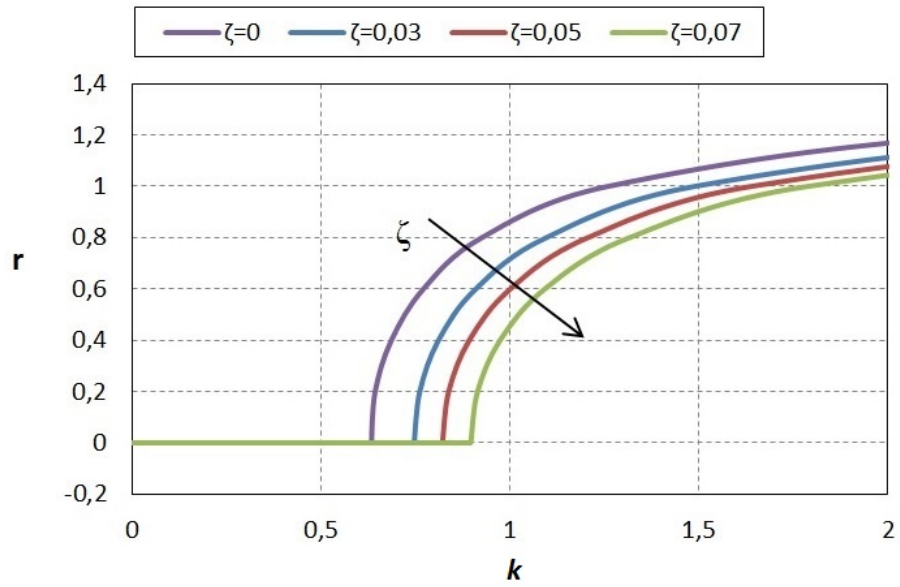
Figure 5.11: Influence of sign of  $\beta_1$  coefficient on stability condition.

For this flame model, the influence of damping on combustion instability is evaluated. Presence of damping leads to a new positive term in left-hand member of Helmholtz equation [40],

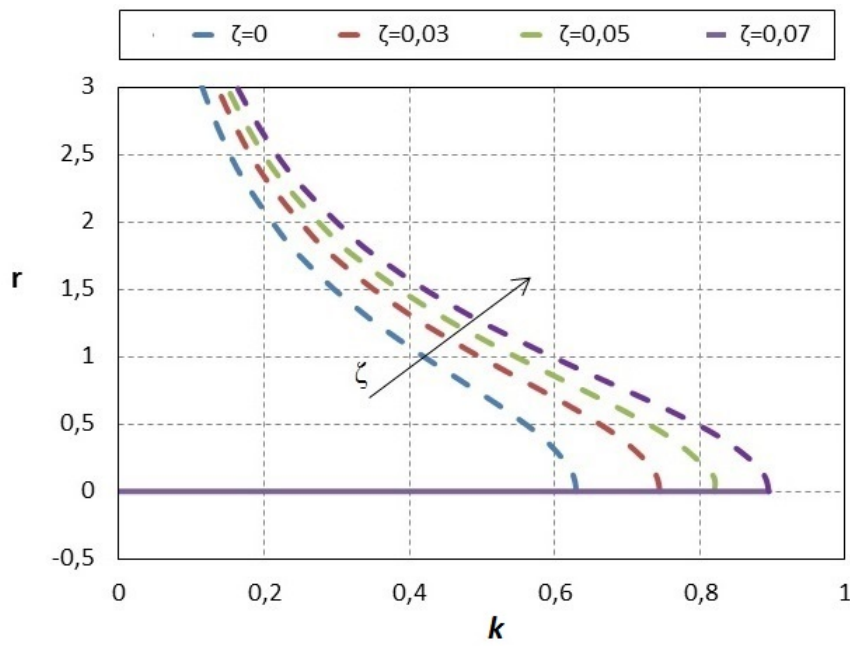
$$\frac{1}{\bar{c}^2} \frac{\partial^2 p'}{\partial t^2} + \frac{\zeta}{c R_H} \frac{\partial p'}{\partial t} - \bar{\rho} \nabla \cdot \left( \frac{1}{\bar{\rho}} \nabla p' \right) = \frac{\gamma - 1}{\bar{c}^2} \frac{\partial q'}{\partial t}, \quad (5.9)$$

where  $\zeta$  is damping coefficient. To reproduce damping effect in Comsol negative source term must be added in eq.(3.5). Damping can be attributed to many factors as flow viscosity, or damping walls. Several tests are obtained varying coefficient in a range between  $\zeta = 0$  and  $\zeta = 0.7$  to evaluate damping influence. This approach is applied to *NFTF* of eq.(5.8) for positive and negative value of  $\beta_1$  in order to consider damping effect on supercritical and subcritical bifurcation (Fig.5.12). Results show that as damping coefficient increases, Hopf point moves to higher values of  $k$ , then stable zone is augmented. However damping coefficient have influence on lower amplitude, while as  $r$  increases the same behaviour of bifurcation is expected. This happens for both type of bifurcation, and it can be explained as result of lower interaction between heat release oscillation and damped acoustic waves.

NUMERICAL TESTS



(a)



(b)

Figure 5.12: Influence of damping coefficient on supercritical (a), and subcritical (b) bifurcation .

## 5.2 SIMPLIFIED ANNULAR COMBUSTION CHAMBER

The second nonlinear test is conducted on a simplified annular combustion chamber geometry used in the previous section for linear analysis 3.2.2. Operating and boundary conditions are the same, time delay is set constant and equal to 2 [ms] and nonlinear flame model is considered. Fig.5.13 shows the computational mesh, which consists of 25776 elements, and the location of the heat release of single burner is highlighted. For this geometry several nonlinear tests are carried out and bifurcation diagrams of the first azimuthal chamber mode (Fig.3.6(c)) are obtained. This mode is the most interesting because is the most dangerous for practical operations, and for this simplified geometry it shows up at frequency equal to 750 Hz.

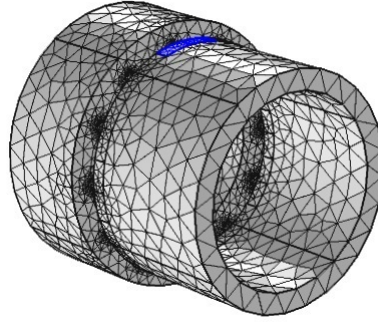


Figure 5.13: Computational grid of the simplified annular combustion chamber.

### 5.2.1 Polynomial flame model

To confirm Comsol approach, van der Pol oscillator model augmented with a fourth order term is used for nonlinear flame model in simplified annular combustion chamber geometry. This flame model is already studied in previous section for Rijke tube with *NFTF* explicit in eq (5.6). Setting  $\mu_4 = -1$ ,  $\mu_2 = 1$  and  $\mu_0 = 0.5$  the first azimuthal chamber mode is analyzed. Bifurcation diagram obtained is reported in Fig.5.14. Bifurcation diagram is qualitatively similar to the one obtained for Rijke tube, with fold point at amplitude equal to 0.8 in both cases. This confirms that bifurcation diagram obtained with interaction index  $k$  as control parameter, depends on the nonlinear flame model applied, independently to the geometry. To evaluate the influence of polynomial coefficients, parametric analysis is performed.

$$NFTF = -\beta_2 r^4 + \beta_1 r^2 + \beta_0 \quad (5.10)$$

Initially influence of  $\beta_0$  is studied keeping  $\beta_2 = 5/8$  and  $\beta_1 = 3/4$  (Fig.5.15 (a)). The results show that qualitatively limit cycle remains the same but the Hopf point varies. This occurs because Hopf point is found at  $r = 0$ . At this condition, *NFTF* is equal to  $\beta_0$  and flame model becomes linear with new interaction index  $C = k \cdot \beta_0$ . Hence, since unstable condition occurs at the same value of  $C$ , as  $\beta_0$  increases, the Hopf point is expected at lower values of  $k$ . In second time influence of  $\beta_1$  and

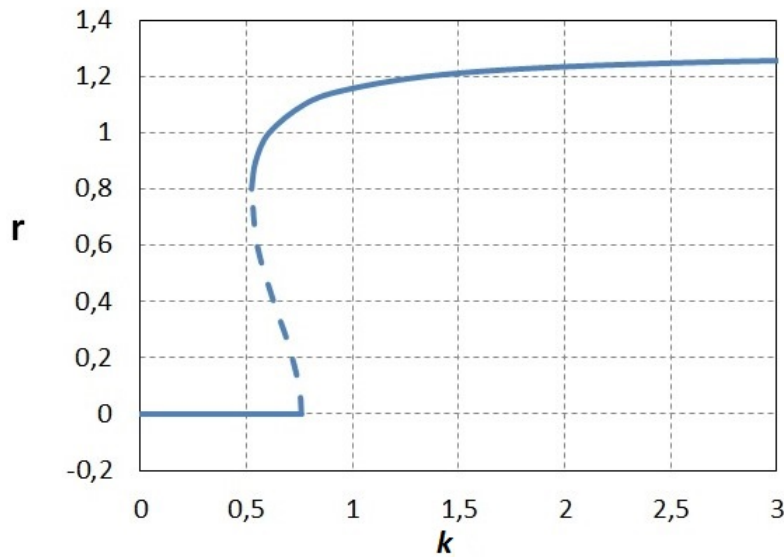


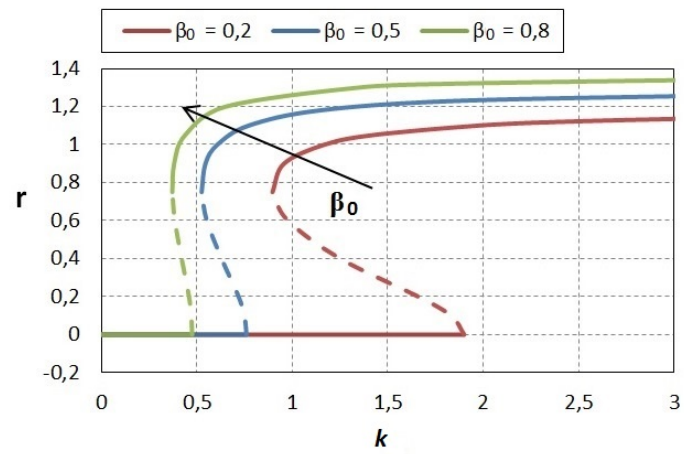
Figure 5.14: Bifurcation diagram of simplified annular combustion chamber for flame model in eq.(5.5) with  $\mu_4 = -1$ ,  $\mu_2 = 1$  and  $\mu_0 = 0.5$ .

$\beta_2$  coefficients are studied (Fig.5.15 (b)(c)). The influence of  $\beta_1$  is evaluated fixing  $\beta_2$  and  $\beta_0$  constant and equal to  $5/8$  and  $0.5$ . At these conditions three bifurcation diagrams are obtained for different test values of  $\beta_1$ . In particular,  $\beta_1$  is set equal to  $0.5$ ,  $0.75$ ,  $1$ . In second time, effects of fourth order term of *NFTF* are studied, setting  $\beta_2$  equal to  $2/5$ ,  $5/8$ ,  $4/5$  and fixing  $\beta_0 = 0.5$  and  $\beta_1 = 3/4$ . As before, Hopf point is the same because  $\beta_0$  coefficient is constant, but oscillation's amplitude reached by the system at the equilibrium varies. In particular these coefficients have opposite effect. As fourth order coefficient increases, oscillation amplitude decreases, while as second order coefficient grows, higher value of amplitude is expected.

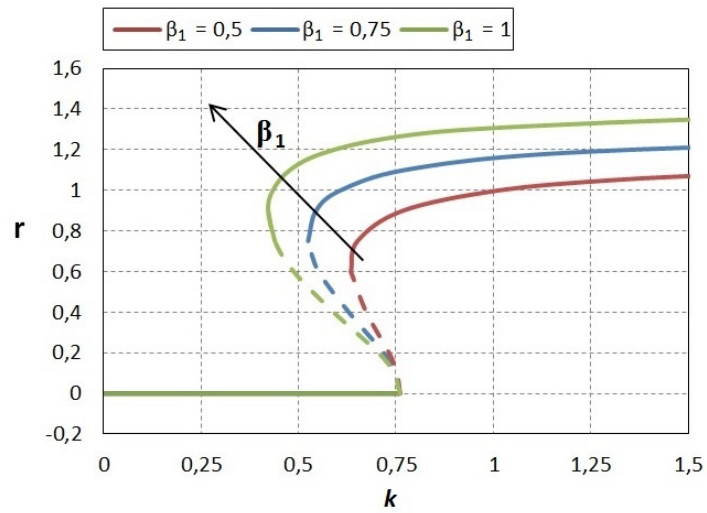
### 5.2.2 Influence of geometry

To evaluate influence of chamber geometry on combustion instability, several bifurcation diagrams are obtained varying length of the zone before (plenum) and after (chamber) the flame. In particular, length of plenum is varied between  $0.1$  to  $0.3$  [m]. Tests with variable chamber lengths are obtained for  $L_c$  equal to  $0.15$  [m],  $0.2$  [m],  $0.25$  [m],  $0.4$  [m]. In particular, for the first two chamber length values, system is always unstable, while for other values bifurcation diagrams are obtained (Fig.5.16). Results show that as length of plenum or chamber increase, stable zone augments. In fact heat release remains constant but volume of the combustion system varies. In particular, as length of plenum or chamber increases, volume of the system grows, and heat per unit volume is reduced promoting stability condition. This explains also the instability conditions observed for  $L_c=0.15$  [m] and  $L_c=0.2$  [m]. In the bifurcation diagram considered, Hopf point moves towards higher value of  $k$ , while the last amplitude reached by the system is independent from geometry.

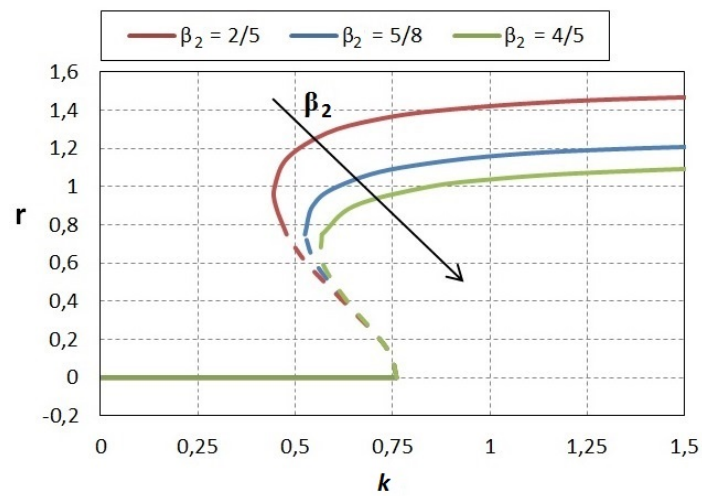
## 5.2 SIMPLIFIED ANNULAR COMBUSTION CHAMBER



(a)

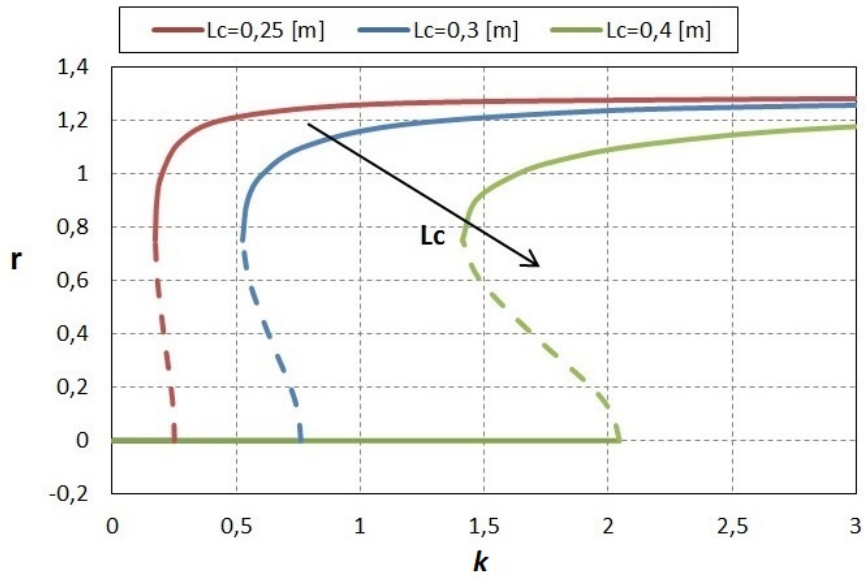


(b)

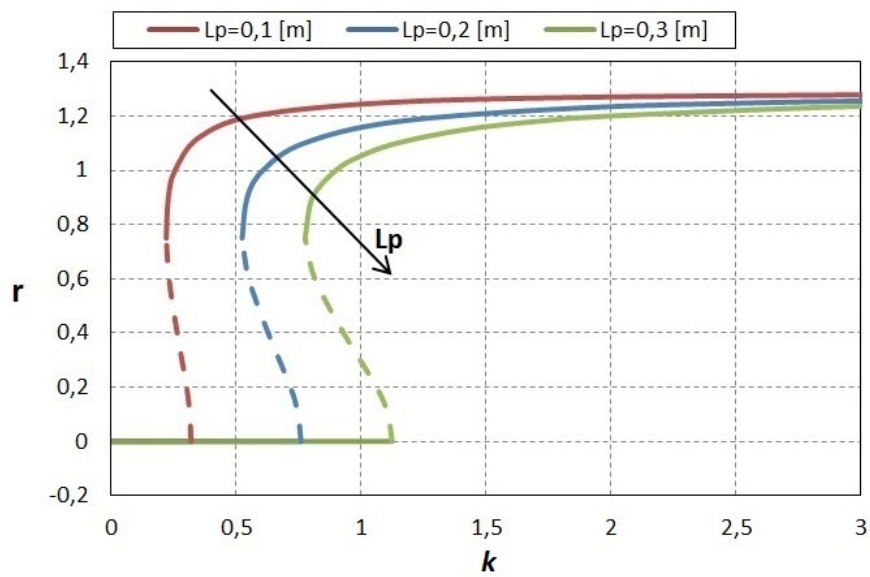


(c)

Figure 5.15: Influence of polynomial coefficients in eq.(5.10):(a)  $\beta_0$  coefficient, (b)  $\beta_1$  coefficient, (c)  $\beta_2$  coefficient.



(a)



(b)

Figure 5.16: Influence of geometry on bifurcation diagram:(a) variable chamber length, (b) variable plenum length.

## 5.2.3 Asymmetric conditions

To evaluate stability of combustion system asymmetric conditions are tested. In particular, bifurcation diagrams are obtained for different asymmetric conditions of the burners. Fig.5.17 shows the configurations considered.

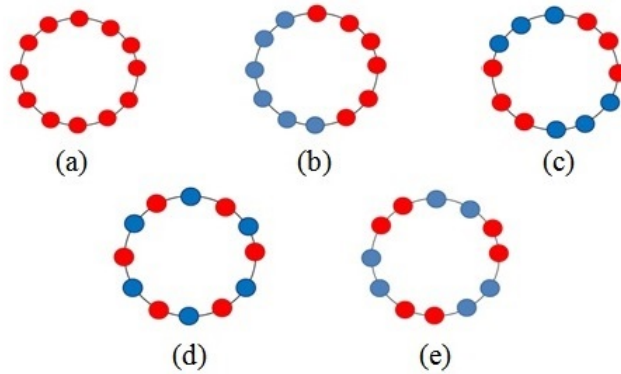
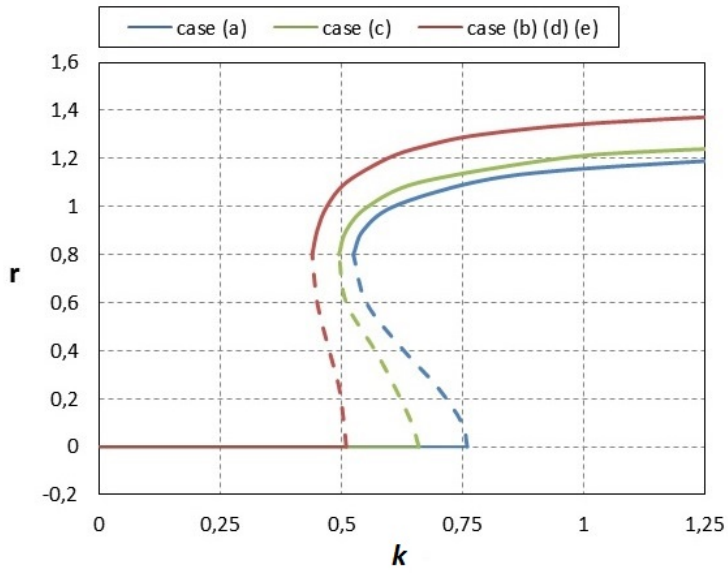


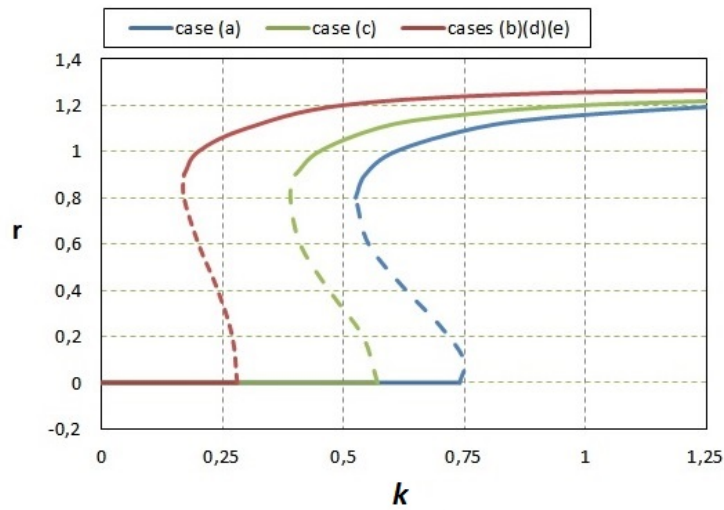
**Figure 5.17:** Asymmetric configurations tested:(a) all burners have the same conditions; (b) one symmetry plane is used to divide six different burners from the others; (c) two symmetry planes are considered; (d) every burner is between two with different conditions; (e) two alternate different burners are applied.

At first, asymmetric distribution of time delay is tested. One set of burners (red in figure) is set with  $\tau_1$  while other burners (blue in figure) work with time delay  $\tau_2$ . As in the previous analysis,  $\tau_1$  is equal to 2 [ms] while several tests are carried out with different values of  $\tau_2$ . In particular for  $\tau_2 = 0.5$  [ms],  $\tau_2 = 1$  [ms] and  $\tau_2 = 3$  [ms] the system is always stable while for  $\tau_2 = 3.5$  [ms] and  $\tau_2 = 4$  [ms] the system is always unstable. For  $\tau_2 = 3.4$  [ms], varying intensity of heat release, system evolves from stable to unstable condition and bifurcation diagram can be produced (Fig.5.18(a)). Results show that if asymmetric conditions are applied stable zone is reduced. Additionally, the same bifurcation diagram is obtained for asymmetric case (b)-(d)-(e) while stable zone of case (c) is more extended than other asymmetric case but lower of main setting (a). However oscillation amplitude reached by the system is the same for all cases tested.

The second asymmetric analysis is executed applying two different flame models with the asymmetric burner configuration of Fig.5.17. In particular six burners are set with linear flame model dependent on velocity flow, while the others use non-linear flame model of (5.6). Results are reported in Fig.5.18(b). The same behaviour obtained for nonuniform azimuthal time delay is obtained. In particular, asymmetric distribution of linear and nonlinear models reduces stable zone, then Hopf point moves towards lower value of  $k$ . This effect is lower for burner configuration (b) while the others asymmetric cases lead to the same limit cycle.



(a)



(b)

Figure 5.18: Influence of asymmetric conditions of the burners on bifurcation diagram:(a) asymmetric time delay influence, (b) asymmetric flame model influence.

### 5.3 EXPERIMENTAL TEST OF NOIRAY

To confirm Comsol approach for combustion instability prediction, experimental data obtained by Noiray are reproduced. Experimental setup consists in a tube terminated at the upstream end by a piston with variable position and at the downstream end by a perforated plate, as shown schematically in Fig.5.19 [41]. A pre-

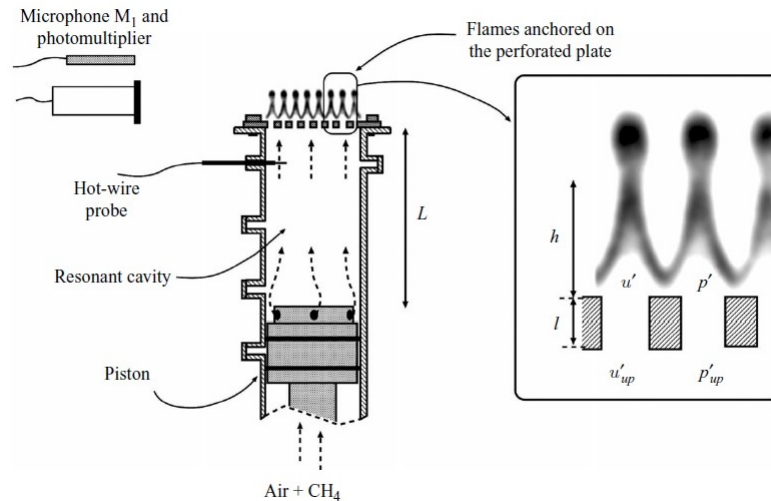


**Figure 5.19:** Experimental setup of Noiray: the burner is sketched on the left. A close-up view of the flames anchored on the perforated plate is displayed on the right [41].

mixed gas (methane and air) enters the tube through small holes in the head of the rigid piston. This mixture passes through the perforated plate, which acts as a flame holder, and is burnt in the matrix flame just outside the tube. Essentially, the tube is a quarter-wave resonator (one rigid end and one nearly open end) with variable length  $L$ . The head of the piston is flat providing a quasi-perfect acoustic reflection boundary at the bottom of the burner. It is easy to modify the resonant cavity size  $L$  (and thus the acoustic properties of the burner) by changing the piston position. The length  $L$  used in this investigation, and used as bifurcation parameter, takes values from 10 to 75 cm. The resonant duct radius  $R_d$  is equal to 3.5 cm. It is small enough to assume that wave propagation is longitudinal in the upstream duct for frequencies lower than 1500 Hz. Details of perforated plate can be found in [41]. From this setup Noiray measured the gain and phase of the FTF of his matrix burner by exciting it acoustically. In particular it is appropriate to use the designation "Flame Describing Function" (FDF) instead of Flame Transfer Function (FTF). This distinction is already apparent in some previous theoretical studies, and it considers FTF dependent on input velocity amplitude. So, experimental FDF is obtained by Noiray using five different velocity amplitudes. Results are reported in Fig.5.20. The FDF depends strongly on the velocity amplitude. As the amplitude increases, the slope of the phase curves grows. In the gain curves, the frequency interval, which spans the first minimum (at zero frequency) to the next minimum becomes smaller and smaller. In literature there are some interesting studies concerning the dependence of the flame transfer function on the input level. Many

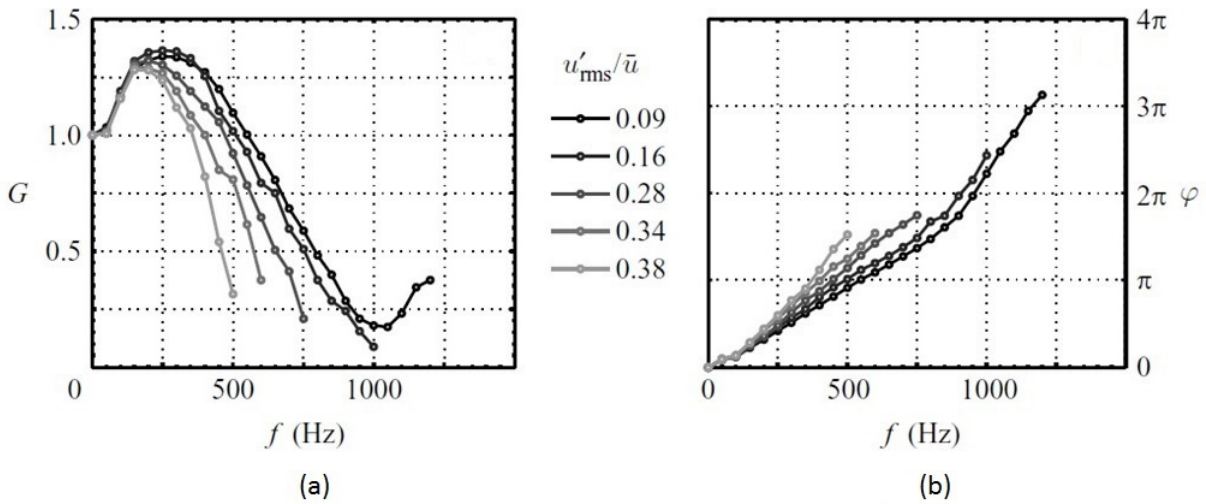


Figure 5.20: FDF measured by Noiray: (a) the gain, (b) the phase [41].

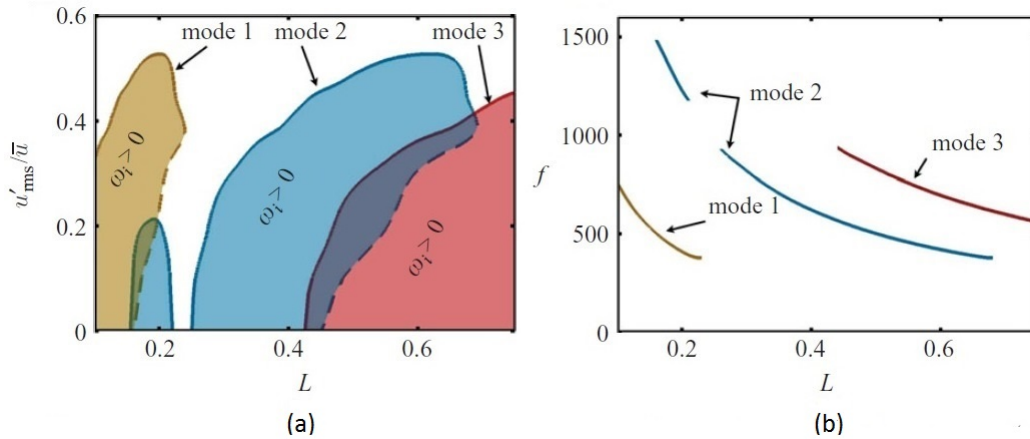


Figure 5.21: Results obtained by Noiray on the first three modes of the system: (a) bifurcation diagram, (b) oscillation frequency expected at the limit cycle [41].

of these studies indicate that as the input level increases the gain drops, in agreement with what is observed in Fig.5.20(a). However, results concerning the phase evolution as a function of the amplitude level are less straightforward than those found in the Noiray's investigation. From experimental data, using NDR analytical method [41], stability condition of the system was evaluated by Noiray. In particular, position of the piston was varied, and for each condition, growth rate value was determined. Then, bifurcation diagram was obtained considering the zero growth rate condition (Fig.5.21). Fig.5.21(a) shows limit cycles of three modes which are represented by different colors. Boundaries of bifurcations correspond to  $\omega_i = 0$  while color zone represent positive growth rate condition then unstable zone. For the first two modes solid and dashed boundary lines are plotted. In two cases the boundary features a turning point with respect to  $L$ . This critical point separates the two branches composing the boundary. The upper branch plotted as a solid line is the locus of stable limit cycles as can be seen by noting that if the system is brought to a point below this branch, the growth rate becomes positive and the

amplitude increases bringing the system back to the initial equilibrium. If on the other hand the system is brought to a point located above that branch, the growth rate becomes negative and the amplitude is reduced until the initial equilibrium is reached. A similar reasoning can be used to show that the lower branches represented by dashed lines pertain to unstable limit cycles. For a fixed cavity size  $L_1 = 0.21$  [m] second mode features a positive growth rate for small amplitude values, indicating that this mode is linearly unstable. The first mode on the other hand is linearly stable but nonlinearly unstable. For a cavity length  $L_3 = 0.6$  [m] the third mode is linearly unstable behaviour predicted for a length  $L_2 = 0.43$  [m] is more straightforward because in this case system is linearly unstable [41]. According to the diagram, growth rate will eventually decrease as the amplitude increases. In Fig.5.21(b) oscillation frequency expected at the limit cycle are reported. Finally, in figure Fig.5.22 schematic behaviour of the system is shown. Depending on whether  $L$  increase or decrease, different behaviour is expected and hysteresis cycle occurs. As  $L$  increase from 0.1 [m] to higher values, mode one appears first as expected at the ignition point which is linearly unstable, its amplitude increases with increasing  $L$ , reaches a maximum and decreases at the turning point ( $L=0.25\text{m}$ )(LB). There is a very narrow stable region (CE). As  $L$  is increased the supercritical bifurcation featured by the second mode appears. The level of oscillation increases (EF), reaches a maximum (at  $L=0.5$  m), then decreases near the turning point (FG) and the oscillation switches to the third mode (GH). As  $L$  decrease, the third mode is initiated first, its amplitude decreases at a point where mode hopping takes place ( $L=0.6$  m). The oscillation amplitude then jumps to a higher level and triggers mode 2 (IF). Decreasing  $L$  still further induces a decrease in the amplitude of this mode which vanishes at the supercritical bifurcation at  $L=0.28$  m (FE). A stable region is reached in this way (EC). A further decrease of  $L$  gives rise to the second mode at low amplitude (CD) while first mode is triggered at higher amplitude and it persists over the predicted range of burner sizes (AL). This hysteresis cycle is due to nonlinear effect and it occurs in several practical combustors.

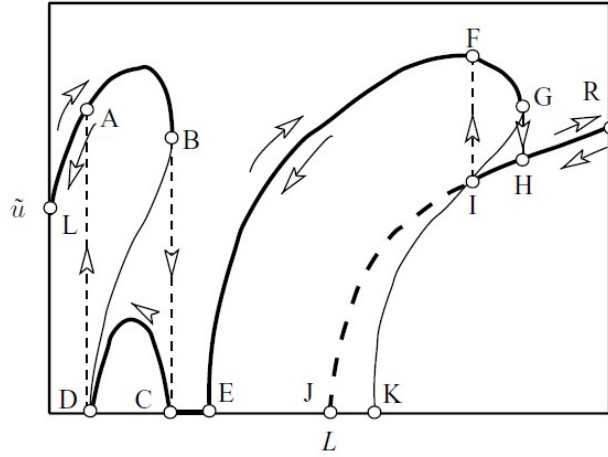


Figure 5.22: Idealized hysteresis cycle deduced from both experimental results and NDR analysis [41].

### 5.3.1 Analytical flame model

To reproduce in Comsol experimental data obtained by Noiray, analytical flame model proposed by Heckl is used [42][43]. This model considers the present heat release low in time domain

$$\frac{Q(t)}{\bar{Q}} = n_1 \frac{u(t-\tau)}{\bar{u}} - n_0 \frac{u(t)}{\bar{u}}, \quad (5.11)$$

where  $Q(t)$  is the fluctuating part of the heat release rate,  $u(t)$  is the instantaneous velocity and  $u(t-\tau)$  is a time-lagged velocity [42].  $n_0$  and  $n_1$  are real positive parameters. In frequency domain eq.(5.11) becomes

$$\frac{\hat{Q}(\omega)}{\bar{Q}} = (n_1 e^{i\omega\tau} - n_0) \frac{\hat{u}(\omega)}{\bar{u}}, \quad (5.12)$$

The gain and the phase of analytical flame model in eq.(5.12) are reported in Fig.5.23. The gain is a periodic function of  $\omega\tau$ , while the slope of the phase curve can be considered proportional to the time-lag for small values of  $\omega\tau$  (Fig.5.23(b)). Analytical flame model is applied on Noiray's test rig by Heckl [42]. Purely one-dimensional conditions are assumed, and downstream end is modelled as two adjacent interfaces where sound waves are reflected and transmitted (Fig.5.24(a)). The interface at  $x=L$  is the perforated plate, and the interface at  $x=L+\Delta$  acts like an open end. The pressure reflection and transmission coefficient for the combined interface, separating region A and region C, have been derived in [43]. If  $\Delta$  tends to zero configuration in Fig.5.24(b) is considered, and reflection ( $R_L$ ) and transmission ( $T_L$ ) coefficients become

$$R_L = \frac{R_{pp} - R_{pp}^2 R_{oe} + T_{pp}^2 R_{oe}}{1 - R_{pp} R_{oe}}, \quad (5.13)$$

$$T_L = \frac{T_{pp} T_{oe}}{1 - R_{pp} R_{oe}}, \quad (5.14)$$

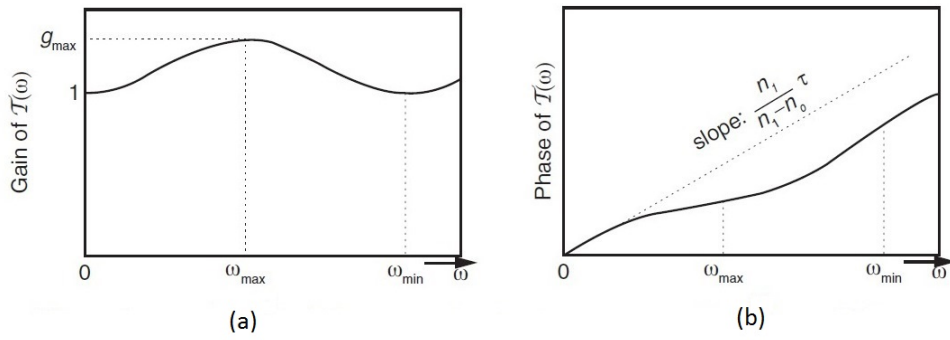


Figure 5.23: Analytical flame transfer function corresponding to eq.(5.11): (a) the gain, (b) the phase [42].

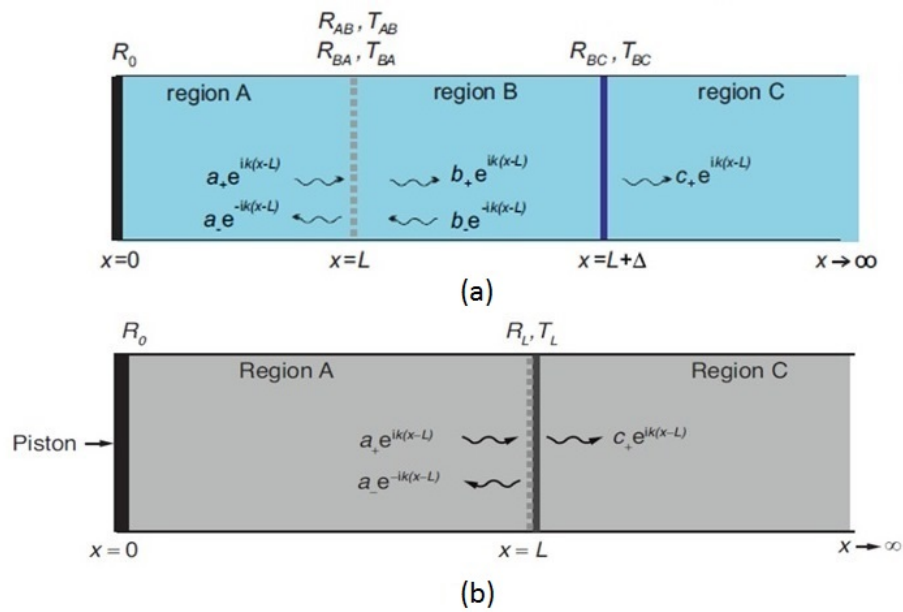


Figure 5.24: Configuration of numerical model [42].

Table 5.3: Noiray test rig conditions

Description	Value
Duct radius	0.75 m
Range of tube lengths	0.1...0.8 m
Thickness of perforated plate	0.003 m
Number of perforations per unit area of plate	$1.09 \cdot 10^5 \text{m}^{-2}$
Radius of perforations	0.001 m
Speed of sound	345 m/s
Specific heat ratio	1.4
Factor relating $q(t)$ and $Q(t)$	$3 \cdot 10^5 \text{m}^2 \text{s}^{-2}$

where  $R_{pp}$ ,  $T_{pp}$  are reflection and transmission coefficients of the perforated plate, while  $R_{oe}$  and  $T_{oe}$  are coefficients of unflanged open tube and they are dependent on the number of holes per unit area, the speed of sound, the radius of the tube

and the Rayleigh conductivity [42]. The parameters describing the experimental combustion rig are reported in Tab.5.3. Flame model of eq.(5.12) is used for stability investigation, with  $n_0$  and  $n_1$  chosen in such a way that at  $\omega = 0$  the gain is equal to one, and at  $\omega_{\max}$  the gain is  $g_{\max}$  [42]. This requires

$$n_1 - n_0 = 1, \quad (5.15)$$

$$n_1 + n_0 = g_{\max}. \quad (5.16)$$

In Heckl's work, according with experimental results reported by Noiray, parameters are set as  $g_{\max} = 1.34$  and  $\omega_{\min} \simeq 2\pi \cdot 1050 \text{ s}^{-1}$  which gives  $\tau = 0.95 \cdot 10^{-3} \text{ s}$ . The gain has linear dependence on amplitude, while for time delay quadratic behaviour is considered. In particular

$$g_{\max} = g_0 - g_1 \left( \frac{u'}{u} \right), \quad (5.17)$$

$$\tau = \tau_0 - \tau_2 \left( \frac{u'}{u} \right)^2 \quad (5.18)$$

with  $g_0 = 1.42$ ,  $g_1 = 0.3$ ,  $\tau_0 = 0.94 \cdot 10^{-3} \text{ s}$  and  $\tau_2 = 2.5 \cdot 10^{-3} \text{ s}$ . From analytical FTF in eq.(5.12), using eq.(5.15) and eq.(5.16) with relations of eq.(5.17) and (5.18), analytical FDF is obtained

$$FDF(\omega, r) = n_1(r) e^{i\omega\tau(r)} - n_0(r). \quad (5.19)$$

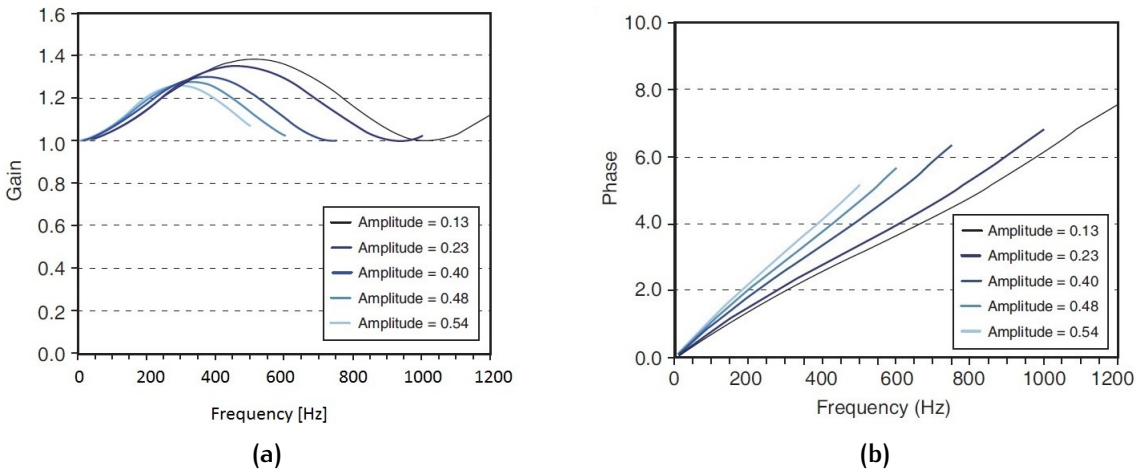


Figure 5.25: Analytical flame describing function: (a) the gain, (b) the phase [42].

### 5.3.2 Numerical results in Comsol

To reproduce bifurcation diagram of Noiray's test rig in Comsol, analytical model of eq.(5.19) is used. 3D cylindrical geometry is considered, and the operating conditions of Tab.5.3 are set. The computational mesh is the same of Fig.5.1. To model the piston closed boundary conditions is applied, while for represent perforated

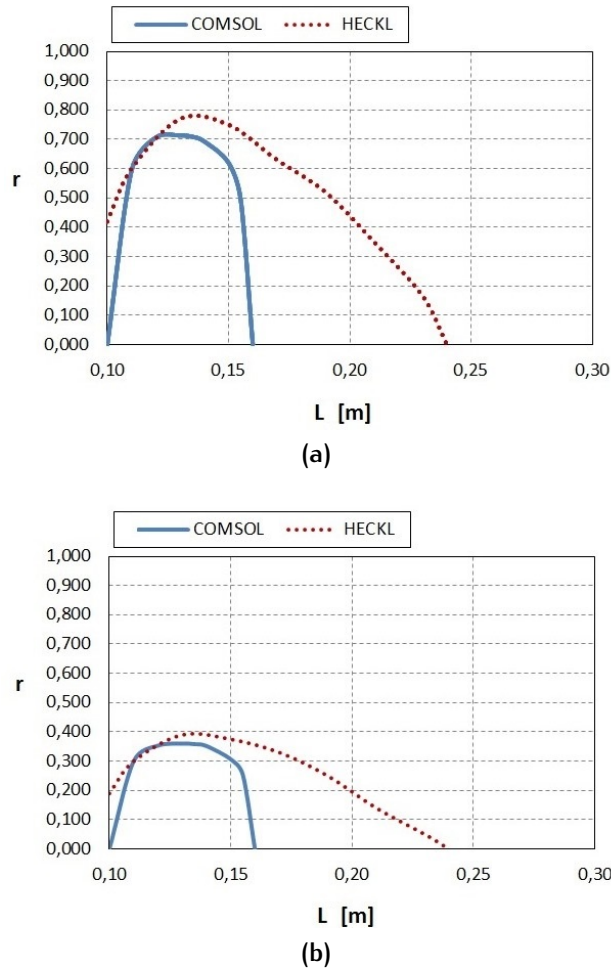
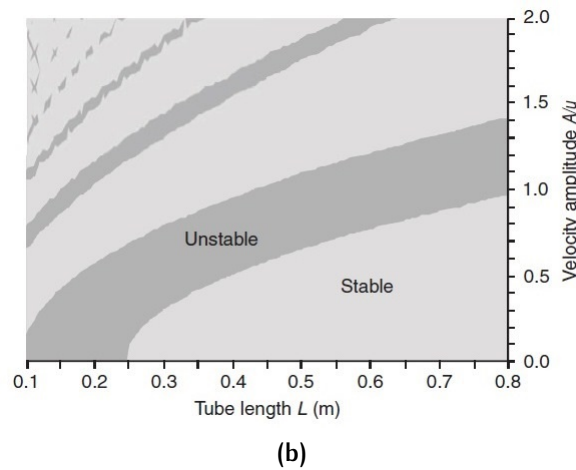
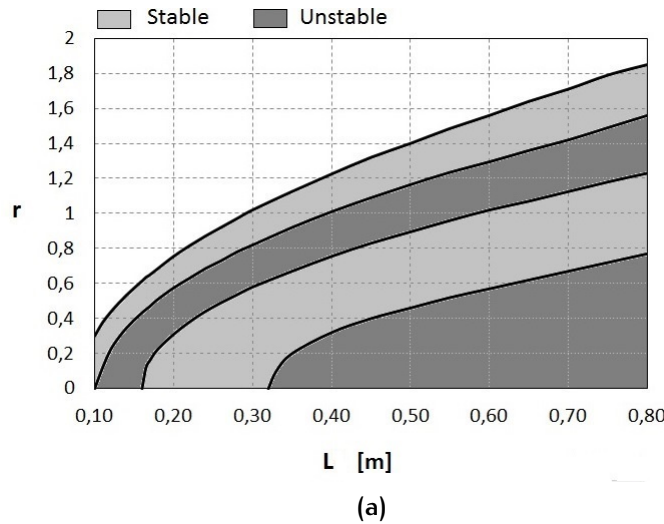


Figure 5.26: Bifurcation diagram of the first axial mode of Noiray's test rig with flame model of eq.(5.19),  $g_0 = 1.42$ ,  $\tau_0 = 0.94 \cdot 10^{-3}$  s and  $\tau_2 = 0$ s; (a)  $g_1 = 1$ , (b)  $g_1 = 2$ .

plate, acoustic impedance is set considering coefficients in eqs.(5.13) (5.14). Bifurcation diagram of the first axial mode is obtained varying the length of the zone after the flame. In particular, for each value of chamber length, zero growth rate condition is evaluated. In [42] stability conditions are evaluated using Green's function approach and modelling the flame zone as an infinitesimal section. In Comsol different approach is followed. In particular, volumetric heat release zone must be considered and calibration of the amplitude is required. In fact, it is possible to change the input amplitude of  $NFTF$ , but the value of  $u'$  in linear model is evaluated iteratively from the solver, and it cannot be set. Hence, to consider the same amplitude in flame model, a calibration coefficient  $\lambda$  must be inserted. To calibrate the model in Comsol, several test are carried out using parametric study of analytical flame model in [42] as benchmark. This analysis computed by Heckl shows the influence of  $g_1$  and  $\tau_2$  coefficients on bifurcation diagram. Considering data with constant  $\tau_2$  and variable  $g_1$ , value of calibration coefficient  $\lambda$  is defined. In particular,  $\tau_2$  is set equal to zero and  $g_1$  is varied from 0 to 2. Considering  $\bar{g} = \lambda \cdot g_1$  with  $\lambda = 0.3$  and replacing  $\bar{g}$  to  $g_1$  in equation eq.(5.17) results in Fig.5.26 are reproduced. The maximum amplitude of bifurcation diagram is similar but the Hopf

point evaluated by two numerical approaches are different. However, to calibrate Comsol model, the peak of bifurcation diagram must be considered, in order to set the correct amplitude in the flame model. In this way gain of FDF is properly evaluated and nonlinear analysis can be performed. Maximum correlation is obtained setting  $\lambda = 0.3$ .

To confirm calibrated model, case of  $\tau_2 = 2.5$  ms and  $g_1 = 0.3$  is tested. For several values of  $L$ , amplitude  $r$  is varied and stable or unstable zones are evaluated (Fig.5.27(a)). The results show the presence of a main band, with other several mi-



**Figure 5.27:** Bifurcation diagram of the first axial mode of Noiray’s test rig with flame model of eq.(5.19),  $g_0 = 1.42$ ,  $g_0 = 0.3$ ,  $\tau_0 = 0.94 \cdot 10^{-3}$ s and  $\tau_2 = 2.5 \cdot 10^{-3}$ s; (a) Comsol results (b) Green’s function results [42].

nor bands with decreasing width. These predictions capture the behaviour at low amplitudes, in particular the linear stability range and the limit cycle amplitudes for low  $L$  values. However, this flame model predicts a band of instability, which spans the whole  $L$  range, while Noiray’s instability region has the shape of a *tongue*, which does not extend beyond  $L$  values of 0.16 m (Fig.5.21(a)). Comparison between Comsol results and Green’s function approach are reported in Fig.5.27. In Comsol the same behaviour of stable and unstable zone obtained by Heckl are reproduced.

Also, another unstable zone occurs for low amplitude and from  $L = 0.32$  m, but the first Hopf point is evaluated for  $L = 0.16$  m in greater agreement with experimental data. Second test is reported in [42] with  $g_1 = 1$  instead of 0.3. The stability map looks quite different, as shown in Fig.5.28. The behaviour of bifurcation diagram is

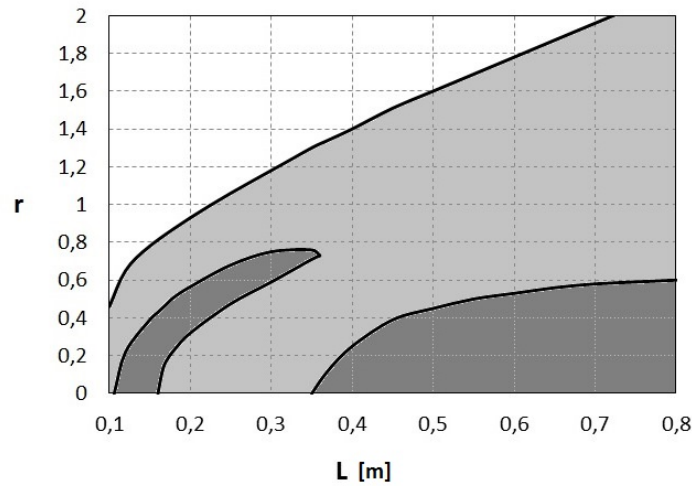


Figure 5.28: Bifurcation diagram obtained in Comsol with flame model of eq.(5.19),  $g_0 = 1.42$ ,  $g_1 = 1$ ,  $\tau_0 = 0.94 \cdot 10^{-3}$  s and  $\tau_2 = 2.5 \cdot 10^{-3}$  s.

similar to the experimental one obtained by Noiray. As  $L$  increases, unstable zone occurs at higher value of amplitude, and it remains for gradually lower range of  $r$  until the fold point at  $L = 0.35$  m. So, better agreement with experimental data is obtained increasing  $g_1$  from extrapolation value of 0.3 to empiric value of 1. This can be explained by the fact that analytical FDF overestimates gain value. Hence, a higher value of  $g_1$  reduces overall gain, and then greater agreement between analytical FDF and experimental one is obtained.

In Fig.5.29 a comparison between experimental bifurcation diagram and numerical results is reported. Limit cycle obtained with Helmholtz solver is similar to the one determined with Green's function approach. In particular Hopf point of experimental limit cycle is correctly evaluated, and fold point occurs at amplitude  $r \approx 0.7$  according to reported data. Differences between two numerical results are due to different equation solution. Comsol makes use of a Helmholtz solver while Heckl used Green's function approach. Also, in FEM code 3D geometry and volumetric heat release zone are considered.

Finally, a parametric study on  $g_1$  value is performed to optimize numerical results. In particular, setting  $g_1$  equal to 1.33 instead of 1 a greater agreement with Noiray's results is obtained (Fig.5.30). The higher value of  $g_1$  is due to overestimation of the gain by the analytic FDF.

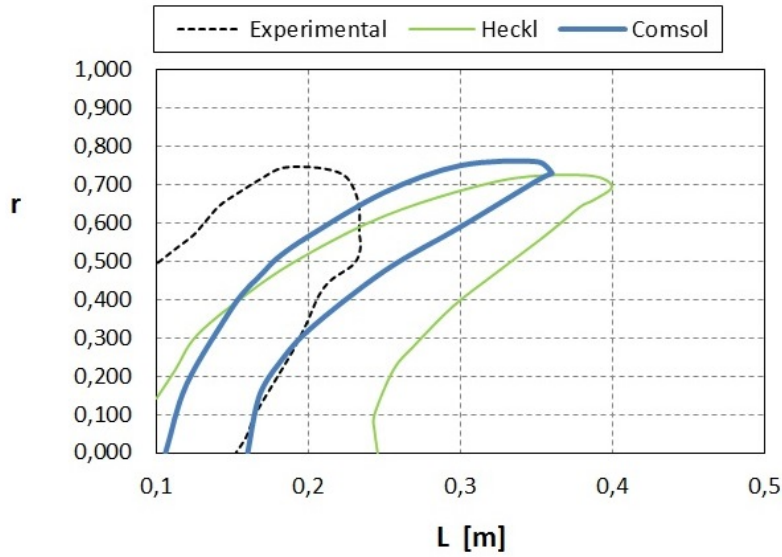


Figure 5.29: Comparison between experimental bifurcation and numerical results,  $g_1 = 1$ .

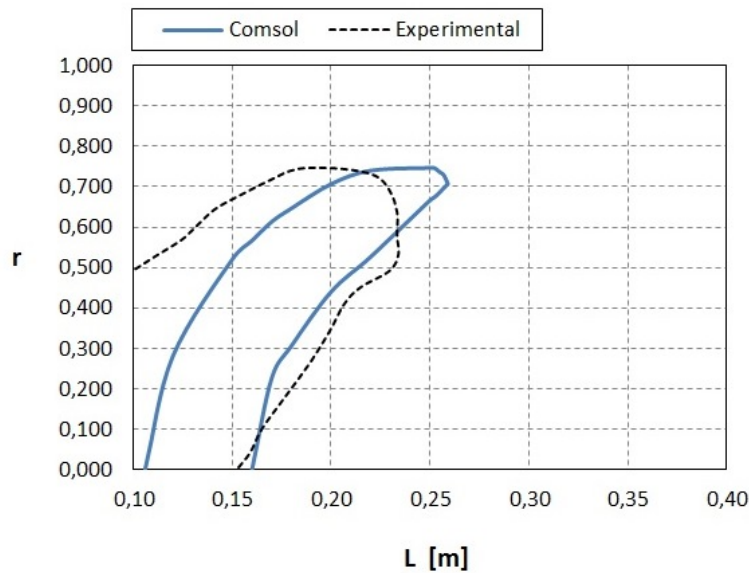


Figure 5.30: Comparison between experimental bifurcation and numerical results,  $g_1 = 1.33$ .

## 5.4 EXPERIMENTAL TEST OF PALIES

In order to confirm Comsol approach, a further experimental test rig is considered. In particular the results obtained by Palies are reproduced [44][45]. In this experimental test, FDF approach was applied on the dynamics of turbulent flames formed by a swirling injector in a confined geometry. Swirling injection is used in many practical systems like jet engines or gas turbine combustors. Experimental setup is formed by a combustor which comprises an upstream manifold including a settling chamber, a contraction ended by a constant diameter duct equipped with the swirler, a horizontal end piece and a cylindrical flame tube (Fig.5.31). An

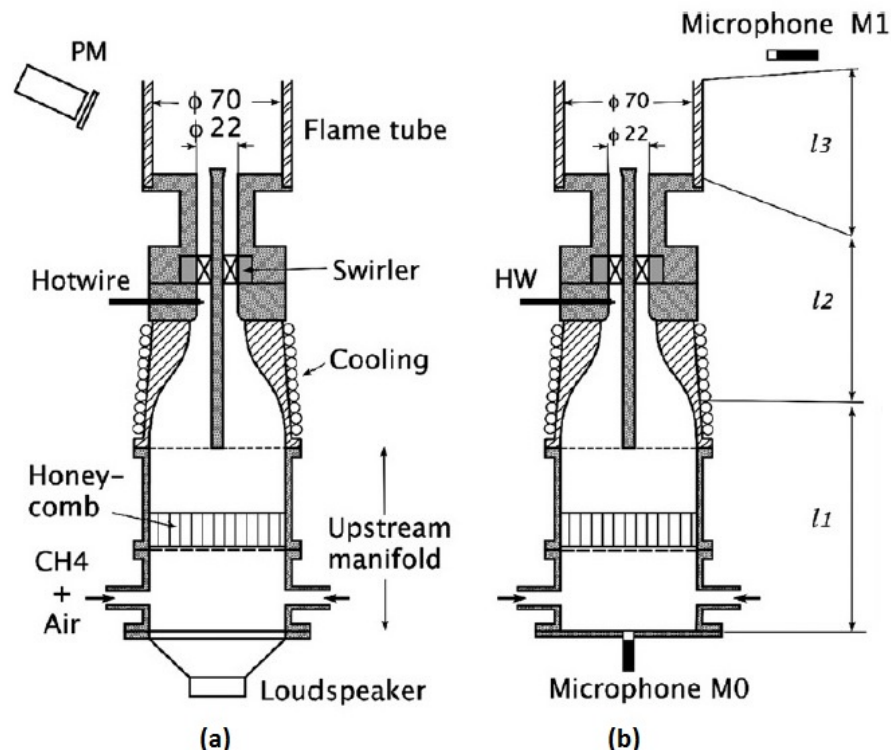


Figure 5.31: Experimental test rig of Palies [45].

air/methane premixed flow is delivered to the feeding manifold unit through two diametrically opposed apertures. The flow then crosses a grid and a honeycomb to break the largest turbulent scales. The gas then traverses a converging section to decrease the boundary layer thickness, reduce the level of turbulence and flatten the velocity profile at the swirler inlet. The flow rotation is generated by the swirler which generates a swirl number about 0.55 [45]. The tube diameter is 70 mm and the length of zone after the flame can take different values  $L_3 = 100, 150, 200$  and 400 mm respectively. There are also three lengths  $L_1$  available for the upstream manifold: short (96 mm), medium (160 mm) and long (224 mm). The upstream manifold diameter is 65 mm. More details are given in [45]. The temperature varies from 300 K in zone before the flame, to 1600 K in chamber zone. A loudspeaker is placed at the back end of this system to measure the flame describing function (Fig.5.31(a)). It was used to generate harmonic perturbations and oscillations in the flow to recreate combustion instability. So, the loudspeaker was removed, and setup of figure Fig.5.31(b) was used to obtain frequencies and amplitudes of velocity disturbances  $u'/U$  under self-sustained limit cycle operation. In particular, perturbations of the system was recorded with a microphone ( $M_0$ ) located at the base of the burner, while a second microphone ( $M_1$ ) placed in front of the loudspeaker provided a reference signal. FDF was obtained by modulating the flame with a loudspeaker and by simultaneously measuring the velocity oscillation with a hot wire anemometer and the heat release rate perturbation with a OH detector [45]. Experimental results obtained by Palies are reported in Fig.5.32. The gain decreases in a first range between 0 and 60 Hz to a value of less than 0.5 and it increase to value of 1.2 from 60 to 100 Hz. Each curve features a peak which is dependent on

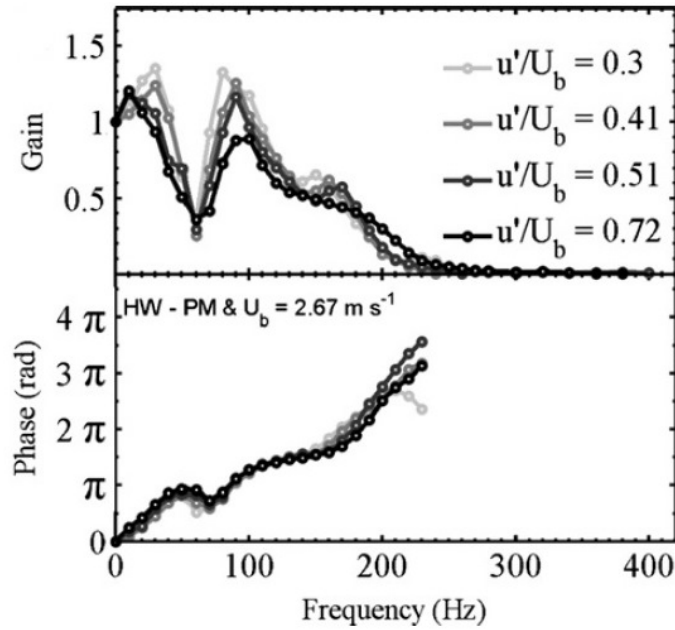


Figure 5.32: Experimental FDF obtained by Palies [45].

value of amplitude. Finally, at high frequency, the gain decreases to zero. This behaviour is in agreement with several other FDF measured and reported in literature. The behaviour is similar for all amplitude inspected, with difference in peak values at 60 and 100 Hz. The phase is lower dependent from amplitude, and in the range of interest, it can be considered the same for all amplitude. Furthermore, phase's behaviour is quite linear and, with fair approximation, proportional relation between  $\tau$  and  $\omega$  can be considered. For this configuration time delay was estimated at 5 ms [45], and since the amplitude influence is very low, it can be considered constant. From experimental analysis was also evaluated a damping rate of combustor system  $\zeta$ . This coefficient is used to evaluate the stability condition of the system. In fact, according to several literature approaches, if growth rate is lower than  $\zeta$  oscillations amplitude is damped and the system evolves to stable conditions. Then, if  $\omega_i > \zeta$  unstable condition is expected, while for  $\omega_i < \zeta$  stable condition occurs. For Palies test rig  $\zeta$  was evaluated equal to  $0.55 \text{ s}^{-1}$  [45]. At condition reported before, for each length of upstream manifold considered ("short", "medium" and "long" configurations), length of chamber was varied and *rms* of pressure was measured in order to evaluate stability conditions (Fig.5.33). To reproduce stability map of the first mode of the system, numerical simplified model was used by Palies [45]. He considered simplified one dimensional geometry and infinitesimal heat release zone to model the flame. Solving an eigenvalue problem unstable conditions were evaluated. Results obtained for "medium" and "long" configuration are reported in Fig.5.34. The stability map shows the value of  $\omega_i - \zeta$ . Hence, at condition of growth rate equals to damping ratio (plotted in white zone) bifurcation diagram is evaluated. For  $\omega_i > \zeta$  unstable zone is expected, and as value of  $\omega_i - \zeta$  increases, stronger unstable conditions occur. For "medium" configuration Hopf point is evaluated at  $L_3=190 \text{ mm}$ , while in "long" configuration it moves to  $L_3 \approx 220 \text{ mm}$ . In both cases alternated subcritical and supercritical bifurcations occur.

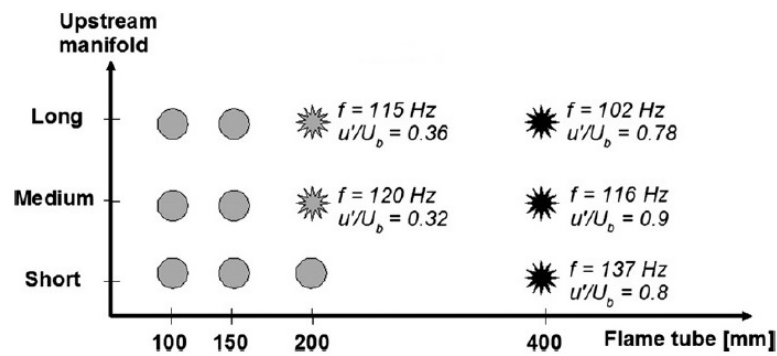


Figure 5.33: Measure of the stability conditions of the combustor. Stable configurations are indicated with gray circles while black stars indicate a high level of rms pressure fluctuation corresponding to a self-sustained oscillation of the system. Gray stars indicate a slightly unstable configuration. [45].

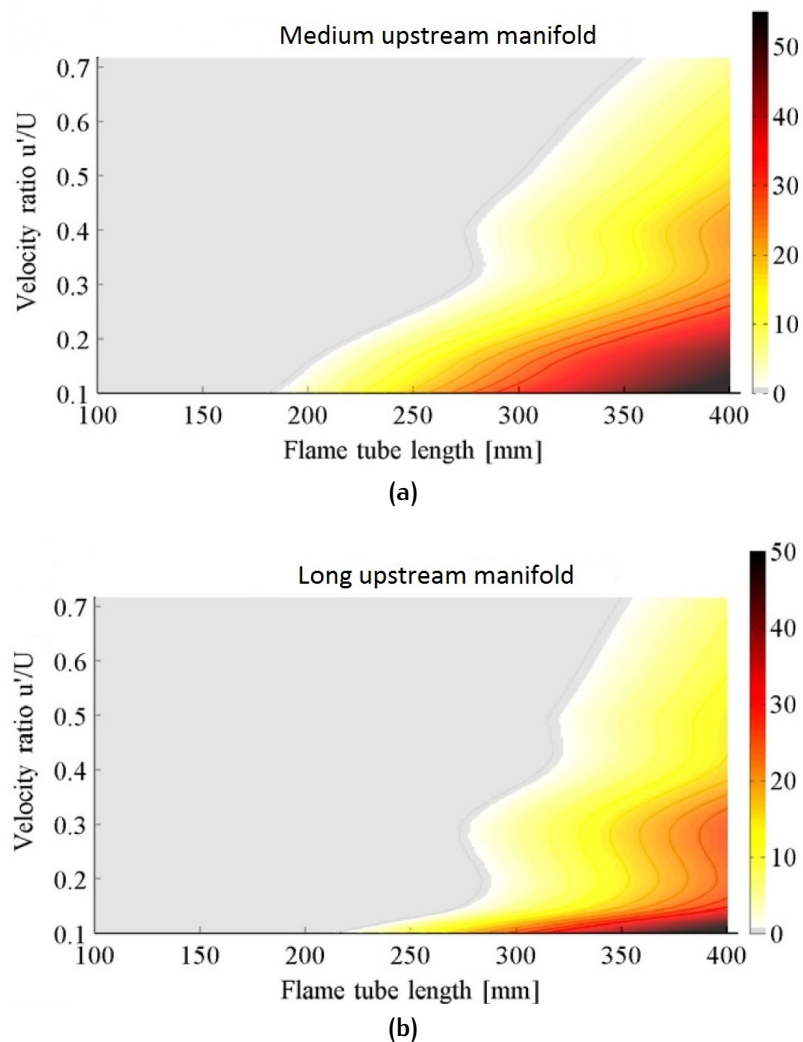


Figure 5.34: Stability maps obtained by Palies. The colorbar indicates values of  $\omega_i - \zeta$  in  $s^{-1}$  (negative values correspond to the gray region). The line separating gray and white regions corresponds to points where  $\omega_i - \zeta = 0$  meaning that the limit cycle is reached [45]. (a) "Medium" configuration ( $L_1=181.3$  mm), (b) "Long" configuration ( $L_1=245.3$  mm).

## 5.4.1 Numerical results

To reproduce in Comsol stability conditions of Palies test rig, the same geometry and operating conditions in [45] are considered. To model heat release in frequency domain, eq.(5.20) is applied.

$$\frac{\hat{q}}{\bar{q}} = NFTF\left(\frac{\hat{u}}{\bar{u}}\right) \cdot \frac{\hat{u}}{\bar{u}} e^{i\omega\tau} \quad (5.20)$$

Time delay is set constant and equal to 5 ms, while the *NFTF* is extrapolated from experimental gain data of FDF. In particular, piecewise function of frequency is considered (eq.(5.21)). A harmonic function approximates gain of FDF in frequency range between 0 and 87 Hz, while the remaining part is modelled with an exponential function.

$$G_{FDF} = \begin{cases} 0.7 + \xi_1 \left(\frac{u'}{\bar{u}}\right) \cdot \cos\left(\left(\frac{f}{4\pi}\right) - \varphi\right) & \text{if } f < 87 \text{ Hz,} \\ \xi_2 \left(\frac{u'}{\bar{u}}\right) \cdot e^{-0.017f} & \text{if } f \geq 87 \text{ Hz.} \end{cases} \quad (5.21)$$

To consider amplitude influence,  $\xi_1$  and  $\xi_2$  parameters are inserted. Good agreement with experimental data is obtained setting  $\varphi$  equal to 1.2 and using linear behaviour in eqs.(5.22)(5.23) for  $\xi_1$  and  $\xi_2$ .

$$\xi_1 = 0.85 - 0.7 \left(\frac{u'}{\bar{u}}\right) \quad (5.22)$$

$$\xi_2 = 6.35 - 2.9 \left(\frac{u'}{\bar{u}}\right) \quad (5.23)$$

In Fig.5.35, for each value of  $r = u'/\bar{u}$ , a comparison between experimental and analytical gain of FDF is reported. Analytic function is in good agreement with experimental data especially in the range of interest for the acoustic mode studied. In particular, the mode considered is reported in Fig.5.36(c) and it occurs in a range between 110 and 125 Hz depending on conditions tested. Hence, only  $G_{FDF}$  exponential function is considered. The experimental test rig is modelled with a geometry in Fig.5.36(a) while the computational mesh is shown in Fig.5.36(b). As illustrated in section 5.3.2, to proceed with Comsol test, calibration of the system is required. Calibration is based on results of Fig.5.34, and it considers two coefficients  $\lambda_1$  and  $\lambda_2$  which affect the gain of FDF in a range of  $f > 87$  Hz:

$$NFTF(r, f) = 10^7 \cdot \lambda_1(r) \xi_2(r) \cdot e^{-\lambda_2 0.017f} \quad (5.24)$$

In particular,  $\lambda_1$  coefficient depends on amplitude, while  $\lambda_2$  is constant. In this way, *NFTF* of the flame model is founded. For each configuration of upstream manifold, different values of  $\lambda_1$  and  $\lambda_2$  are applied. Also, to obtain bifurcation diagram, two different relations between  $\lambda_1$  and amplitude  $r$  are tested. At first, power function is tested.

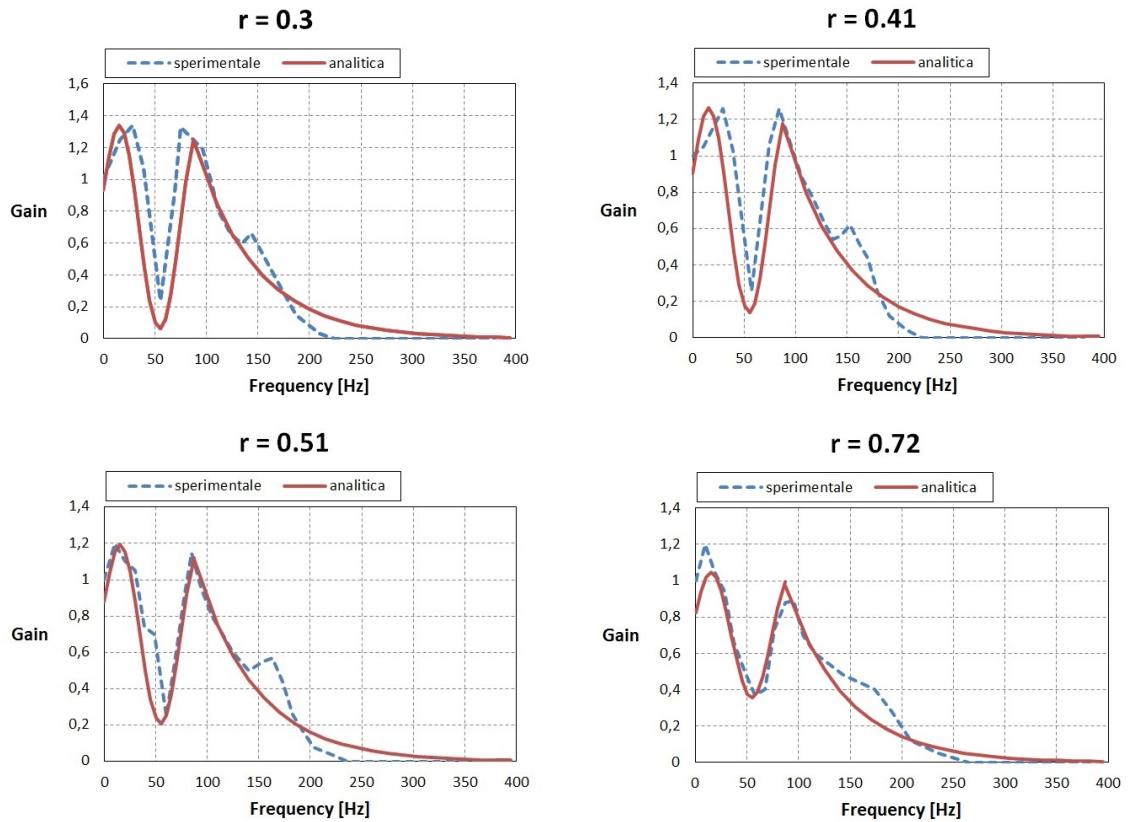


Figure 5.35: Comparison between experimental and analytic FDF.

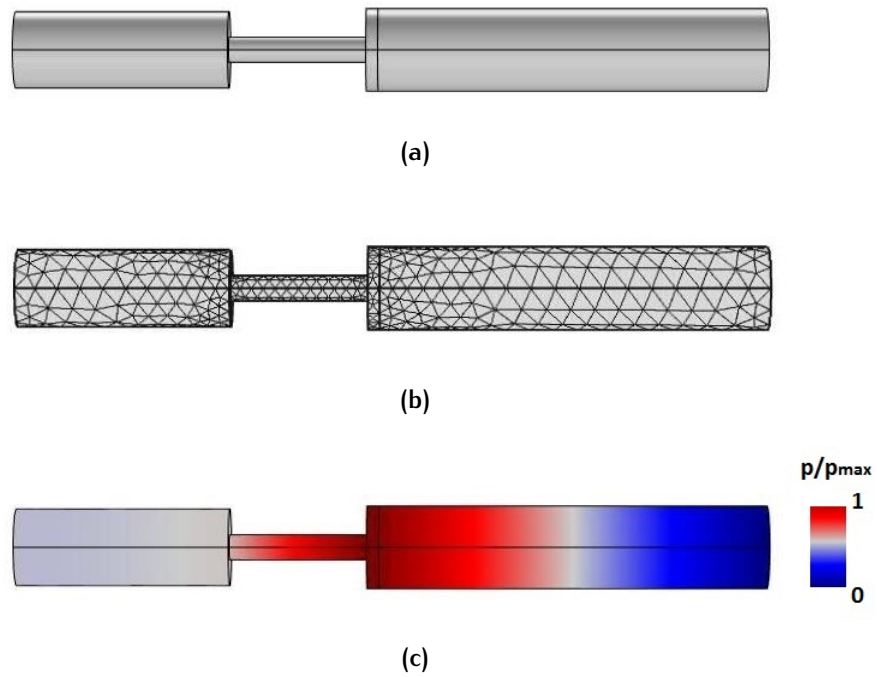


Figure 5.36: Numerical model of test rig: (a) geometry, (b) computational mesh, (c) acoustic mode studied.

For "medium" configuration ( $L_1=160$  mm), calibration coefficients are evaluated as

$$\lambda_{1M} = 0.1 r^{-0.25} \quad (5.25)$$

$$\lambda_{2M} = 6.3. \quad (5.26)$$

For these relations, as performed in [45], limit condition of  $\omega_i = 55 \text{ s}^{-1}$  is searched for, and bifurcation diagram is obtained (Fig.5.37(a)). According to Palies's results, Hopf point is evaluated at  $L_3 = 180$  mm and an increase of curve slope occurs at flame tube length equal to 280 mm. However, the subcritical bifurcation which occurs in a little range of amplitude between  $r= 0.3$  and  $r= 0.4$  is not reproduced. This is due to the expression of calibration coefficient in eq.(5.25), which however leads to results in good agreement with the ones obtained by Palies. For "long" configuration of test rig, calibration coefficients are set as

$$\lambda_{1L} = 0.96 r^{-0.12} \quad (5.27)$$

$$\lambda_{2L} = 7.647. \quad (5.28)$$

The results obtained are reported in Fig.5.37 (b). The Hopf point is correctly evaluated in  $L_3 = 220$  mm while the fold points, which occur in Palies's data at  $L_3 = 285$  mm and at  $L_3 = 320$  mm, are not reproduced. In particular, an alternated supercritical and subcritical bifurcation diagrams occur while in Comsol supercritical bifurcation is obtained. However conservative beginning of instability is predicted.

The results obtained with the power expression of  $\lambda_1$  are in good agreement with numerical data obtained by Palies, but at low amplitude theoretical singularity occurs. In particular, in experimental data the amplitude of velocity ratio starts at  $r=0.1$ , but if  $r=0$  the eqs.(5.25)(5.27) lead to  $\lambda_1 \rightarrow \infty$ . To solve this problem polynomial function is tested. In this way, also  $r= 0$ ,  $NFTF$  is constant value and linear analysis can be performed. So, for "medium" configuration, expression reported in eq.(5.29) is applied to  $\lambda_{1M}$ , while  $\lambda_{2M}$  is set as in eq.(5.26). For "long" configuration, expression of  $\lambda_{1L}$  and  $\lambda_{2L}$  are reported in eqs.(5.30)(5.28).

$$\lambda_{1M} = 0.347 r^2 - 0.3881 r + 0.222 \quad (5.29)$$

$$\lambda_{1L} = 1.936 r^2 - 2.075 r + 1.567 \quad (5.30)$$

Results obtained are shown in Fig.5.38. In both cases good agreement with Palies's data is obtained at lower amplitude, but for  $r > 0.5$  increase of curve slope occurs. Hence, to reproduce bifurcation diagram, piecewise expression of coefficient  $\lambda_1$  is considered. At high amplitude power relation may be set, while to eliminate the singularity at low amplitude, polynomial dependence is applied. In particular, expressions of  $\lambda_1$  for "medium" and "long" configuration are reported in eqs.(5.31)(5.32).

$$\lambda_{1M} = \begin{cases} 0.347 r^2 - 0.3881 r + 0.222 & r < 0.33 \\ 0.1 r^{-0.25} & r \geq 0.33 \end{cases} \quad (5.31)$$

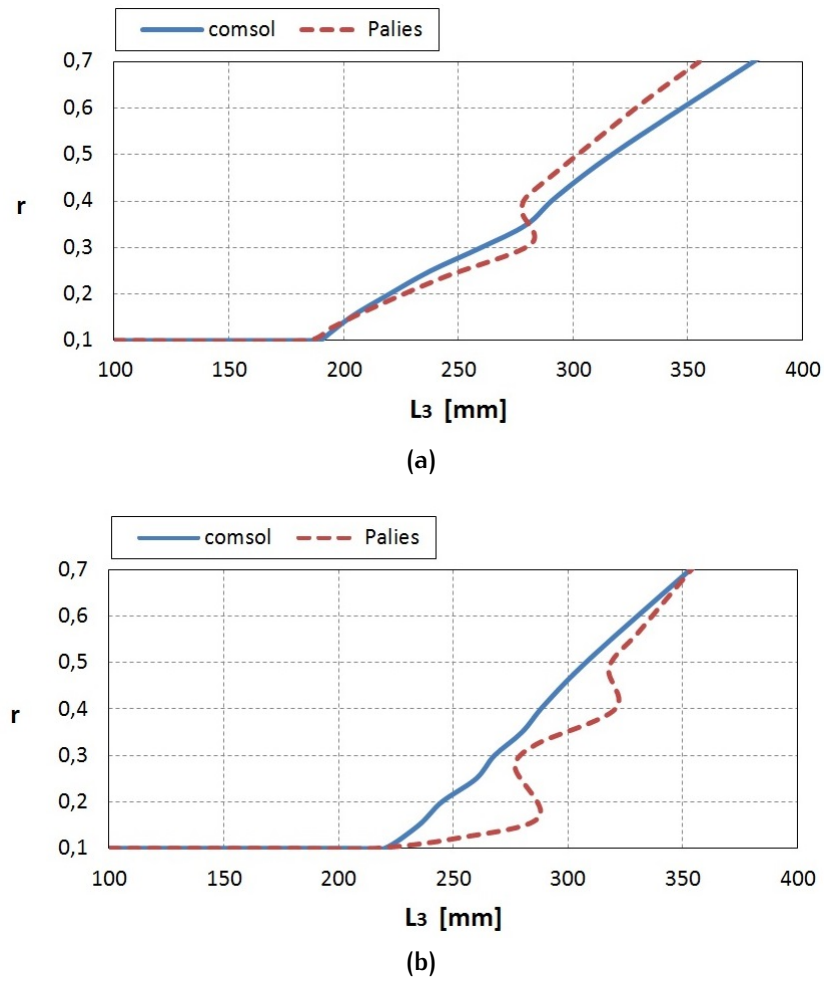


**Figure 5.37:** Comparison between bifurcation diagram obtained by Palies and Comsol results obtained with power function for  $\lambda_1$ : (a) "medium" configuration, (b) "long" configuration.

$$\lambda_{1L} = \begin{cases} 1.936 r^2 - 2.075 r + 1.567 & r < 0.33 \\ 0.96 r^{-0.12} & r \geq 0.33 \end{cases} \quad (5.32)$$

Replacing  $\lambda_1$  and  $\lambda_2$  in eq.(5.24) with expression of (5.31) and (5.26) for "medium" configuration, and with eqs.(5.32)(5.28) for "long" geometry, results in Fig.5.39 are obtained. The bifurcations diagram obtained by Comsol are similar to the ones obtained by Palies, especially in geometry with medium upstream manifold. In the "long" configuration conservative stability prediction is obtained. Hence, calibration with piecewise function leads to results more similar to the ones performed with power expression, but it removes the singularity which occurs at low amplitude in power function model.

NUMERICAL TESTS

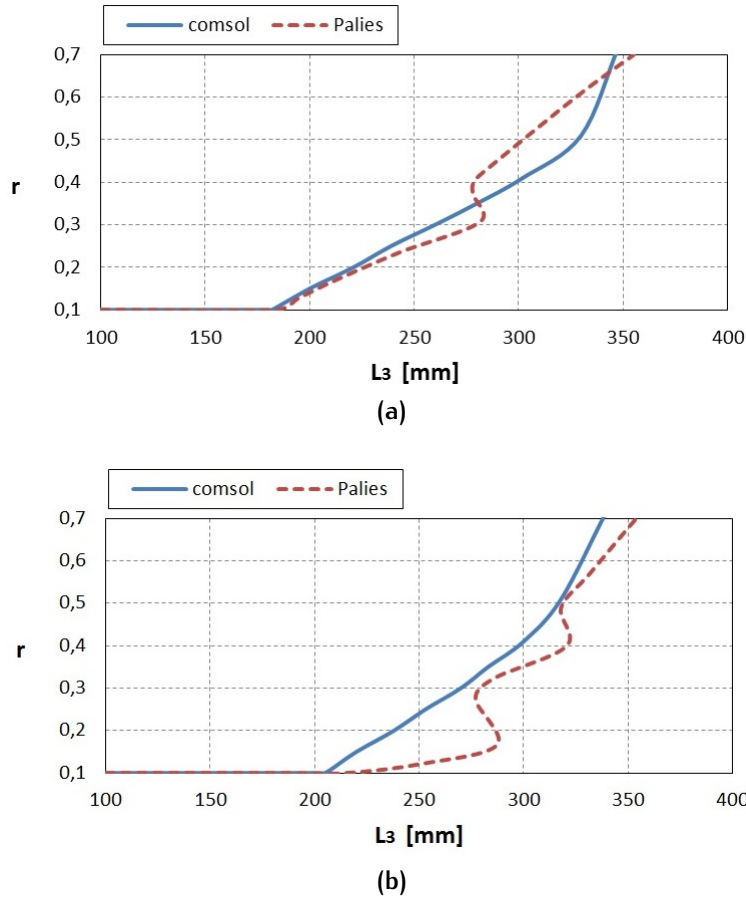


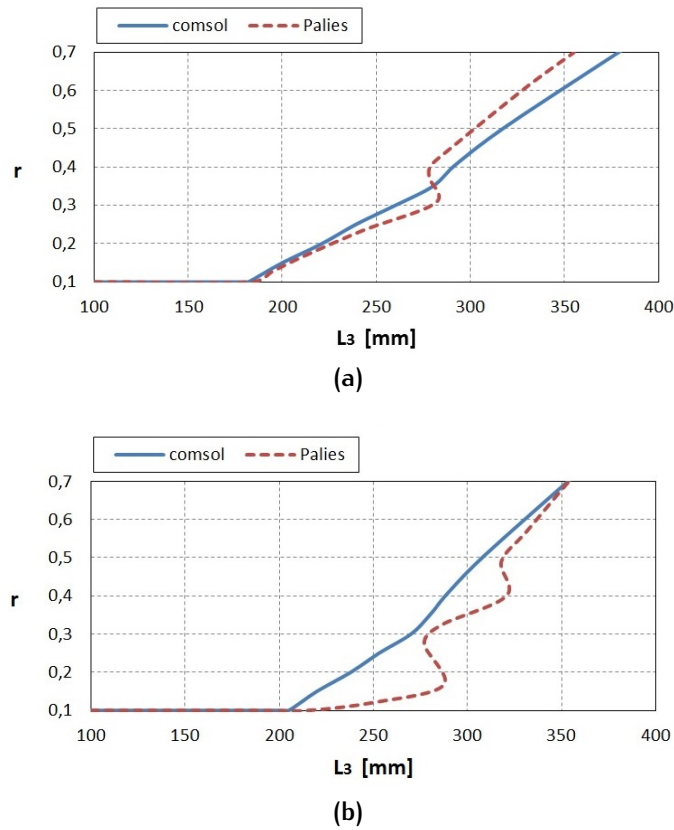
Figure 5.38: Comparison between bifurcation diagram obtained by Palies and Cmsol results obtained with polynomial function for  $\lambda_1$ : (a) "medium" configuration, (b) "long" configuration.

Table 5.4: Comparison of experimental and numerical predicted frequency of the mode in Fig.5.36c for the medium (M) and long (L) upstream manifold with the two flame tube size  $L_3 = 200, 400$  mm at  $r = 0.1$ .

	Frequency (Exp) Hz	Frequency (Pred) Hz
M-200	120	122
M-400	116	117
L-200	115	118
L-400	113	102

A comparison between experimental and predicted frequencies of the mode studied is reported in Tab.5.4. The calculated frequencies are quite close to the experimental values, confirming the described approach.

To complete the study, stability map of the system is reproduced. For each amplitude, varying flame tube length in unstable zone, value of  $\omega_i - \zeta$  is evaluated. In this way, results of Fig.5.40 are obtained. As flame tube length increase, value of  $\omega_i - \zeta$  grows, and the system evolves to more unstable conditions. Comparing the stability maps reproduced in Cmsol and the ones obtained by Palies in (Fig.5.34),



**Figure 5.39:** Comparison between bifurcation diagram obtained by Palies and Comsol results obtained with flame model in (5.24): (a) "medium" configuration with  $\lambda_{1M}$  in (5.31) and  $\lambda_{2M}$  in (5.26) , (b) "long" configuration with  $\lambda_{1L}$  in (5.32) and  $\lambda_{2L}$  in (5.28).

can be evaluate the accuracy of the model. The good agreement with numerical results confirms the ability to perform a nonlinear thermoacoustic analysis in Comsol, even if a calibration of the flame model must be considered.

#### 5.4.2 Influence of damping coefficient

In [45] is reported the procedure to measure the damping coefficient of the system. In particular, for Palies's test rig,  $\zeta$  is evaluated equal to  $0.55 \text{ s}^{-1}$ . This value is compared to growth rate in order to obtain the bifurcation diagram. The damping coefficient is a property of particular test rig, and it depends on the geometry of the burner. Hence, to evaluate the damping coefficient influence on stability, various test are performed in Comsol using the flame model in eq.(5.24). The same bifurcation diagram obtained for "medium" configuration is considered, but the beginning of unstable conditions is displaced from growth rate equal to  $\zeta$  to two different coefficients  $\zeta_1$  and  $\zeta_2$ . In particular, cases with  $\zeta_1 = 0.5 \text{ s}^{-1}$  and  $\zeta_2 = 0.6 \text{ s}^{-1}$  are considered, and the influence on  $\lambda_{1M}$  is studied maintaining  $\lambda_{2M}=6.3$ . Results are shown in Fig.5.41. The variation of damping coefficient of test rig leads to an alteration of  $\lambda_1$ . However the qualitative behaviour is the same. So, calibrated flame model can be used for qualitative investigation of combustion instability in test rig with different damping coefficient.

NUMERICAL TESTS

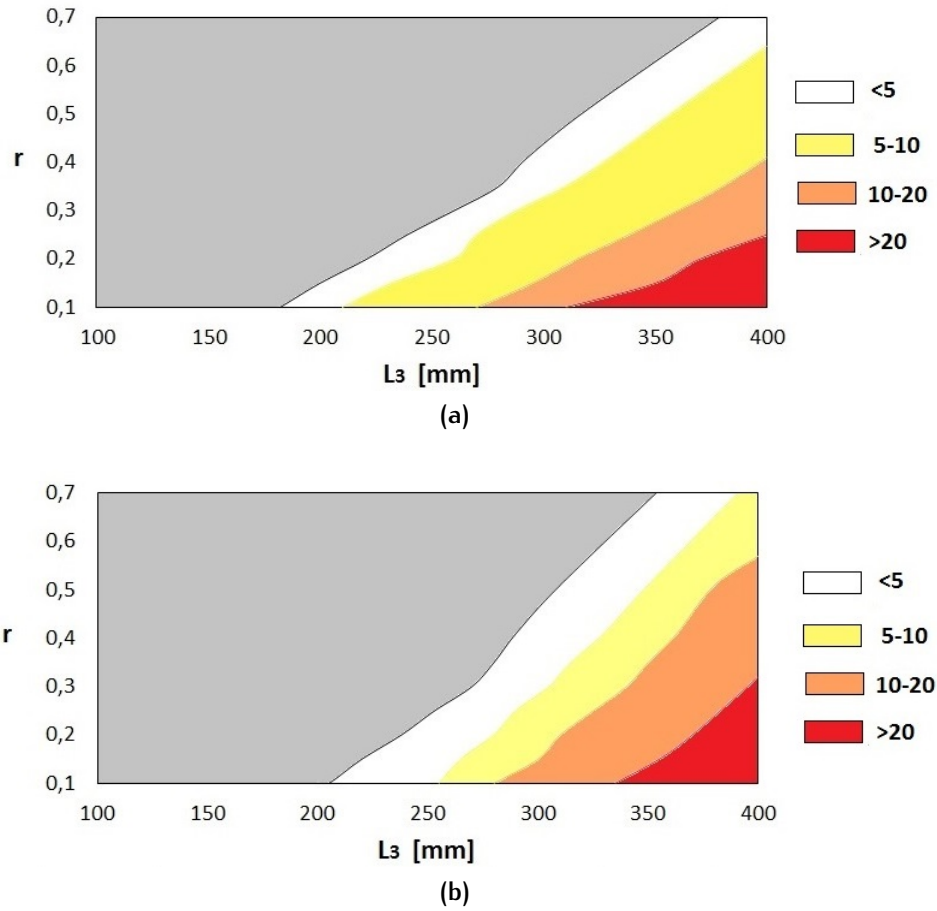


Figure 5.40: Stability maps of test rig obtained in Comsol. The color zones indicates values of  $\omega_i - \zeta$  in  $s^{-1}$ . (a) "medium" configuration, (b) "long" configuration.

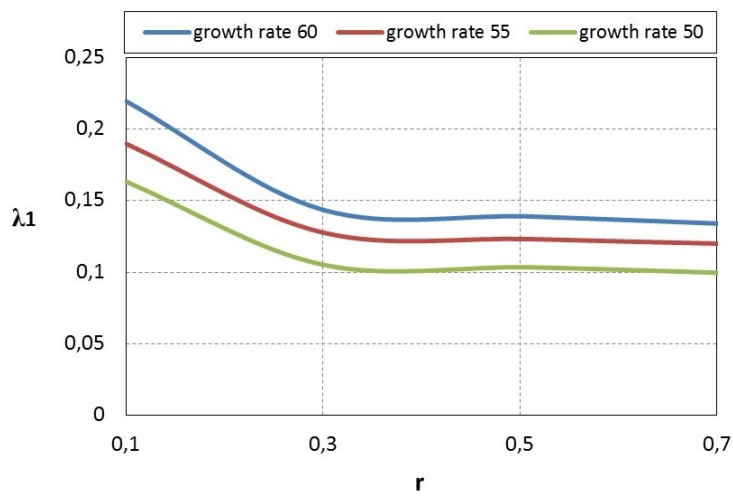


Figure 5.41: Influence of damping on calibration coefficient  $\lambda_1$ .

---

# 6

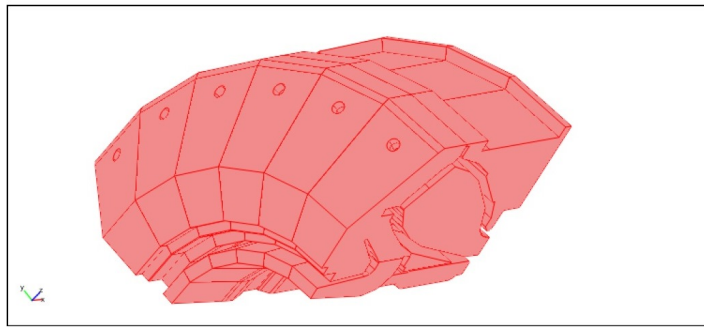
## ANSALDO MACHINE AE94.3A

---

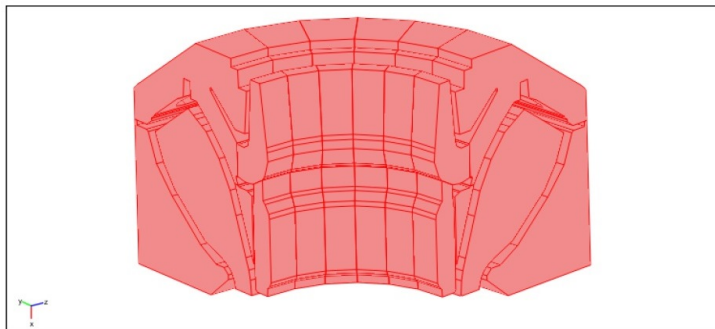
This chapter contains the application of the 3D FEM approach described in the previous chapters to an actual annular combustion chamber of an heavy duty gas turbine. The geometry and all the operative conditions are provided by Ansaldo Energia. At the beginning the model is described (geometry, computational grid, operating conditions and boundary conditions). Then the modes of the chamber are evaluated, and for one of these, nonlinear flame model is applied to reproduce bifurcation diagram. In particular, experimental data of combustion instability in Ansaldo machine are not available, and then, with some approximations, experimental FDF obtained by Palies in [45] is considered.

### 6.1 GEOMETRY AND BOUNDARY CONDITIONS

The geometry of the Ansaldo Energia annular combustion chamber is taken from the work carried out by Campa [1]. It is composed by 24 burners placed in annular sector. A quarter of the entire 3D chamber is shown in Fig.6.1. The computational grid is defined in order to have a good mixing between the computational accuracy and a reduction of the required computational efforts (Fig.6.2) [1]. Both the inlet and the outlet boundary conditions are closed walls, like all the other boundaries. Actually the inlet and the outlet zones are not exactly closed walls, since they should be defined by means of acoustic impedances which take into account the flow condition at the exit of the axial compressor (inlet to the plenum) and at the entrance of the turbine (outlet of the combustion chamber). The assumption of closed walls is driven by the difficulty to obtain this kind of information, so that simplified boundary conditions are assumed. In order to reduce the computational efforts (number of processors and RAM used) and the computational time, only one quarter of the entire annular combustion chamber is examined instead of the whole. In acoustics it is possible to detect all the eigenfrequencies of the system only from one quarter, since there are surfaces with nodes and surfaces with the maxima and the minima of the acoustic pressure trend. It is necessary to apply proper periodic boundary conditions and two steps in the computation are carried out [1]. In the first step sound hard boundary conditions are applied to the longitudinal sections (symmetric boundary conditions). In the second step sound hard boundary condition is applied to one longitudinal section and sound soft boundary condition to the other longitudinal section (non-symmetric boundary conditions). In so doing the azimuthal modes are detected once and not twice as happens when an entire circumferential domain is computed. Hence, exploiting the symmetry of the phenomenon, the mode shape of the eigenvalue corresponding to the entire geometry can be obtained from the mode shape of one quarter of the entire geom-

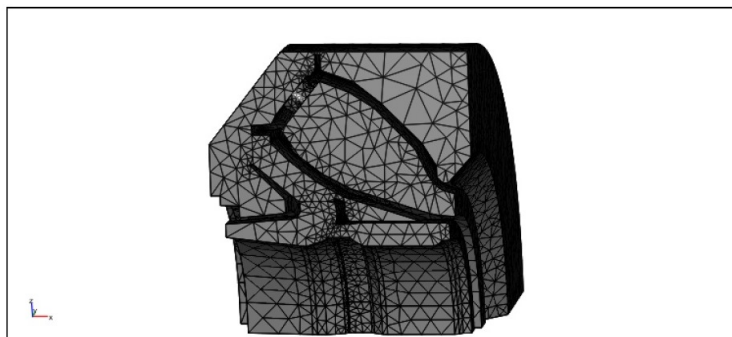


(a)

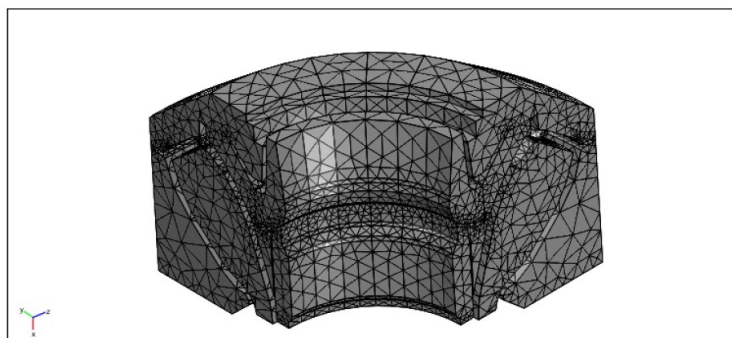


(b)

Figure 6.1: Quarter of the whole combustion chamber in the 3D FEM code: (a) top view, (b) bottom view [1].



(a)



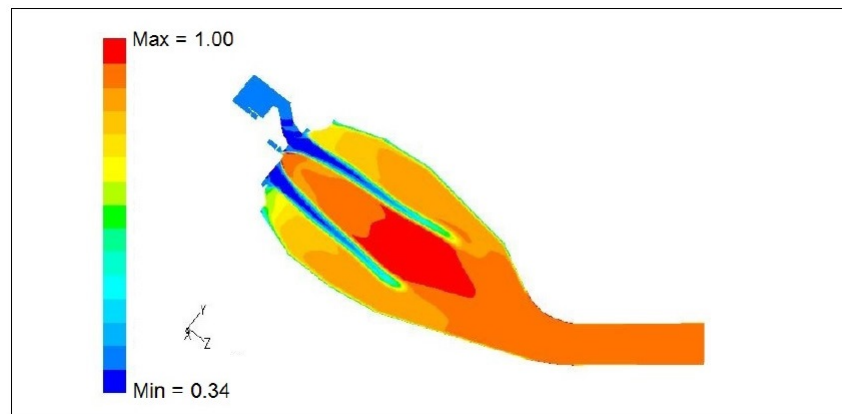
(b)

Figure 6.2: Computational grid of one quarter of the system: (a) top view, (b) bottom view [1].

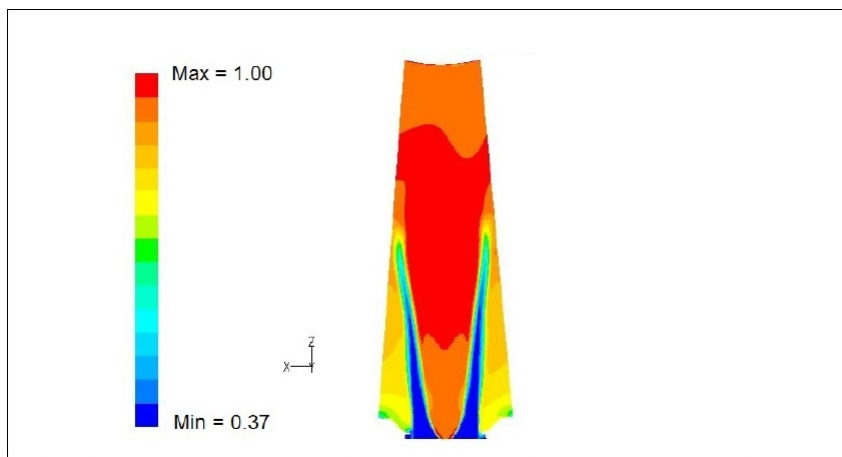
etry. In [1] various tests are performed to evaluate the symmetry influence on the assessment of eigenfrequencies. The results obtained for a quarter of entire geometry are in very good agreement with the ones evaluated with whole configurations, confirming the followed approach.

## 6.2 OPERATIVE CONDITIONS

The operative conditions come from experimental and numerical data provided by Ansaldo Energia. In the plenum uniform operative conditions are assumed. In the combustion chamber the pressure and the temperature varies point by point. One configuration is taken into account and it refers to the condition of maximum load: the temperature field is introduced from the numerical data obtained by means of the fluid dynamic simulations in Fluent, which are shown in Fig.6.3. The



(a)



(b)

**Figure 6.3:** Temperature field in combustion chamber (Fluent data): (a) view of plan parallel to the yz plan, (b) view of plan parallel to the zx plan [1].

maximum values of the temperature are concentrated inside the flame, while the minimum values inside the flame front. Across the flame front there is an abrupt

passage from the lower to the higher values of temperature. The swirl effect is not directly taken into account, but it is evident from the images, as well as the cooling system around the shroud of the combustion chamber.

### 6.3 BURNER TRANSFER MATRIX

Limited domains, such as the conduits of the burners, characterized by a unidimensional propagation of the acoustic wave and by not-negligible levels of the flow velocity, can be treated as compact elements. Additionally, the burners are conduits composed of several details, and their acoustic modeling is very challenging. The burners can thus be modelled by means of specific transfer function matrices, experimentally or numerically obtained through CFD or aeroacoustics codes. The mathematical model of the burners is represented by a system of linear equations, which is the transfer matrix. In this system the unknowns are the fluctuations of acoustic pressure  $p'$  and acoustic velocity  $u'$  at the junctions, or ports of the element. Several tests reported in [1] shows a very good agreement between the results obtained with transfer matrix and those obtained from the original "one-piece" duct. Hence, it is possible to substitute burner with a transfer matrix of a compact element with reduction of the computational efforts. Also, by means of the transfer matrix, it is possible to take into account the effects induced by the Mach number and the loss coefficient. In the following tests the burner is modelled as a transfer matrix obtained by means of experimental data. According to the work of Fanaca and Alemela [46][47], assuming a onedimensional flow and linearizing the conservation equations, it is obtained

$$\left[ A \left( \frac{p'}{\rho c} M + u' \right) \right]_u^d = 0 \quad (6.1)$$

$$\frac{i\omega}{c} u'_u l_{eff} + \left[ M u' + \frac{p'}{\rho c} \right]_u^d + \zeta M_d u'_d = 0 \quad (6.2)$$

In eq.(6.2) the effective length  $l_{eff}$  is a measure of the accelerated mass in the compact element

$$l_{eff} = \int_{x_d}^{x_u} \frac{A_u}{A(x)} dx \quad (6.3)$$

and it takes into account the variation of section between plenum and burner.  $\zeta$  is the acoustical losses and generally closed to the time mean flow loss coefficient. Using effective length  $l_{eff}$  and pressure loss coefficient  $\zeta$ , neglecting higher order Mach number terms, the transfer matrix of a compact element is obtained from eq.(6.1) and eq.(6.2):

$$\begin{bmatrix} \frac{p'}{\rho c} \\ u' \end{bmatrix}_d = \begin{bmatrix} 1 & M_u - \alpha M_d (1 + \zeta) - i K_i l_{eff} \\ \alpha M_u - M_d & \alpha + M_d i K_i l_{eff} \end{bmatrix} \begin{bmatrix} \frac{p'}{\rho c} \\ u' \end{bmatrix}_u \quad (6.4)$$

where  $K_i = \omega/c$  is wave number and  $\alpha = A_u/A_d$  is the area ratio. The surfaces over which the transfer matrix is applied are chosen in order to be representative of the whole system of addition of compressed air and methane inside the combustion chamber. Hence the inlet surface is the inlet to the burner system from the plenum and the outlet surface is the entrance to the combustion chamber, Fig.6.4. In this system the transfer matrix substitutes the cylindrical computational domain

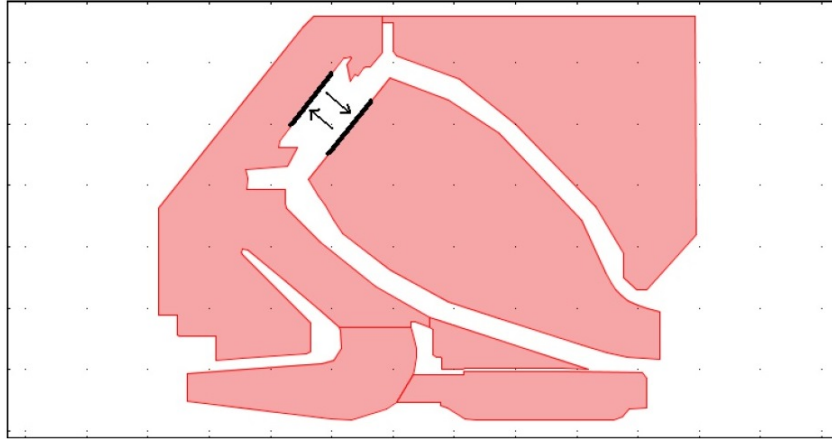


Figure 6.4: Model of the burner transfer matrix with the inlet and outlet surfaces [1].

modelling the burner. As a consequence,  $\alpha = 1$ , the Mach number is constant and the effective length is equal to the length of the substituted element. The terms characterizing the burner transfer matrix come from experimental data on the diagonal burner and concerns the pressure gradient, the density, the velocity, the temperature and the pressure.

## 6.4 LINEAR ANALYSIS

### 6.4.1 Results without unsteady heat release

First the modes of the actual annular combustion chamber are detected without unsteady heat release. The complex eigenfrequencies have a nonzero imaginary part because the model is composed of acoustic impedance conditions related to the transfer matrix. Hence it is possible to detect the growth rate of the oscillations for every mode even if the source term is absent. The first modes until 250 Hz are searched for and they are listed in Tab.6.1, where an indication about their modeshape is provided. In particular modes named with "AX" refer to pure axial modes, the "AZ" are azimuthal modes, while "M" represent the azimuthal-axial mode shape. The frequencies are normalized against the first eigenfrequency. Fig.6.5 shows frequencies and growth rates of the modes, highlighting the stability of each mode, as expected.

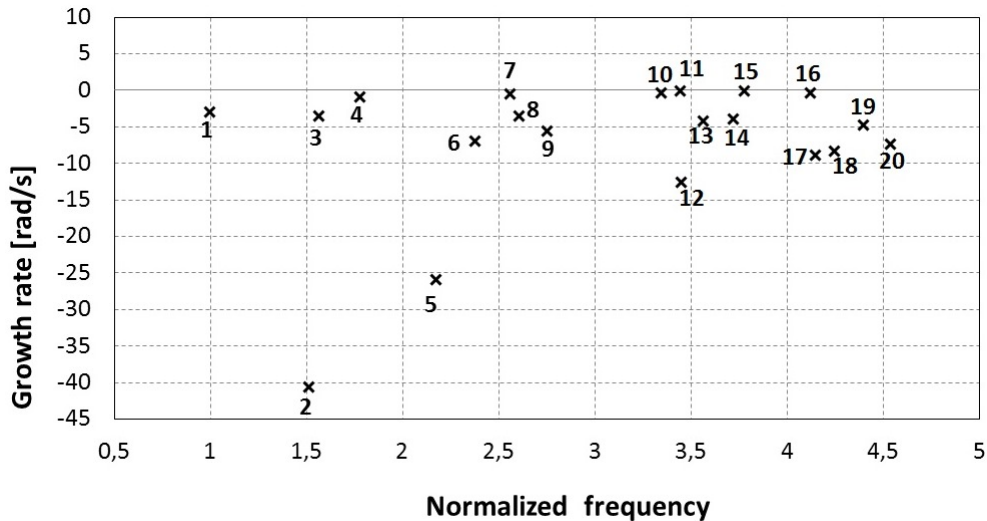


Figure 6.5: Frequencies and growth rates of the modes regarding the actual annular combustion chamber without unsteady heat release.

### 6.4.2 Results with unsteady heat release

To reproduce the flame and the heat release which occur in real machine, numerical data from RANS simulation are inserted in the FEM code. In particular, the eigenvalue problem is solved with the actual temperatures into the combustion chamber, defining as well as possible the flame shape. In Fig.6.3 the temperature field inside the combustor is reported, while Fig.6.6 shows the *Rate of Reaction* data from the fluid-dynamic simulations in Ansys Fluent. *Rate of Reaction* is defined as the rate of reaction of the consumption of methane in a two step reaction between methane and air, and it is used to describe the flame front. Volumetric heat release fluctuations  $q'$  are modelled by means of the following procedure:

**Table 6.1:** List of the first modes until 250 Hz. Frequencies are normalized against the first eigen-frequency.

Number	Name	Frequency	Node	zone
1	AX <sub>1</sub>	1	1	plenum
2	AX <sub>2</sub>	1.52	2	plenum
3	AX <sub>3</sub>	1.57	1	plenum
4	AZ <sub>1</sub>	1.78	1	plenum
5	AX <sub>4</sub>	2.18	2	plenum
6	AX <sub>5</sub>	2.38	1	plenum
7	AZ <sub>2</sub>	2.56	1	plenum
8	M <sub>1</sub>	2.61	ax1-az1	plenum & chamber
9	AX <sub>6</sub>	2.76	2	plenum
10	AZ <sub>3</sub>	3.35	2	plenum
11	AX <sub>7</sub>	3.45	1	plenum
12	M <sub>2</sub>	3.46	ax2-az1	plenum & chamber
13	M <sub>3</sub>	3.57	ax1-az1	plenum & chamber
14	M <sub>4</sub>	3.72	ax1-az1	plenum & chamber
15	AX <sub>8</sub>	3.78	1	plenum
16	AZ <sub>4</sub>	4.13	2	plenum
17	AX <sub>9</sub>	4.15	2	plenum
18	AX <sub>10</sub>	4.25	2	plenum
19	M <sub>5</sub>	4.40	ax1-az2	plenum & chamber
20	M <sub>6</sub>	4.54	ax3-az1	plenum & chamber

1.  $\bar{q} = 0$  and  $\hat{q} = 0$  when *Rate of Reaction* is lower than an inferior limit, which is properly defined;
2. in the other points  $\bar{q}$  (volumetric heat release W/m<sup>3</sup>) is calculated considering the Lower Heating Value (J/kmol).

Heat release law is obtained from the following model:

$$\frac{q'(x)}{\bar{q}(x)} = -k \frac{u_i'(t - \tau(x))}{\bar{u}_i} \quad (6.5)$$

where  $q$  is the volumetric heat release,  $\bar{q}$  is its mean value, subscript  $i$  corresponds to the position at which acoustic velocity inside heat release law is referred. In this scheme this position corresponds to the combustion chamber inlet, which is also the burner transfer matrix interface. Heat release is expressed as

$$\bar{q} = RR(x) \cdot h_f, \quad (6.6)$$

where  $RR$  represents the spatial distribution of *Rate of Reaction* [kmol/m<sup>3</sup>s],  $h_f$  is the Lower Heating Value [J/kmol] of the fuel. *Rate of Reaction* decays to zero value outside the flame and then flame front is correctly reproduced. The volumetric heat release model defined in eq.(6.6) is transferred into the governing equation. Time delay is defined with a spatial distribution along the flame front through a

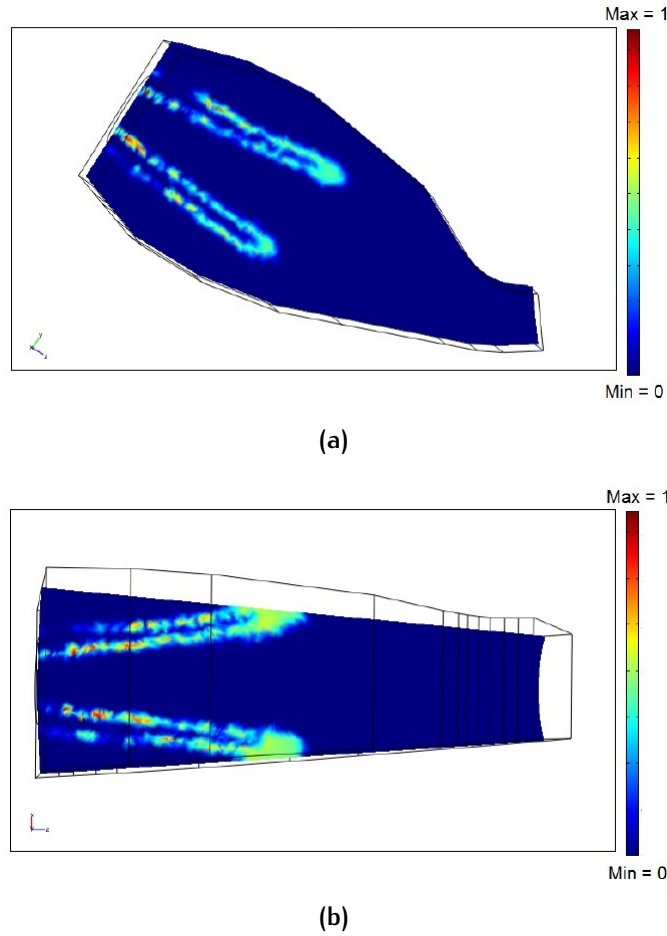


**Figure 6.6:** *Reaction Rate* from RANS simulation. : (a) view of chamber, (b) view along one sector axis. The values are normalized against the maximum Reaction Rate. [1].

function of position  $\tau(x)$ . The procedure to detect this distribution is roughly the same proposed by Krebs et al.[48] and called "flight time" method by Giaque et al. [49]. Using the CFD analysis, time for a particle to go from the burner exit to the flame front is calculated. The spatial distribution for  $\tau$  is obtained by means of a high number of particles[1][50]. Fig.6.7 shows the time delay distribution inside the combustion chamber as taken from the RANS simulations. The time delay is plotted only in the areas where the values of heat release are significant [1].

Applying the flame model in (6.5) the eigenvalues of the machine are evaluated. In Fig.6.8 is reported a comparison between eigenvalues obtained with linear flame model and the ones evaluated without unsteady heat release. Results show that if heat release is considered, variation of the frequency and the growth rate occur. In particular, limited alteration of the eigenfrequency is evaluated, while there are some modes with a large change in the value of growth rate. As a general result, applying the linear flame model a less stable condition occurs. For most of all modes, variation from negative to positive growth rate is expected, with an alteration of the stability condition.

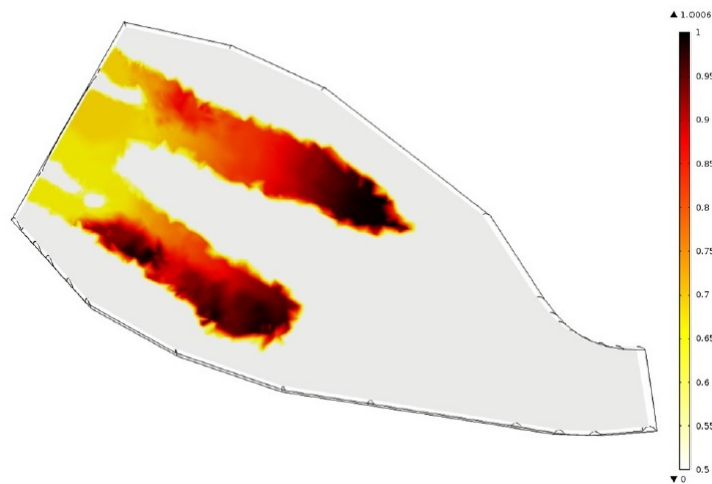


Figure 6.7: Time delay from RANS simulation in the 3D FEM code. The values are normalized against the maximum value [50].

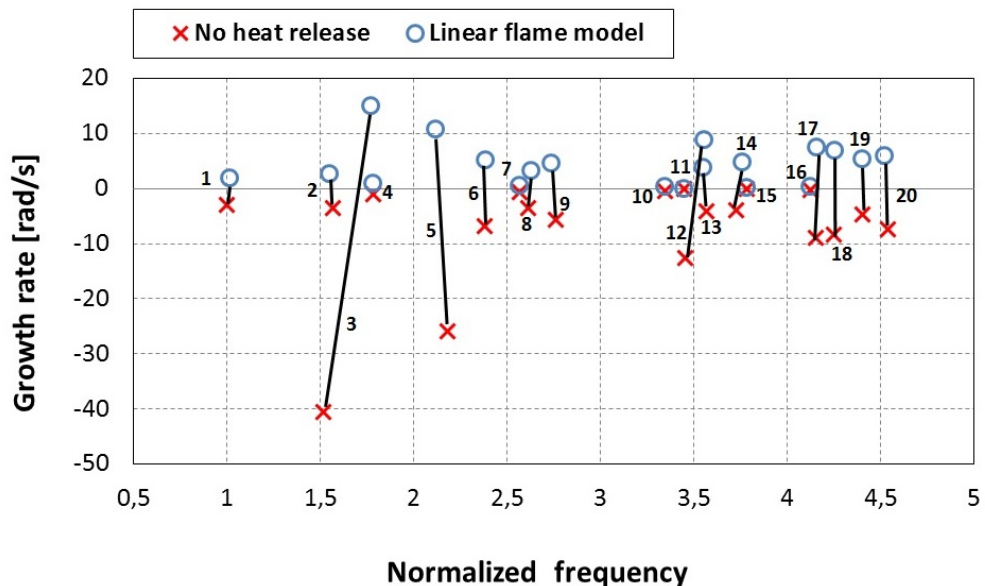


Figure 6.8: Comparison between eigenvalues of machine obtained with linear flame model and the ones evaluated without unsteady heat release.

### Time delay influence

To evaluate the time delay influence on stability of the system,  $\tau$  value must be regarded as a constant. The assumption of a constant time delay could be justified by work of Campa [1] which evaluates the range of interest for machine configuration. In particular, time delay is assumed between 5 to 8 ms. The study of time delay influence is performed on mode 12 of Tab.6.1. It is the first azimuthal mode in combustion chamber and it is one of the most dangerous which occur in real machine. Fig.6.9 shows the mode considered for the study. Time delay influence is evaluated setting interaction index of heat release  $k=1$  and varying  $\tau$

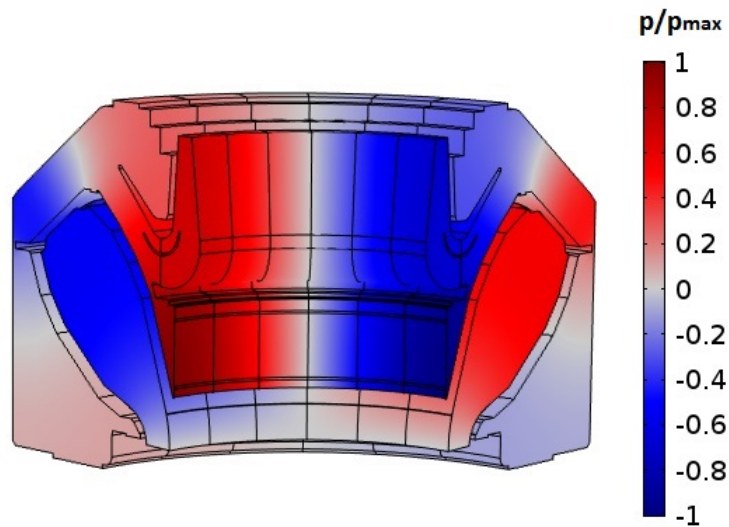


Figure 6.9: First azimuthal mode in combustion chamber.

from 3 to 8 ms. Results are reported in Fig.6.10. As time delay increases, the frequency of the mode drops, while growth rate oscillates between positive and negative values. In particular, in the range of interest between 5 to 8 ms, system evolves from unstable to stable conditions. For time delay higher than about 6.5 ms less stable conditions occur up to  $\tau = 7.4$  ms which brings back the system to unstable condition. This confirms that time delay is an important parameter on stability, and then it must be evaluated with high accuracy.

#### *Interaction index influence*

To complete linear analysis of the studied acoustic mode, influence of interaction index  $k$  is evaluated. In particular time delay is set equal to 5 ms, while  $k$  is varied from 0.4 to 1.8. Results are reported in Fig.6.11. As  $k$  increases, nonlinear decreasing behaviour of frequency is obtained. The system moves from stable to unstable conditions with monotone growing trend of growth rate. In fact, as  $k$  increases higher value of heat release is considered with reduction of stability conditions. Hence, the growth rate moves from negative to positive values, while frequency drops. However the effect of interaction index on frequency is very low. This behaviour of the system demonstrates the importance to consider the correct heat release interaction index and how the mode is modified by changing in the load.

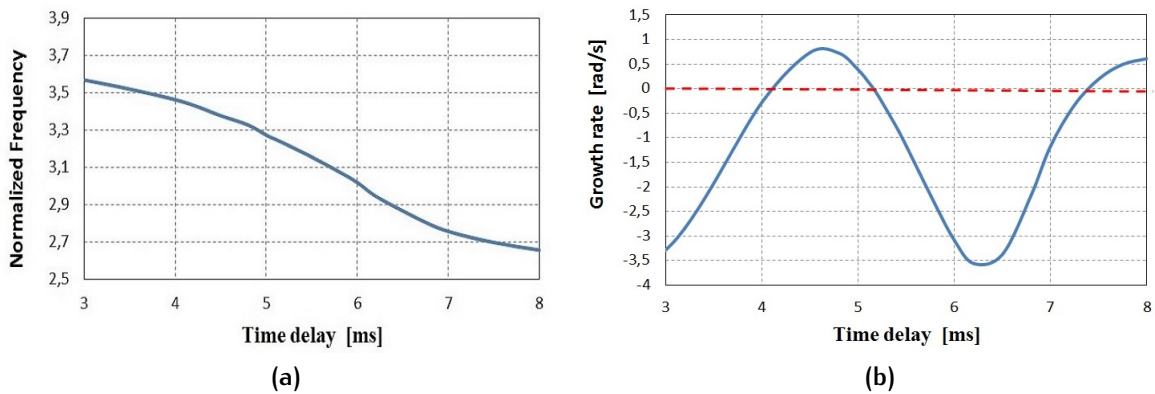


Figure 6.10: Influence of time delay on the first azimuthal mode in combustion chamber: (a) frequency dependence, (b) growth rate dependence.

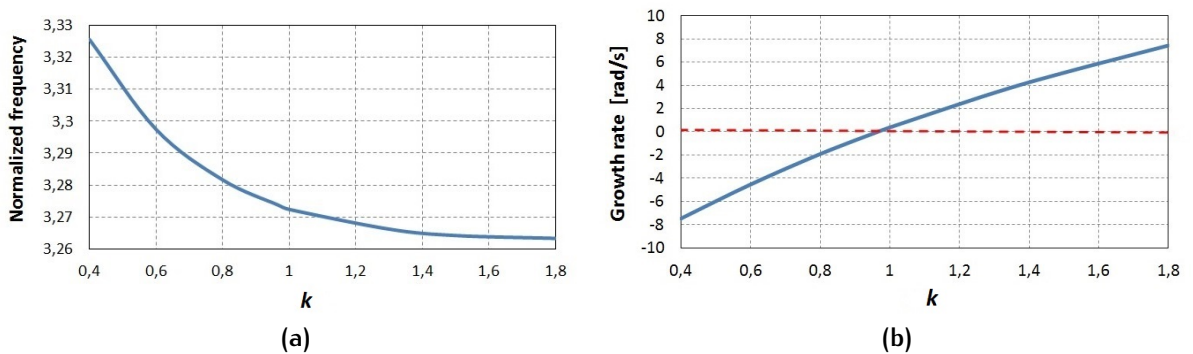


Figure 6.11: Influence of interaction index on the first azimuthal mode in combustion chamber: (a) frequency dependence, (b) growth rate dependence.

## 6.5 NONLINEAR FLAME MODEL

As reported in the previous chapter, a non linear analysis is very important in studying the thermoacoustic instability. To obtain the limit cycle and the bifurcation diagrams of Ansaldo machine, nonlinear flame model is applied. First the polynomial flame model previously applied to simplified geometry is considered. Then, experimental FDF obtained by Palies is set to evaluate the qualitative behaviour of bifurcation diagram and the influence of parameter on stability of combustor .

### 6.5.1 Test case from the literature

In order to evaluate the nonlinear heat release effect in real machine, polynomial flame model tested before in simplified geometry is applied. In particular, quadratic polynomial of eq.(5.2) is considered with  $\mu_2 = 1$  and  $\mu_0 = 0.2$ .  $\tau$  is set constant and equal to 5 ms. Results are shown in Fig.6.12 and they confirm the behaviour of bifurcation diagram obtained with the same flame model in Rijke tube. As can be predict from weakly nonlinear analysis subcritical bifurcation occurs with Hopf point in  $k = 4.82$ .

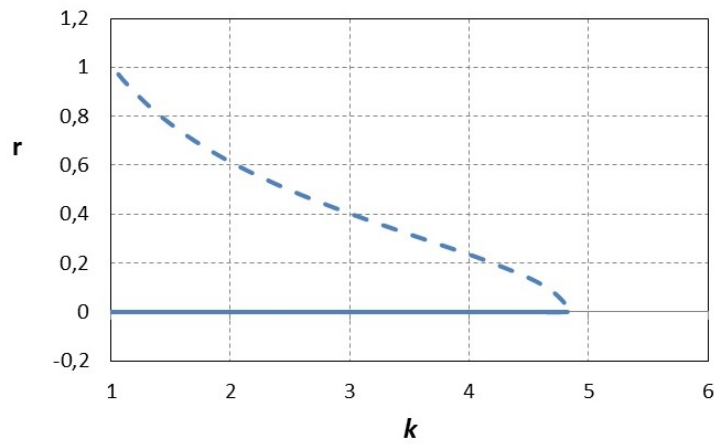


Figure 6.12: Bifurcation diagram for machine configuration with flame model of eq.(5.2),  $\mu_2 = 1$  and  $\mu_0 = 0.2$ .

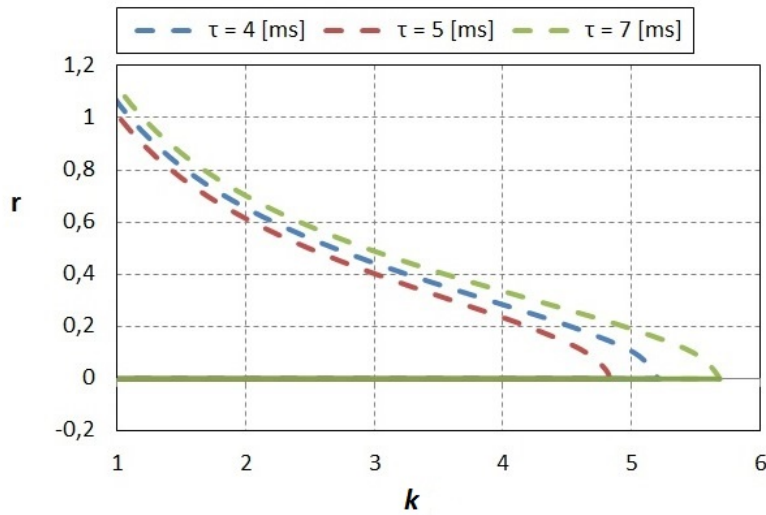


Figure 6.13: Influence of time delay of flame model in eq.(5.2) on stability of machine combustor.

For this flame model, with reference to [fifth chapter](#), the influence of time delay and damping coefficient is evaluated. In particular, three cases with  $\tau = 5$  ms,  $\tau_1 = 4$  ms and  $\tau_2 = 7$  ms are considered. For each value of time delay varying the interaction index  $k$  zero growth rate condition is searched for and bifurcation diagram is obtained. Results are reported in Fig.6.13. As obtained for Rijke tube configuration in Fig.5.3, the influence of the time delay is on the position of the Hopf point. It can be seen that a rise of time delay does not involve a monotone increase or reduction of stability range. In fact, for  $\tau_1$  the Hopf point moves at  $k = 5.2$  while for  $\tau_2$  it occurs at  $k = 5.69$ . This trend is due to the oscillatory behaviour of growth rate evaluated in linear analysis.

The influence of damping is analyzed considering eq.(5.9). Damping coefficient is varied in a range between 0 to 0.07, and for each value of this, flame model of eq.(5.2) is applied and bifurcation diagram is tracked. Once again the same trend observed for Rijke tube in Fig.5.12 is obtained. The presence of damping increases

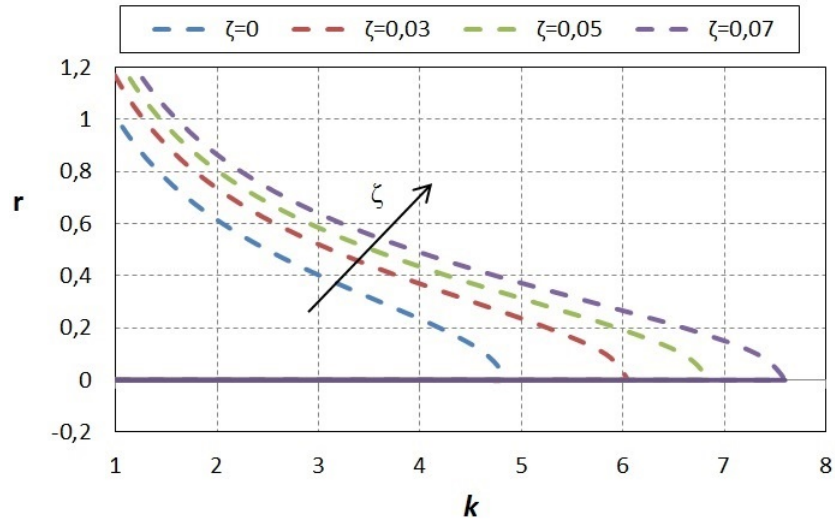


Figure 6.14: Influence of damping coefficient on stability of machine combustor.

the stability range of combustion, proportionally to the value of  $\zeta$ .

Applying the same flame model to Rijke tube and machine configuration, the same behaviour of bifurcation diagram is evaluated. Also, an alteration of parameters of the system leads to the same change in stability conditions. This confirms that the kind of bifurcation depends on the nonlinear flame model, independently of the geometrical configuration examined, following the predictions of the weakly nonlinear analysis. Hence, qualitative nonlinear analysis can be performed in order to obtain informations about the flame model. In this way, in presence of experimental measurements in real machine, numerical model can be calibrated in order to predict combustion instability.

### 6.5.2 Experimental flame model

At the moment in Ansaldo Energia experimental data about thermoacoustic instability of AE94.3A machine are not available. Hence, qualitative analysis is performed applying the experimental FDF obtained by Palies in [44]. This approximation can be carried out considering that both combustors operate with swirl premixed combustion. Also, on the literature several FDF similar to the one measured by Palies are reported. In particular in most of these, the gain presents two peaks at different frequencies and then it decays to zero as frequency increases. So, at first FDF of Palies is used as benchmark while in next step sensitivity analysis on the FTF shape is carried out.

To apply experimental FDF on the machine configuration, it must be considered that the acoustic mode of machine tested occurs at different frequency compared to the one studied in Palies test rig. Hence, the FDF must be scaled in order to lead the second peak of gain in a frequency range of the considered mode. Fig.6.15 shows the scaled FDF obtained for relation in eqs.(6.7),(6.8) and (6.9). The influence

of amplitude on *NFTF* is maintained equal to the one evaluated from the measurements by Palies in eq.(5.24).

$$G_{FDF} = \begin{cases} 0.7 + \xi_1 \left(\frac{u'}{u}\right) \cdot \cos\left(\left(\frac{f}{8\pi}\right) - \varphi\right) & \text{if } f/f_0 < 3.27 \\ 10^7 \xi_2 \left(\frac{u'}{u}\right) \cdot e^{-0.015f} & \text{if } f/f_0 \geq 3.27. \end{cases} \quad (6.7)$$

$$\xi_1 = 0.85 - 0.7 \left(\frac{u'}{u}\right) \quad (6.8)$$

$$\xi_2 = 21,185 - 8.872 \left(\frac{u'}{u}\right) \quad (6.9)$$

Hence, the same relation used in previous analyses is considered for  $\xi_1$ , while relation of (6.9) is applied to  $\xi_2$  to guarantee correct piecewise function. Also, the same calibration coefficients evaluated for two different configurations of Palies test rig are considered. One test is performed with the calibration coefficients reported in eqs.(5.31), (5.26) while further test considers relations in eqs.(5.32) and (5.28). The nonlinear analysis is conducted on the mode 12 of Tab.6.1 applying the nonlinear flame model in eq.(6.10). Time delay is set equal to 5 ms. This value is the same evaluated for the test rig of Palies, and then less approximation on calibration coefficients can be considered. Also, time delay is in good agreement with results from RANS simulation.

$$\frac{\hat{q}}{\bar{q}} = k \text{NFTF} \left(\frac{\hat{u}}{\bar{u}}\right) \cdot \frac{\hat{u}}{\bar{u}} e^{i\omega\tau} \quad (6.10)$$

Results are reported in Fig.6.16. The behaviour of bifurcation diagrams obtained for calibration coefficients relative to two different configurations of Palies test rig is similar. In particular supercritical bifurcation occurs with the Hopf points at  $k=0.49$  and  $k=1.65$  but the same trend is expected. Then, only calibration coefficients of eqs.(5.31), (5.26), relative to "medium" configuration of Palies test rig, is considered for the next simulations.

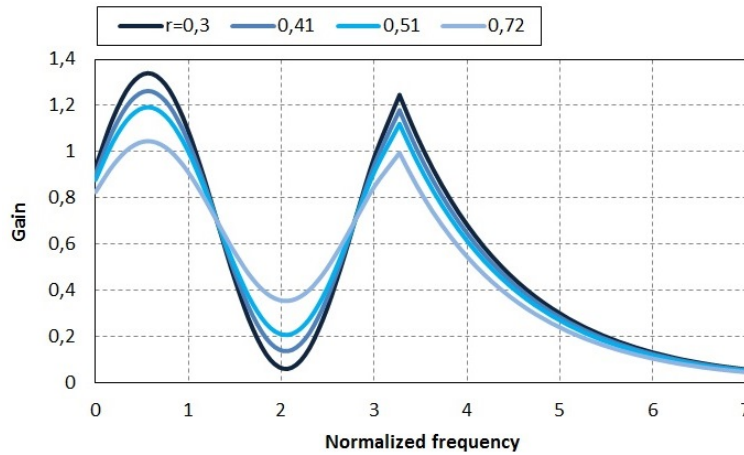
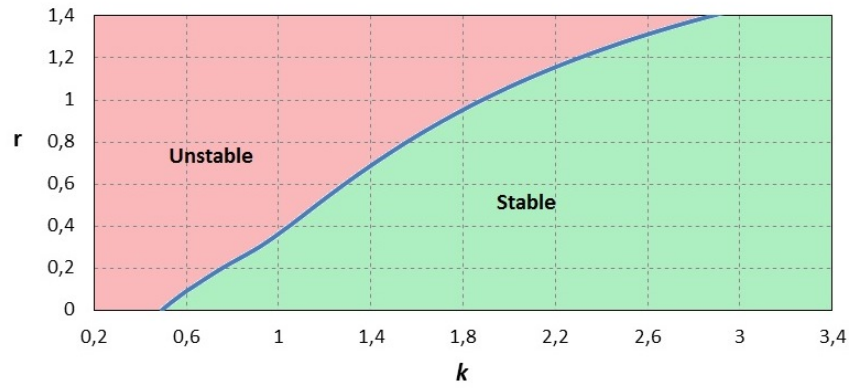
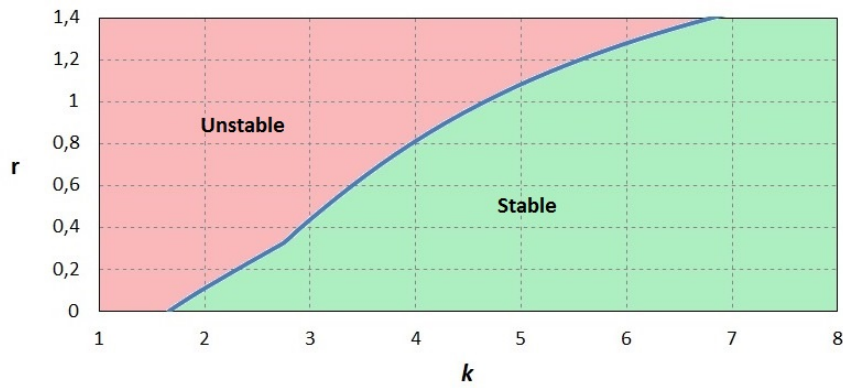


Figure 6.15: FDF obtained by Palies scaled on frequency of Ansaldo machine mode.



(a)



(b)

**Figure 6.16:** Bifurcation diagram of real machine evaluated with experimental flame model of eq.(5.21): (a) calibration coefficients of eqs.(5.31) and (5.26), (b) calibration coefficients of eqs.(5.32) and (5.28).

### Sensitivity analysis

In order to evaluate the effects of different FDFs on stability conditions of machine, several tests are performed varying the shape of the FDF. The gain is approximated with three piecewise functions to vary the value and the position of the second peak of gain. The expressions used are reported in eq.(6.11) where  $\xi_1$ ,  $\xi_2$ ,  $\xi_3$ ,  $v_1$  and  $v_2$  are coefficients set in such a way to obtain the required shape.

$$G_{FDF} = \begin{cases} 0.7 + \xi_1 \left(\frac{u'}{u}\right) \cdot \cos\left(\left(\frac{f}{v_1\pi}\right) - 1, 2\right) & \text{if } f/f_0 < 2.7 \\ 0.7 + \xi_2 \left(\frac{u'}{u}\right) \cdot \cos\left(\left(\frac{f}{v_2\pi}\right) - 1, 2\right) & \text{if } 2.7 \leq f/f_0 < 3.27 \\ \xi_2 \left(\frac{u'}{u}\right) \cdot e^{-0.015f} & \text{if } f/f_0 \geq 3.27. \end{cases} \quad (6.11)$$

The FDF is obtained considering  $\xi_1$ ,  $\xi_2$ ,  $\xi_3$  with dependence to the amplitude. In particular the parametric analysis of the gain is carried out on curve relative to  $r=0.3$  and it is extended to the other amplitudes considering the eq.(6.8) for  $\xi_1$  and  $\xi_2$ , maintaining the same linear dependence of eq.(6.9) for  $\xi_3$ . At first, the value of the gain at second peak is varied (Fig.6.17). The peak is maintained at the frequency of the mode studied and gain value is varied from 0.8 to 1.4. Considering the flame

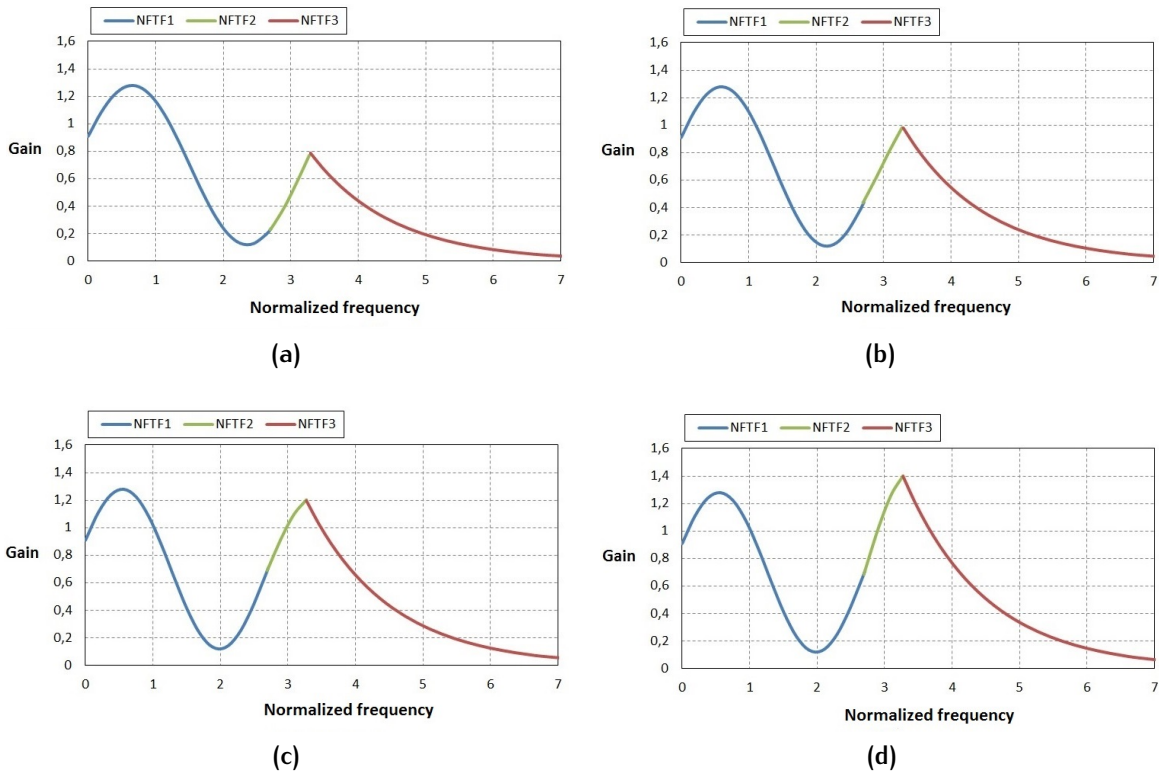


Figure 6.17: FDF with second peak at normalized frequency equal to 3.27 : (a) gain=0.8, (b) gain=1, (c) gain=1.2, (d) gain=1.4.

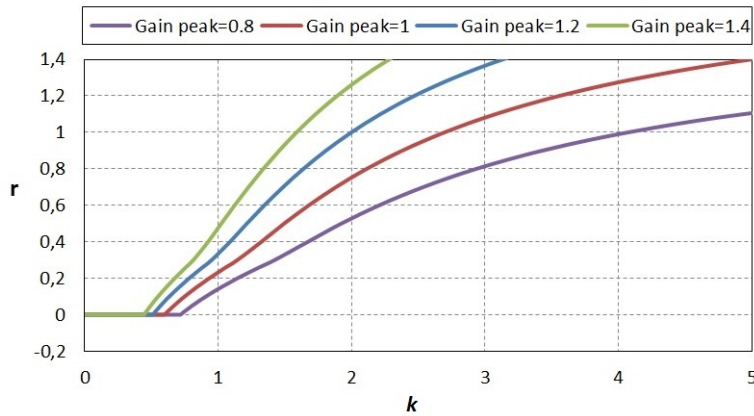


Figure 6.18: Influence of the second peak gain of FDF on bifurcation diagram.

model in eq.(5.20) and eq.(6.10), with calibration coefficient in eqs.(5.31) and (5.26), bifurcation diagram of the system are obtained. Time delay is set constant and equal to 5 ms. Results are reported in Fig.6.18. As can be expected, reducing the gain peak of FDF, unstable conditions occur at higher value of interaction index  $k$ . In particular the Hopf point moves from  $k=0.84$  to  $k=0.52$  with nonlinear behaviour. Also, at constant interaction index, as gain increases the amplitudes reached by system grow. In fact, the gain of FDF is related to the heat release in combustion chamber, and as it increases less stable combustion conditions occur.

The last analysis is performed considering the peak of gain at three different frequencies. In particular, the gain value is set equal to 1.2 and the peak is moved at normalized frequencies equal to 2.9, 3 and 3.27. Fig.6.19 shows the FDF for the considered cases. For each case, applying the flame model used before, stability conditions of the system are evaluated. Results are reported in Fig.6.20.

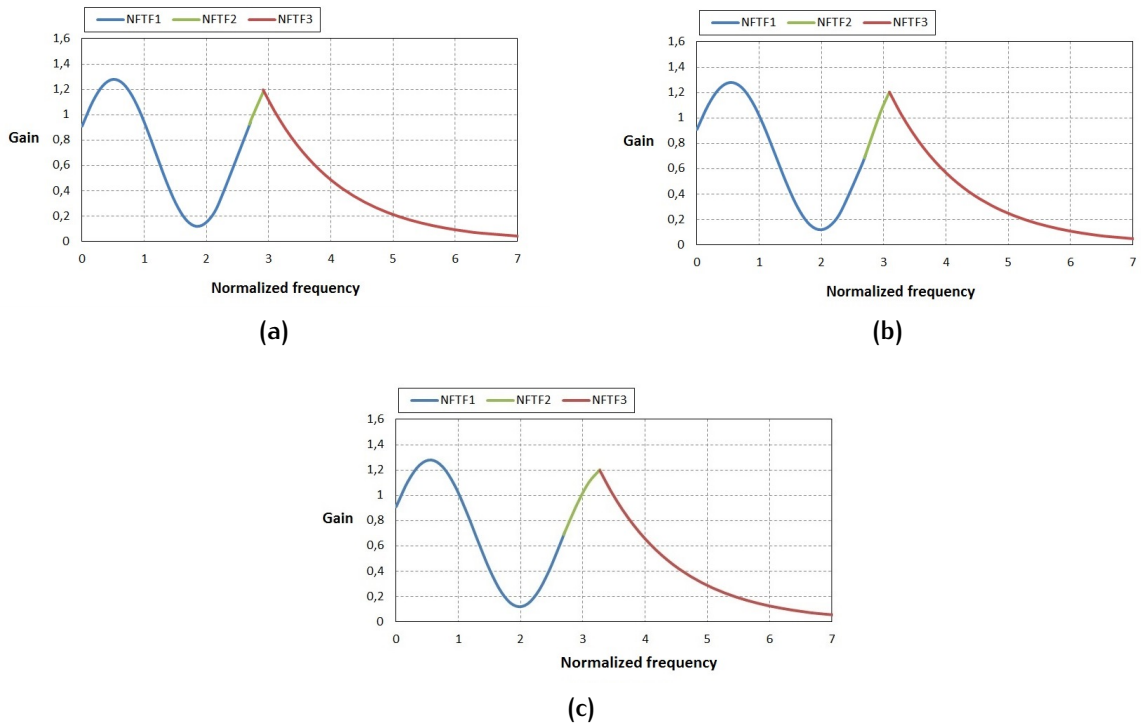


Figure 6.19: FDF with second peak gain of 1.2 : (a) second peak at 2.9, (b) second peak at 3, (c) second peak at 3.27.

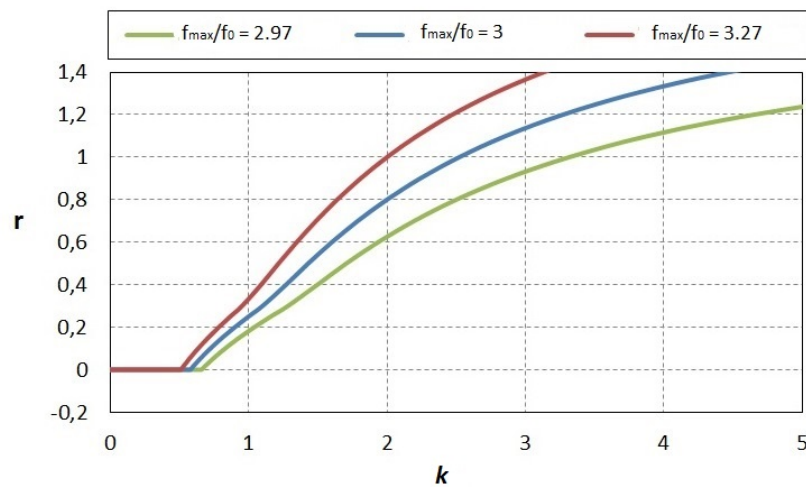


Figure 6.20: Influence of the second peak position on bifurcation diagram.

The same supercritical behaviour of bifurcation diagram is expected with variation in Hopf point and in amplitude reached by the system. As the frequency of the peak decreases, the gain of FDF at the frequency of the mode drops. In particular, as peak is shifted, the gain moves from 1.2 to 0.88. This causes a lower heat release promoting the stability of the system. Hence, as Fig.6.20 shows, the Hopf point moves at higher values of  $k$  and system reaches a lower amplitude. Previous results show that as the shape of FDF varies, stability conditions of the system change. However similar behaviour of bifurcation diagram is expected, and even if some hypotheses are carried out to consider experimental FDF of another test rig, qualitative influence of different parameters are evaluated.

---

## CONCLUSION

---

The work described in the previous chapters has brought to the confirmation of the methodology used for the analysis of the thermoacoustic combustion instabilities in Ansaldo Energia. A 3D FEM commercial software is used for the solution of the acoustic equations. Elements from the traditional tools (low order models and CFD models) are introduced inside this tool in order to have a better comprehension of the whole physical phenomenon.

The importance of the non linearity in the instability analysis has been examined, and several nonlinear flame model are considered in order to obtain bifurcation diagram of the system. In the first part of this work several nonlinear flame models are applied on simplified geometry to evaluate the influence of the main flame parameters over the complex eigenfrequency. In particular has been fund that:

- the influence of the time delay and the damping is only on the position of Hopf point and fold point;
- the amplitude of the limit cycle solution and the amplitude of the oscillations at the fold point are not influenced by variations of the time delay or the damping;
- the frequency of the mode changes only in linear conditions, whereas remains constant when the nonlinear solution occurs.

A new method to track bifurcation diagram is found. For a particular nonlinear flame model this new approach permits to evaluate stability conditions of the system starting from the Hopf point. This can significantly reduce the time to obtain bifurcation diagram.

The second part of the work confirms the possibility to use Comsol for solving the Helmholtz equation with nonlinear flame models. However, experimental data on stability of the system are required for calibration of the flame model. Since the experimental measure of combustion instability on AE94.3A machine are not available, qualitative nonlinear analysis is carried out considering the experimental FDF obtained from a simplified premix swirl combustor. This analysis has brought to very good results which must be confirmed by experimental measurements.



---

## BIBLIOGRAPHY

---

- [1] G. CAMPA, *Prediction of the thermoacoustic combustion instability in gas turbines*, PhD thesis, Politecnico di Bari, 2012.
- [2] K. ALNE, *Reduction of NOx Emissions from the Gas Turbines for Skarv Idun*, Master of Science in Energy and Environment, Norwegian University of Science and Technology, 2007.
- [3] DW. BAHR, *Aircraft turbine engine NOx emission abatement*, Chapter 10, In: Culick FEC, Heitor MV, Whitelaw JH, editors. *Unsteady combustion*, The Netherlands: Kluwer Academic Publisher, 1996.
- [4] SM. CORREA, *A review of NOx formation under gas-turbine combustion*, *Combustion Science and Technology*, 1992.
- [5] AH. LEFEBVRE, *The role of fuel preparation in low-emission combustion*, *Journal of Engineering for Gas Turbines and Power*, 1995, pp.117-617.
- [6] SM CORREA, *Power generation and aero-propulsion gas turbines: from combustion science to combustion technology*, *Proceedings of the Combustion Institute*, 1998.
- [7] J.ZELDOVICH, *The oxidation of nitrogen in combustion and explosions*, *Acta Physicochimica*, 1946, pp. 577-628.
- [8] CJ.GOY, SR.JAMES and S.REA, *Combustion instabilities in gas turbine engines: operational experience, fundamental mechanisms, and modeling*, Lieuwen T, Yang V, editors, *Progress in Astronautics and Aeronautics*, Chapter 8, 2005.
- [9] FE. ZUKOSKI, Chapter 21, *The aerothermodynamics of aircraft gas turbine engines*, Air Force Aero Propulsion Laboratory, 1978, AFAPL-TR-78-52.
- [10] T. LIEUWEN, H. TORRES, C. JOHNSON and BT. ZINN, *A mechanism of combustion instability in lean premixed gas turbine combustors*, Schools of Aerospace and Mechanical Engineering, Georgia Institute of technology, Atlanta 2001.
- [11] Y.HUANG, V.YANG, *Dynamics and Stability of Lean-Premixed Swirl-Stabilized Combustion*, *Progress in Energy and Combustion Science*, 2009, pp.293-364.
- [12] FEC CULICK, *Unsteady Motions in Combustion Chambers for Propulsion Systems*, AGARD, AG-AVT-039 2006.

- [13] J.P. HATOUT, *Thermoacoustic Instability, Fundamentals and Modeling in Combustion*, 1999.
- [14] J.W.S. RAYLEIGH, *The Explanation of Certain Acoustical Phenomena*, *Nature*, 18, pp. 319-321, 1878.
- [15] J.W.S. RAYLEIGH, *The Theory of Sound*, Vol. 2, Dover, 1896.
- [16] K.T. FELDMAN, *Review of the literature on Sondhauss thermoacoustic phenomena*, *J. Sound Vib.* 7, 71-82 and 83-89 (1968)
- [17] W. POLIFKE, *Combustion Instabilities*, Von Kármán Institute Lecture Series, March 2004.
- [18] FEC. CULICK, *Dynamics of combustion systems, fundamental, acoustics and control*, Active control of engine dynamics. Von Kármán Institute for Fluid Dynamics, May 14-18, 2001, Lecture Series.
- [19] A.P. DOWLING and S.R. STOW, *Acoustic Analysis of Gas Turbine Com-bustors*, *Journal of Propulsion and Power*, 19 (5), pp.751-765, 2003.
- [20] L. CROCCO and SI.CHENG, *Theory of combustion instability in liquid propellant rocket motors*, London: Butterworths Scientific Publications; 1956, AGARDograph No.8.
- [21] FEC. CULICK, *Combustion instabilities in liquid-fueled propulsion systems - an overview*, AGARD Conference Proceedings 450. Belgium: NATO ASI Series Publication Coordination Office, 1989.
- [22] C. JAHNKE and F. CULICK, *Application of dynamical systems theory to nonlinear combustion instabilities*, *Journal of Propulsion and Power* 1994;10:508-517.
- [23] N. ANANTHKRISHNAN, S. DEO, F. CULICK, *Reduced-Order Modeling and Dynamics of Nonlinear Acoustic Waves in a Combustion Chamber*, *Combustion Science and Technology* 2005;177:1-27.
- [24] S. STROGATZ, *Nonlinear Dynamics and Chaos*, Westview Press,2001.
- [25] CE. MITCHELL and L. CROCCO, WA. SIRIGNANO, *Nonlinear Longitudinal Instability in Rocket Motors with Concentrated Combustion*, *Combustion Science and Technology* 1969;1:35-64.
- [26] MP. JUNIPER, *Triggering in Thermoacoustics*, 50th AIAA Aerospace Sciences Meeting 2012.
- [27] MP. JUNIPER, *Triggering in the Horizontal Rijke Tube: Non-normality, transient growth and bypass transition*, *Journal of Fluid Mechanics* 2011;667:272-308.
- [28] K. BALASUBAMANIAN, RI. SUJITH, *Thermoacoustic Instability in a Rijke Tube: Nonnormality and Nonlinearity*, *Physics of Fluids* 2008.

- [29] FEC. CULICK, *Nonlinear Growth and Limiting Amplitude of Acoustic Oscillations in Combustion Chamber*, Combustion Science and Technology 1971;3:1-16.
- [30] ME. LORES and BT.ZINN, *Nonlinear Longitudinal Combustion Instability in Rocket Motors*, Combustion Science and Technology 1973;7:245-256.
- [31] J. WICKER, W. GREENE, SI. KIM, V. YANG, *Triggering in Longitudinal Combustion Instabilities in Rocket Motors: Nonlinear Combustion Response*, Journal of Propulsion and Power 1996;12(6):1148-1158.
- [32] FEC. CULICK, *Nonlinear Behavior of Acoustic Waves in Combustion Chambers*, Acta Astronautica 1976;3:715-734, 735-757.
- [33] E. AWAD and FEC. CULICK, *On the Existence and Stability of Limit Cycles for Longitudinal Acoustic Modes in a Combustion Chamber*, Combustion Science and Technology 1986;46(3):195-222.
- [34] LG. PAPARIZOS and FEC. CULICK, *The Two-Mode Approximation to Nonlinear Acoustics in Combustion Chambers I. Exact Solutions for Second Order Acoustics*, Combustion Science and Technology 1989;65(1):39-65.
- [35] V. YANG and FEC. CULICK, *On the Existence and Stability of Limit Cycles for Transverse Acoustic Oscillations in a Cylindrical Combustion Chamber. 1: Standing Modes*, Combustion Science and Technology 1990;72(1):37-65.
- [36] V. YANG and SI. KIM, *Triggering of Longitudinal Pressure Oscillations in Combustion Chambers. I: Nonlinear Gas Dynamics*, Combustion Science and Technology 1990;72(4):183-214.
- [37] S. STOW and A. DOWLING, *A time-domain network model for nonlinear termoacoustic oscillations*, ASME paper, GT2008-50770 2008.
- [38] M. CINQUEPALMI, *Study of the termoacoustic combustion instability with nonlinear flame models*, Master thesis, Politecnico di Bari, 2012.
- [39] N. NOIRAY, M. BOTHIEN and B. SCHUERMANS, *Investigation of azimuthal staging concepts in annular gas turbines*, University of Cambridge, 2008.
- [40] M.P. JUNIPER, *Triggering in the horizontal Rijke tube: non-normality, transient growth and bypass transition*, J.Fluid Mech.,(2011), vol 667, pp.272-308.
- [41] N.NOIRAY, D.DUROX, T.SCHULLER and S.CANDEL, *New perspective on the flame describing function of a matrix flame*, Journal of Fluid Mechanics 2008.

- [42] M. HECKL, *A unified framework for nonlinear combustion instability analysis based on the flame describing function*, International journal of spray and combustion dynamics Volume 7, Number 2, pages 91-112, 2015.
- [43] M. HECKL, *Analytical model of nonlinear thermo-acoustic effects in a matrix burner*, Journal of Sound and Vibration 332 (2013).
- [44] P. PALIES, D. DUROX, T. SCHULLER and S. CANDEL, *The combined dynamics of swirler and turbulent premixed swirling flames*, Combustion and Flame 157, (2010), 1698-1717.
- [45] P. PALIES, D. DUROX, T. SCHULLER and S. CANDEL, *Nonlinear combustion instability analysis based on the flame describing function applied to turbulent premixed swirling flames*, Combustion and Flame 158 (2011) 1980-1991.
- [46] D. FANACA, P.R. ALEMELA, F. ETTNER, C. HIRSCH, T. SATTELMAYER and B. SCHUERMANS, *Determination and Comparison of the Dynamic Characteristics of a Perfectly Premixed Flame in Both Single and Annular Combustion Chamber*, ASME paper GT2008-50781, 2008.
- [47] P.R. ALEMELA, D. FANACA, F. ETTNER, C. HIRSCH, T. SATTELMAYER and B. SCHUERMANS, *Flame Transfer Matrices of a Premixed Flame and a Global Check with Modeling and Experiments*, GT2008-50111, 2008.
- [48] W. KREBS, P. FLOHR, B. PRADE and S. HOFFMANN, *Thermoacoustic Stability Chart for High Intensity Gas Turbine Combustion Systems*, Combustion Science and Technology, 174 (7), pp.99-128, 2002.
- [49] A. GIAUQUE, L. SELLE, T. POINSOT, H. BUECHNER, P. KAUFMANN and W. KREBS, *System Identification of a Large-Scale Swirled Partially Premixed Combustor Using LES and Measurements*, Journal of Turbulence, 6 (21), pp.1-20, 2005.
- [50] G. CAMPA, S. CAMPOREALE, *Prediction of the Thermoacoustic Combustion Instabilities in Practical Annular Combustors*, Journal of Engineering for Gas Turbines and Power, 2014.
- [51] C. PANKIEWITZ and T. SATTELMAYER, *Time Domain Simulation of Combustion Instability*, ASME paper, GT-2002-30063, 2002.